



저작자표시-비영리-변경금지 2.0 대한민국

이용자는 아래의 조건을 따르는 경우에 한하여 자유롭게

- 이 저작물을 복제, 배포, 전송, 전시, 공연 및 방송할 수 있습니다.

다음과 같은 조건을 따라야 합니다:



저작자표시. 귀하는 원저작자를 표시하여야 합니다.



비영리. 귀하는 이 저작물을 영리 목적으로 이용할 수 없습니다.



변경금지. 귀하는 이 저작물을 개작, 변형 또는 가공할 수 없습니다.

- 귀하는, 이 저작물의 재이용이나 배포의 경우, 이 저작물에 적용된 이용허락조건을 명확하게 나타내어야 합니다.
- 저작권자로부터 별도의 허가를 받으면 이러한 조건들은 적용되지 않습니다.

저작권법에 따른 이용자의 권리는 위의 내용에 의하여 영향을 받지 않습니다.

이것은 [이용허락규약\(Legal Code\)](#)을 이해하기 쉽게 요약한 것입니다.

[Disclaimer](#)

February 2013
Ph.D. Dissertation

Preparation and Characterization of Electrospun Nanofibers for Dye-sensitized Solar Cells

Graduate School of Chosun University

Department of Chemical Engineering

Cheong-Suk Yang

Preparation and Characterization of Electrospun Nanofibers for Dye-sensitized Solar Cells

염료감응태양전지용 전기방사 나노파이버의 제조 및 특성

February 25, 2013

Graduate School of Chosun University

Department of Chemical Engineering

Cheong-Suk Yang

Preparation and Characterization of Electrospun Nanofibers for Dye-sensitized Solar Cells

Supervised by Professor Sun-Il Kim

This dissertation is submitted to the Graduate School of
Chosun University in Partial fulfillment of the requirements
for the Degree of Doctor of Philosophy in Engineering

October 2012

Graduate School of Chosun University

Department of Chemical Engineering

Cheong-Suk Yang

This dissertation of Cheong-Suk Yang has been
approved by the following supervisor committee
members

Chairman	Chosun University	Prof. Byung-Wook Jo
Member	Chonnam Nat'l University	Prof. Hee Moon
Member	Chosun University	Prof. Jung-Gyu Kim
Member	Chosun University	Prof. Jae-Wook Lee
Member	Chosun University	Prof. Sun-Il Kim

December 2012

Graduate School of Chosun University

Acknowledgment

I would like to thank Professor Sun-Il Kim for giving me an interesting research topic and for supervising the thesis as well as for his guidance in selecting the guidelines for the work. I am extremely grateful to Professor Sun-Il Kim for his excellent guidance, advice, consistent motivation and unstinted enthusiasm, patience and the degree of freedom that he gave, made me to explore, adopt innovative learning and develop a scientific temper.

I am grateful to my thesis committee members, Professor Jae-Wook Lee, who monitored my works and put efforts in reading and providing me with valuable comments on this thesis. Especially, I must thank Professor Byung-Wook Jo for his special care, helpful advises and support, which were really helped me to made a better form of final version of thesis. I wish to express gratitude to Professor Hee Moon, Professor Jung-Gyu Kim, who really inspired me by their caring nature and ingenuity.

I wish to thank my laboratory members of Department of Biochemical Engineering for their helping hands whenever it was needed. They supported me in a several critical situations and also gave me a special care on every occasion.

Finally, I am in paucity of words to express my inner feeling for my parents and my wife, whose constant encouragement and moral support always sacrificed their own wishes and happiness toward the upliftment of my career. Without their car, love, sacrifice, support, prayers, wishes and motivation, it wold have not been possible to finish my Ph. D course.

Cheong-Suk Yang

December, 2012

Table of Contents

List of Tables	iv
List of Figures	v
Abstract in Korea	x
Chapter I . Introduction	1
1.1 Research Background	1
1.1.1 Synthesis of TiO ₂ by Sol-gel Method	4
1.1.2 Electrospinning	7
1.1.3 Dye-sensitized Solar Cells	12
1.2 Objective	16
1.3 Overview	19
Chaper II . Theoretical Background of Dye-sensitized Solar Cells	20
2.1 Working Principle of Dye-Sensitized Solar Cells	20
2.2 Photovoltaic Energy Conversion	24
2.2.1 The Solar Spectrum	24
2.2.2 Air Mass	25
2.2.3 Basic Parameters of Solar Cell Performance	27

2.3 Panchromatic Sensitizers	32
2.3.1 Light Absorption via MLCT Excitation	32
2.3.2 Dye Molecule Sensitizers	33
2.4 Interfacial Principle of DSSCs	38
2.4.1 Interfacial Kinetics	38
2.4.2 Charge Transport	39
2.4.3 Charge Recombination	43
Chapter III. Experimental Procedure	45
3.1 Preparation of Materials for DSSC	45
3.1.1 TiO ₂ Particle by Sol-gel Method	45
3.1.2 Electrospun TiO ₂ Nanofibers	48
3.1.3 Electrospun Al ₂ O ₃ Nanofibers	50
3.2 Preparation and Measurement of DSSCs	54
3.2.1 Preparation of DSSCs	54
3.2.2 Measurement of DSSCs	67

Chapter IV. Results and Discussion	69
4.1 Materials	69
4.1.1 TiO ₂ Particles by Sol-gel Method	69
4.1.2 Electrospun TiO ₂ Nanofibers	76
4.1.3 Electrospun Al ₂ O ₃ Nanofibers	80
4.2 Photoelectricity for DSSC Performance	94
4.2.1 TiO ₂ Particle Photoelectrode	94
4.2.2 TiO ₂ Nanofiber Doped TiO ₂ Particle Electrode	105
4.2.3 Al ₂ O ₃ Nanofiber Doped TiO ₂ Particle Electrode	107
 Chapter V. Conclusions	 115
 References	 118
 Abstract in English	 125

List of Tables

Table 1-1 Electrospinning parameters and their effects on fiber morphology	11
Table 1-2 The crystal structure and properties of TiO ₂ (rutile, anatase and brookite)	15
Table 3-1 Experimental condition of DSSC	54
Table 4-1 Condition of electrospinning in this study	90
Table 4-2 Surface properties of TiO ₂ film	95
Table 4-3 Photovoltaic performance of DSSC	101
Table 4-4 Characteristics values of dye-sensitized solar cells according to adsorption time	103
Table 4-5 Photovoltaic performance of DSSC with TiO ₂ nanofiber dopant	106
Table 4-6 Photocurrent-voltage of dye-sensitized solar cells for Al ₂ O ₃ nanofiber doped TiO ₂ electrodes	113

List of Figures

Figure 1-1	The simplified scheme of the first step creation.	6
Figure 1-2	Typical electrospinning setup. Q, flow rate; d, distance between collector and needle; V, applied voltage.	8
Figure 1-3	Different morphology of electrospun nanofibers : (a) beaded (b) ribbon (c) porous fibers and (d) core-shell.	9
Figure 1-4	Potential applications of electrospun polymer nanofibers.	10
Figure 1-5	Schematic structure of dye-sensitized solar cell.	13
Figure 2-1	The working principles and energy level diagram of dye-sensitized solar cell (DSSC).	21
Figure 2-2	Solar radiation spectrum in space and after entering the atmosphere (a) and the spectral distribution of air masses (0, 1, 2 and 5) (b).	24
Figure 2-3	Reference spectral distributions geometry and Global AM1.5 model.	26
Figure 2-4	Dye-sensitized solar cells : I-V plots of solar cell.	27
Figure 2-5	A solar simulation system.	31
Figure 2-6	Schematic illustration of Charge transfer poceses at the metal oxide (TiO ₂)/dye interface and electron injection into metal oxide.	33
Figure 2-7	Photocurrent action spectra of nanocrystalline TiO ₂ films	

sensitized by N3, N719 and the black dye(N749).	36
Figure 2-9 A schematic of energy level diagram for metal oxide/dye/ electrolyte interfaces.	43
Figure 3-1 Experimental procedure for preparation of the TiO ₂ nanoparticles by sol-gel method.	46
Figure 3-2 Experimental procedure for preparation of the TiO ₂ nanofiber by electrospinning method.	49
Figure 3-3 Flow chart of the preparation of alumina nanofibers.	52
Figure 3-4 Schematic diagram of the electrospinning apparatus.	53
Figure 3-5 The typical preparation for TiO ₂ paste and the various coating method for the fabrication of nanocrystalline TiO ₂ thin film.	57
Figure 3-6 TG analysis of sol-gel TiO ₂ film and HPC powder.	59
Figure 3-7 Fabrication method of dye-sensitized solar cell.	66
Figure 4-1 XRD patterns of sol-gel TiO ₂ particles calcinated at 250, 350, 500, 600 and 700 °C. (a) Rutile, JCPDS No. 21-1276, (b) Anatase. JCPDS No. 21-1272.	71
Figure 4-2 SEM photographs of sol-gel TiO ₂ particle calcined at various temperatures: (a) 350 °C , (b) 500 °C , (c) 600 °C and (d) 700 °C.	72
Figure 4-3 X-ray diffraction spectra of sol-gel TiO ₂ and P25-TiO ₂	74

Figure 4-4	X-ray photoelectron spectra of (a) the sol-gel TiO ₂ particle, (b) Ti 2p core level and (c) O 1s core level.	75
Figure 4-5	FE-SEM image of (a) sol-gel TiO ₂ particle, (b) as-spun TiO ₂ nanofiber at room temperature and (c) calcined at 500 °C.	77
Figure 4-6	XRD patterns of electrospun TiO ₂ nanofiber calcined at different temperature.	78
Figure 4-7	N ₂ gas adsorption and desorption isotherms (a) and pore volume distributions (b) of sol-gel TiO ₂ particle and TiO ₂ nanofiber.	79
Figure 4-8	(a) The thermogravimetric curve and (b) the derivative weight loss curve of the as-spun AIP/PVP nanofibers. The heating rate was 10 °C/min.	81
Figure 4-9	SEM images of as-spun AIP/PVP nanofibers.	83
Figure 4-10	SEM images of alumina nanofibers calcinated at 800 (left) and 1200 °C (light).	84
Figure 4-11	SEM images and diameter distributions of (a) the as-spun AIP/PVP nanofibers and the nanofibers calcined at (b) 800 °C and (c) 1200 °C.	85
Figure 4-12	XRD spectra of the alumina nanofibers calcined at 700 °C, at 800 °C and those at 1200 °C; (a) γ-Alumina from JCPDS file 10-0425, (b) α-Alumina form JCPDS file 42-1468.	87
Figure 4-13	FT-IR spectra of (a) AIP solution, (b) AIP/PVP solution, (c) as-spun AIP/PVP composite nanofibers, (d) alumina	

nanofibers calcined at 800 °C, (e) and those calcined at 1200 °C. (B:Al-O bending, S:Al-O stretching).	89
Figure 4-14 SEM image according to relative humidity of as-spun Al ₂ O ₃ /PVP nanofiber; (a) RH < 35 %, (b) RH 40-45 % (c) RH 45-50 % (d) RH 50-55 % and (e) RH 70 < %. Electrospinning condition (1.5 mL/h, 20 kV, 15 cm).	92
Figure 4-15 SEM image of as-spun Al ₂ O ₃ nanofibers at different power supply (a) 15 kV and (b) 20 kV (Relative Humidity <35 %).	93
Figure 4-16 FE-SEM images of (a) P25-TiO ₂ and (b) sol-gel TiO ₂ film. ...	95
Figure 4-17 N ₂ gas adsorption and desorption isotherms (a) and pore size distributions (b) of sol-gel TiO ₂ and P25-TiO ₂ films.	97
Figure 4-18 FT-IR spectra; N719 dye powder (a), N719 dye adsorbed on P25-TiO ₂ film (b) and sol-gel TiO ₂ film (c).	99
Figure 4-19 Photocurrent-voltage (I-V) curves of sol-gel TiO ₂ and P25-TiO ₂ films.	101
Figure 4-20 Efficiency and adsorption amount according to adsorption time of N719 dye.	104
Figure 4-21 Photocurrent-voltage(I-V) of DSSCs depending on the contents of TiO ₂ nanofiber dopant in TiO ₂ electrode.	106
Figure 4-22 SEM image (left side) and EDS analysis (right side) of Al ₂ O ₃ nanofiber doped TiO ₂ films; (a) without Al ₂ O ₃ nanofiber, (b) 0.5 % Al ₂ O ₃ nanofiber (c) 1.0 % Al ₂ O ₃ nanofiber.	108

Figure 4-23 XPS Survey graphs (a) and Al 2p core level (b) of Al ₂ O ₃ nanofiber doped TiO ₂ films.	110
Figure 4-24 Electrochemical impedance spectra of TiO ₂ /Al ₂ O ₃ nanofiber doped electrode.	112
Figure 4-25 Photocurrent-voltage(I-V) polt of DSSCs depending on the contents of Al ₂ O ₃ nanofiber dopant in TiO ₂ electrode.	114

국문초록

염료감응태양전지용 전기방사 나노파이버의 제조 및 특성

양 청 석

지도교수 : 김선일, Ph.D.

화학공학과

조선대학교 대학원

태양전지는 광전기적 효과에 의해 태양빛 에너지를 전기로 직접 변화시키는 전기 발생 장치이다. 염료감응형 태양전지는 반도체가 접합되어 있는 기존의 태양전지와는 달리 높은 에너지 변환 효율과 저렴한 제조단가로 인하여 산업계의 비상한 관심을 모으고 있다. 지금까지 염료감응형 태양전지의 효율향상을 위해 주로 TiO_2 나노결정 소재 및 전극구조, 염료 개발, 전해질 및 홀전도체, 광전자 전달, 봉합기술 그리고 전도성 기판 등에 관한 연구들이 수행되고 있다.

본 논문에서는 염료감응형 태양전지 효율향상을 위해 다양한 방법으로 TiO_2 전극을 개발하고 에너지 전환 효율을 평가하였다. 이를 위해 TiO_2 나노입자를 가수분해에 의한 졸-겔 방법으로 합성하였다. 이렇게 얻은 나노입자는 염료감응형 태양전지에서 요구되는 아나타제의 결정상과 약 15 nm의 입자크기로 이루어져 있음을 확인할 수 있었다. 제조된 TiO_2 및 상업용 P-25를 이용하여 광전극 샘플을 BET, FE-SEM, FT-IR, XPS 및 XRD 등을 이용하여 분석하였다. 본 연구에서 제조한 TiO_2 의 광전극의 에너지 전환효율이 상업적으로 널리 이용되는 P25- TiO_2 로 제작된 광전극에 비해 효율이 높다는 것을 알 수 있었다. 그리고 흡착특성이 에너지 전환효율에 미치는 영향을 조사하였다. 이를 위해 제조된 TiO_2 나노입자 상에서 N719 염료의 흡착평형 및 속도론에 관해 연구하였다.

염료감응형 태양전지의 효율향상을 위해 $\text{TiO}_2/\text{dye}/\text{electrolyte}$ 인터페이스에서 나타나는 전자의 재결합 손실을 줄일 수 있는 방법으로 금속 산화물들이 이용되고 있다. 본 논문에서 넓은 범위의 태양광 흡수가 가능한 TiO_2 나노입자에 전기방사법으로 제조된 TiO_2 나노파이버와 Al_2O_3 나노파이버 등을 첨가하여

TiO₂ 광전극의 에너지 전환효율에 관한 연구를 수행하였다. 전기방사법으로 제조된 TiO₂ 나노파이버와 Al₂O₃ 나노파이버의 특성분석은 SEM, XRD, FT-IR 및 TGA 를 통해 확인하였다. 단락 전류(short-circuit)의 광전류를 개선하기 위해서 졸-겔법에 의해 합성된 TiO₂ 광전극에 TiO₂ 나노파이버와 Al₂O₃ 나노파이버를 각기 다른 함량으로 첨가하여 페이스트를 제조한 후, 염료감응태양전지의 효율 변화를 조사하였다. TiO₂ 나노입자에 TiO₂ 나노파이버가 첨가된 광전극이 TiO₂ 나노입자만으로 제조한 광전극에 비해 에너지전환효율이 15 % 이상 증가하였다. TiO₂ 나노파이버를 1.5 % 함유한 광전극의 에너지 변환 효율 (η_{eff})은 5.87 % 임을 확인할 수 있었다. 이러한 결과는 졸-겔법으로 제조한 TiO₂ 광전극에 비해 Al₂O₃ 나노파이버를 첨가한 광전극의 염료 흡착량이 더 많고 액체 전해질 내의 I₃⁻ 이온의 높은 확산 속도에 기인한다는 사실을 전기화학적 특성 분석을 통해 확인 할 수 있었다.

Chapter I . Introduction

1.1 Review of the Current Literature

The use of fossil fuels is a major cause of environmental pollution and the reserves of fossil fuels are not infinite. With the increased use of fossil fuels, it is important to consider the impact their use has on our global environment. Therefore, the development of new energy sources that are clean and advanced and making the change to them away from global fossil fuel use will be essential in the future. Also in order to convert to clean energy, such as wind, solar, and tidal power, from fossil fuel sources new technology and devices must be developed for clean energy-conversion, storage, and conservation [1].

Energy issues related to the economy and the global environment, are at the center of discussions on the long-term sustainability in energy. The use of fossil fuels is causing problems such as air pollution and global warming. Thereby, serious problems such as the average temperature rising and sea level rises can be the result in the future. To regulate carbon dioxide emissions as the main cause of global warming, the Kyoto Protocol, adopted in December 1997 and formally entered into force on February 16, 2005, and the carbon dioxide reduction program is working. Korea from 2013 is included in the list of carbon dioxide regulated countries.

According to an OPEC report[2], primary energy demand was expected to increase by 51% by the year 2035, and fossil fuels would account for 82% of total energy by 2035. Carbon dioxide emissions since 1990 have increased steadily and this is projected to continue steadily through 2035 and fossil

fuels are predicted to be the cause of up to 61% of total Carbon dioxide emissions. In addition, carbon dioxide emissions due to fossil fuel use has contributed to between 6 and 9% of the greenhouse effect[1,3].

Although the use of fossil fuels, particularly oil and coal, is projected to grow at high rates contributing more than half of the global energy supply, the use of new energy resources such as nuclear, hydro, and biomass in addition to other renewables are expected to play a leading role through 2030. Photosynthetic activity of plants is one way carbon dioxide can be controlled naturally, however current control of carbon dioxide emissions will be difficult. In order to reduce carbon dioxide emissions, efforts to reduce the use of fossil fuels and substitute it with renewable energy sources, should be made.

There are promising renewable energy devices such as fuel cells, lithium-ion batteries, and solar cells. Developing these energy technologies to meet our energy demands represents an important step forward, therefore new innovation is required to improve their performance in terms of harvesting efficiency, durability, power density, conversion efficiency, and cost. To overcome these problems, researchers have been trying to create new nano sized functional materials.

In recent years, nano-technology has attracted a lot of attention and is being used in the fields of electronics, information technology, and communications. It has found wide application in other areas as well, including the mechanical and chemical sciences, biotechnology, and the energy sector[4,5].

Nano-materials have a very high surface area to volume ratio and have

unique physical and chemical properties unlike bulk materials. Electrospun nanofibers with one-dimensional structure have been applied to new energy technologies such as energy storage and energy conversion devices. An excellent example of this is the absorption of solar radiation in photovoltaic cells. The absorption is much higher in structures composed of nano materials than it is in continuous sheets of thin film material. In this case, the smaller particles lead to greater solar energy absorption. There are many kinds of nanoscale materials including nanoparticles, nanopowders, nanorods, nanotubes, and nanowires. Nanoparticles have been studied for a long time and nanofibers have received the attention of researchers recently.

Nanofibers are composed of 1D materials that can be used in various applications where high surface area and porosity are desirable. Nanofibers can be prepared by many methods such as template-directed methods, vapor-phase methods [6], interface synthesis techniques [7], solvothermal synthesis [8], solution-phase growth controlled by capping reagents [9], nanolithography [10,11], self-assembly [12] and the electrospinning method.

Recently, electrospinning, a simple, inexpensive technique, has attracted significant attention in the preparation of nanomaterials. Through the electrospinning technique, nanofibers or nanorods, nanotubes, and different shapes of materials can be easily manufactured enabling users to successfully manufacture complex things such as polymers or metal oxide nanofibers, chemical and biological sensors, tissue engineering, and scaffolds have been studied in such applications[13]. These electrospun nano-materials have unique properties that can be applied to various fields, including the fabrication of nano-materials for use in energy conversion devices.

1.1.1 Synthesis of TiO₂ by the Sol-gel Method

The sol-gel method was developed in the 1960s due to the need for new synthesis methods in the nuclear industry. A method was needed where dust was reduced (compared to the ceramic firing method) and which needed a lower sintering temperature. In addition, it should be possible to do the synthesis by remote control. Synthesis by this method is possible by remote control and at a lower temperature^[14]. Sol-gel synthesis can be used to prepare materials with a dense porous structure. In addition, this technology is very efficient in producing different kinds of functional materials in which particle size, porosity, separation of particles with different compositions and structures may be controlled and successful applications using this method have been achieved.

In other words, the sol-gel process may be described as a way to form three dimensional continuous networks through a poly condensation reaction of molecular precursors in a liquid. The procedure for sol-gel synthesis is as follows:^[15]:

Hydrolysis

A mixture of alkoxide and water in a solvent(alcohol) starts to react slowly under atmospheric pressure.



Polymerization

The water and solvent are removed by the condensation reaction with the reactants and the polymers formed by the condensation reaction become a colloid because bridges between metal oxides are made. In these conditions, particles start to form. These particles combine with the metal

and oxygen to form a three-dimensional lattice structure.

Gelation

In this process, the viscosity of the mixed solvent suddenly rises and the solvent becomes a gel if the reaction goes over the gel point.

Drying

The water and solvent are removed at ordinary temperatures and the hydrated metal oxides and organic residues remain. For the purpose of making aerogels and products which will have the large surface area and low-density, the water and solvent must be removed completely.

Dehydration

After the mixed solvent is dried, the gel has silanol group on its surface and contains water in its holes. The water and hydroxy-groups must be removed to make the gel stable. The chemical method or sintering is used for this. Chlorosilane, silicon tetrachloride, chlorine, and carbon tetrachloride are used to remove the silanol group.

Densification

Hydrolysis and condensation occur not only in solution but also in the xerogel or aerogel. Products made by this process are not stable although they are solid. Therefore, the product must go through thermal processing to be made stable. Because xerogel is porous itself, it shrinks a lot during thermal processing. In this shrinking process, the density increases a lot.

Synthesis of TiO_2 by the sol-gel method is similar to the following procedure. First, titanium alkoxide is dissolved thoroughly in alcohol. Next, the solvent is hydrolyzed and then polymerized to form sol which has

colloidal particles below $1\mu\text{m}$ is size spread through it. Then this sol changes into gel which has a three-dimensional network structure. This gel is dried and calcined to form TiO_2 . This is the most common way to make TiO_2 .

Throughout the procedure of making TiO_2 via the TiO_2 sol-gel method, the alkoxide group (OR) and the hydroxyl group (OH) are switched in the hydrolysis and a Ti-O-Ti combination occurs with water or alcohol formed by the condensation reaction; (a) the removal of unreacted alkoxide ($\text{Ti}^{4+}\text{-OR}$) and the terminal i-OPr group (-OR) at a temperature higher than 473 K, (b) the forming of surface defects (Ti^{3+}) after removal of the terminal i-OPr group (-OR) after calcination at 723 K (Figure 1-1) [16].

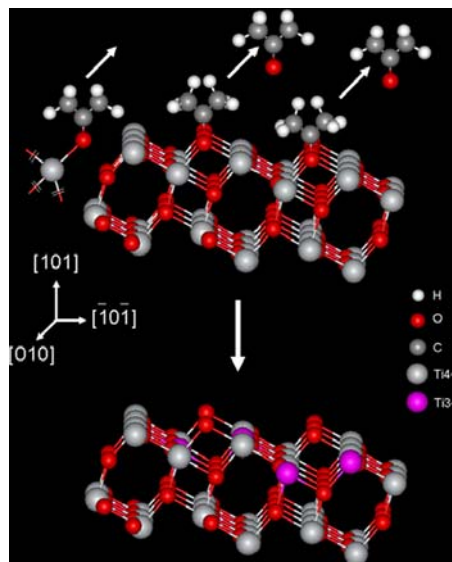


Figure 1-1 The simplified scheme for the first step in creation.

1.1.2 Electrospinning

1.1.2.1 The Principle of Electrospinning

The field of electrospinning had its starting point in the electrical dispersion of fluids in 1902. The fabrication of textile yarns from electrically dispersed fluids was patented by Formhals in 1934. This technique did not receive much attention until the 1990s.

However, It was found that organic polymer nanofibers can be produced using electrospinning, since then, the term “electrospinning” has been popularized and attention and research in electrospinning has increased significantly each year. Today, electrospinning is an established technique for generating nanofibers [17,18].

A typical electrospinning apparatus consists of a syringe, a collector and a high voltage power supply. A schematic of an electrospinning set up is shown in Figure 1-2 [19]. In a typical fiberspinning process, a syringe is filled with a melt or blend polymer solution and a high voltage is applied between the syringe nozzle and a collector. Electrospinning is fundamentally different from air or other mechanically driven spinning techniques in that the extrusion force is generated by the interaction between the charged polymer fluid and an externally applied electric field. During electrospinning, a conical fluid structure called a Taylor cone [20] is formed at the tip of the syringe. At a critical voltage, the repulsive force of the charged polymer overcomes the surface tension of the solution and a charged jet erupts from the tip of the Taylor cone. If the applied voltage is not high enough, the jet will break up into droplets, a phenomenon called Rayleigh instability. If the voltage is sufficiently high, a stable jet will form near the tip of the Taylor

cone. Beyond the stable region, the jet is subject to bending instability [21,22] that results in the polymer being deposited on the grounded collector via a whipping motion. As the charged jet accelerates towards the region of lower potential, the solvent evaporates, and the resulting increase in electrostatic repulsion of the charged polymer causes the fibers to elongate. The strength of the polymer chains prevent the jet from breaking up resulting in the formation of fibers.

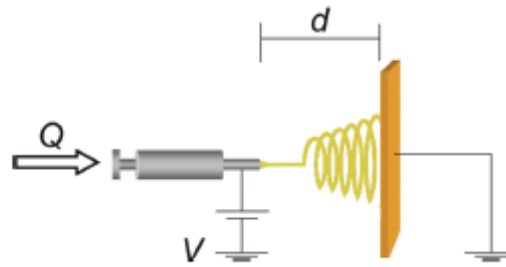


Figure 1-2 A Typical electrospinning setup. Q , flow rate; d , distance between collector and needle; V , applied voltage.

Almost any soluble polymer can be electrospun if its molecular weight is high enough. However, the creation of fine nanofibers requires careful consideration of many operating parameters (such as polymer molecular weight, applied voltage, solution feed rate, and spinning distance), environmental parameters (such as temperature, humidity, and air velocity in the chamber) and solution properties (such as conductivity, viscosity, and surface tension). By selecting different polymer blends and tuning these electrospinning process parameters, a wide range of nanofibers made of natural polymers, polymer blends, ceramic precursors, and metal or metal oxides have been spun in the form of each different fiber morphology, such

as beaded [23], ribbon [24], porous [25,26], core-shell, and aligned [27] fibers (Figure 1-3).

Nanofibers according to electric application areas are as follows (see Figure 1-4). Because electrospun fibers have a nanofibrous structure similar to human tissues and organs [20], they are well suited for use in many biomedical applications such as tissue engineering [28], medical prostheses [29], drug delivery [30], and wound healing [31]. In addition to biomedical applications, they have also been used in other areas such as sensors [32,33], filters and separation membranes, templates for nanotube materials, protective layers, composite materials and energy applications [34,20].

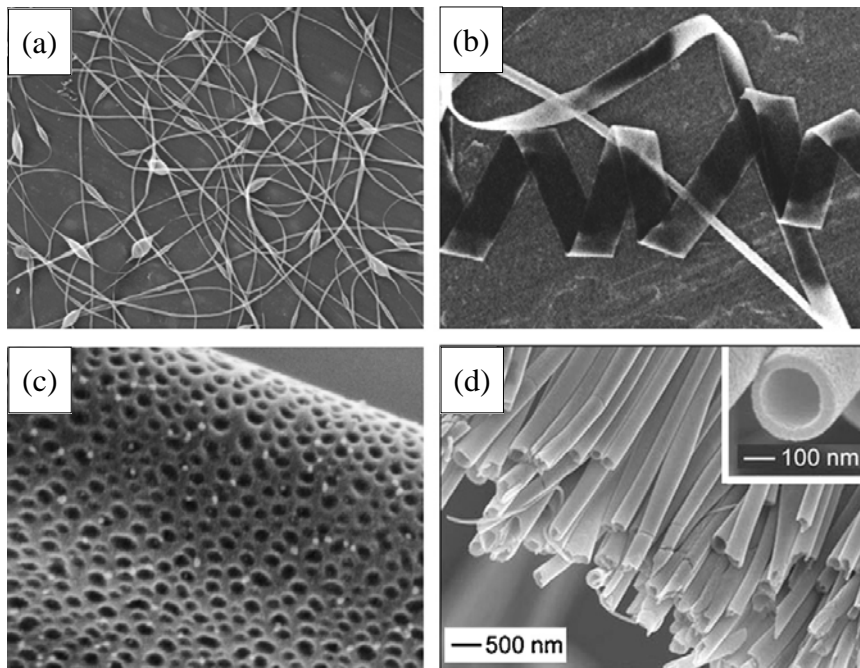


Figure 1-3 Different morphology of electrospun nanofibers: (a) beaded (b) ribbon (c) porous fibers and (d) core-shell.

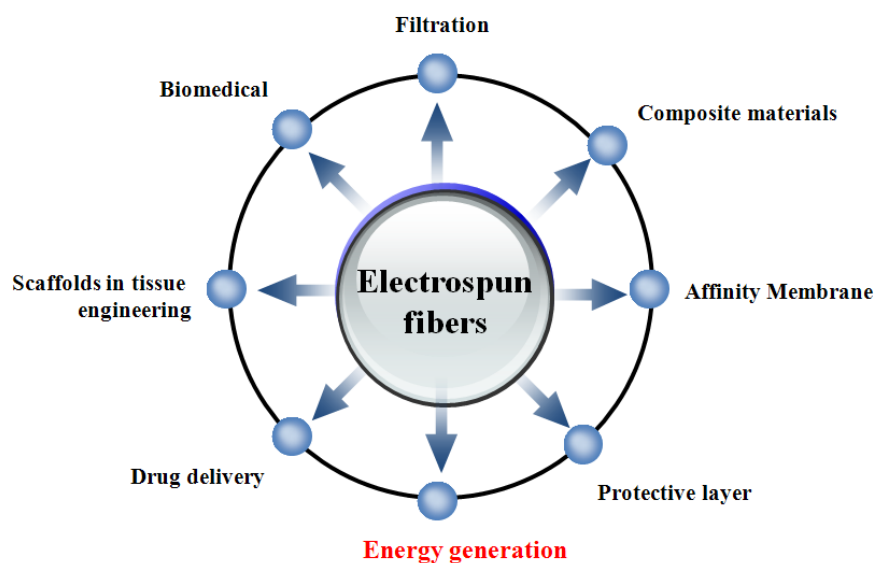


Figure 1-4 Potential applications of electrospun polymer nanofibers.

1.1.2.2 Parameters on Electrospinning

The electrospinning process is solely governed by many parameters, classified broadly into solution parameters, process parameters, and ambient parameters [35]. Solution parameters include viscosity, conductivity, molecular weight, and surface tension. Process parameters include the degree of applied electric field, the tip to collector distance, and the feeding or flow rate. Each of these parameters significantly affects the fibers morphology obtained as a result of electrospinning, and by proper manipulation of these parameters we can get nanofibers of the desired morphology and diameter [36]. In addition to these variables, ambient parameters encompass the humidity and temperature of the surroundings which play a significant role

in determining the morphology and diameter of electrospun nanofibers [17]. In Table 1-1, various parameters and their effects on fiber morphology have been shown.

Table 1-1 Electrospinning parameters and their effects on fiber morphology

Parameters	Effect on fiber morphology	Ref.
Solution parameters		
Viscosity	Low-bead generation, high-increase in fiber diameter , disappearance of beads.	[37]
Polymer concentration	Increase in fiber diameter with increase of concentration.	[38]
Molecular weight of polymer	Reduction in the number of beads and droplets with increase of molecular weight.	[39]
Conductivity	Decrease in fiber diameter with increase in conductivity.	[40]
Surface tension	No conclusive link with fiber morphology, high surface tension results in the instability of jets.	[41]
Processing parameters		
Applied voltage	Decrease in fiber diameter with increased voltage.	[42]
Distance between tip and collector	Generation of beads with too small and too large a distance, a minimum distance required for uniform fibers.	[43]
Feed rate/Flow rate	Decrease in fiber diameter with a decrease in flow rate, generation of beads with too high a flow rate.	[44]
Ambient parameters		
Humidity	High humidity results in circular pores on the fibers.	[45]
Temperature	An increase in temperature results in a decrease in fiber diameter.	[46]

1.1.3 Dye-sensitized Solar Cells

Recently, Electrospun materials have been used as a material for energy conversion devices and can also be used in the manufacture of solar cells. Solar cells convert the energy of sunlight directly into electrical energy via the photovoltaic effect. Solar cell development has progressed through several stages including crystalline silicon, thin-film and now a third generation of solar cells, dye-sensitized solar cells (DSSCs), which cover a variety of advanced thin-film technologies. Dye-sensitized solar cells are a relatively new area of thin-film solar cells. DSSC technology can be described as an artificial photosynthesis process^[1].

In the original Grätzel design, a cell was composed of three main parts; (1) a transparent fluorine-doped tin oxide ($\text{SnO}_2\text{:F}$) deposited on a glass plate that served as the anode, (2) a platinum sheet was the cathode, and (3) a photosensitive ruthenium-polypyridine dye deposited on TiO_2 (or ZnO , etc.) film with a thin layer of iodide sandwiched between the two electrodes.

Figure 1-5 is a schematic illustration of a DSSC. The use of electrospun materials in DSSC photoelectrodes and electrolytes can be described as follows^[47]. (1) Upon light absorption, the dye (S) is promoted into an electrically excited state (S^*) from there it injects, an electron into the conduction band of a large band gap semiconductor film (TiO_2), onto which it is adsorbed. (2) The electrons are transported through the TiO_2 film by diffusion before reaching the anode of the cell. (3) The positive charges resulting from the injection process are transferred into the liquid electrolyte by reaction of the dye cation (S^+) with the reduced species of a redox

couple in the electrolyte solution. This leads to the generation of the charge neutral state of the sensitizer. (4) The most typical redox couple is I^-/I_3^- . After ionic diffusion, the carrier of the positive charge (I_3^-) reaches the cathode, where it releases its charge thus being reduced back to I^- .

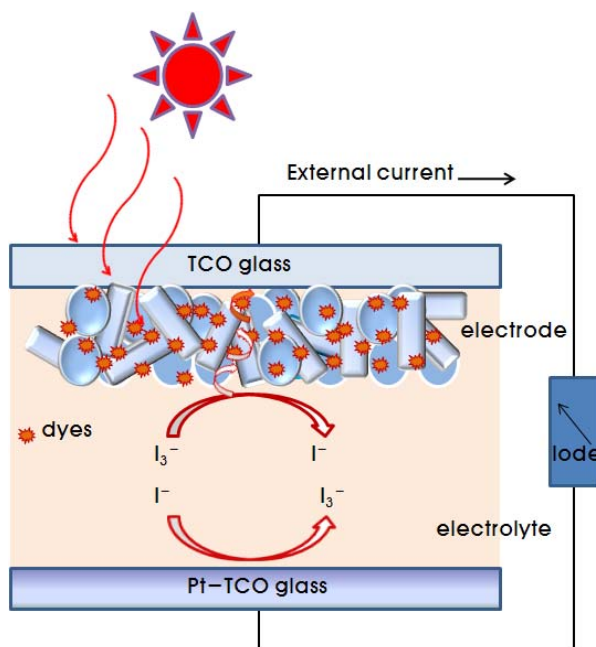


Figure 1-5 Schematic structure of a dye-sensitized solar cell.

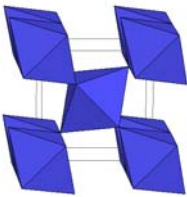


Oxide semiconductors are used specifically in photoelectrochemistry, because of their exceptional stability against photo-corrosion on optical excitation in the band gap^[48]. Furthermore, transparency of the semiconductor electrode for a large part of the solar spectrum is needed in the large band gap (>3 eV) of the oxide semiconductors for DSSCs. In addition to TiO_2 , electrodes of semiconductors with porous nanocrystalline structures used in DSSCs include ZnO , $CdSe$, WO_3 , Fe_2O_3 , SnO_2 , Nb_2O_5 ,

and Ta_2O_5 [49]. However, the cornerstone semiconductor of the dye-sensitized nanostructured electrodes for DSSCs is still TiO_2 .

TiO_2 is a semiconductor which has a wide band gap [In the case of anatase it is 3.2 eV (E_g) and for rutile it is 3.0 eV]. It is widely used, as a pigment in the paper and paint industry, an excipient in pharmaceuticals and as a raw material for cosmetics. It is very cheap and the preparation of particles with a very small size is fairly easy. The crystallite structures of TiO_2 are anatase, rutile, and brookite, of which brookite is very difficult to obtain. Rutile absorbs light in the near UV-region, band-gap excitations lead to generation of holes, and this causes thermal instability in the solar cell. Anatase is dominant at low temperatures ($\sim 1,183.15$ K). Table 1-2 shows the crystal structure and properties of TiO_2 [50].

Only a few mono-layers of the adsorbed dye can efficiently participate in the charge injection process. If a planar surface of TiO_2 is used, the small absorption cross section of the dye will cause poor performance. Therefore, TiO_2 with a sponge-like structure and a high surface area is necessary. The surface area of the film increases with decreasing particle size. The particle size can not be reduced indefinitely because porosity also plays an important role in the performance of the TiO_2 layer. As the particle size decreases, the pores also get smaller. The electrolyte has to be able to penetrate the pores and be present where there is adsorbed dye. In addition, larger particles scatter light more effectively, and this has been found to have a positive effect on the performance of the cell [48]. The particle size needs to be optimized to maximize the effect of the large surface area and the porosity of the film.

Table 1-2 The crystal structure and properties of TiO₂(rutile, anatase, and brookite)

Property	Rutile	Anatase	Brookite
Crystal structure			
Form.Wt.	79.890	79.890	79.890
Crystal structure	Tet* (stable in high temp.)	Tet* (stable in low temp.)	Orth*
Density, g/cm ³	4.2743	3.895	4.123
Refractive index	2.71	5.52	
Dielectric constant	114	31	
Unit Cell			
a, Å	4.5845	3.7842	9.184
b(Å)			5.447
c, Å	2.9533	9.5146	5.145
Vol., Å ³	62.07	136.25	257.38
Melting point	2,131 K	Transformation to rutile at 1,183 K	
Band gap, eV	3.0	3.2	

* Tet ; Tetragonal, Orth; Orthogonal

1.2 Objective

Dye-sensitized solar cells (DSSCs) based on the photosensitization of nanocrystalline TiO_2 electrodes have been regarded as a promising cost-effective alternative to silicon-based solar cells since the pioneering work of O'Regan and Grätzel [51-53]. The key points in developing technology for dye-sensitized solar cells are as follows [52,54]. First, it requires technology where particle size can be regulated and the crystallization factors and the surface conditions of TiO_2 controlled. Second, the material needs to have excellent electronic switching capacity and long-term stability. Third, there must be a suitable dye which will help absorb a wide range of light wavelengths. The material also must have strong chemical bonds with the surface of the nano oxide semiconductor. Finally, new polyelectrolytes are required for solid-state dye-sensitized solar cells [55].

Currently, studies on TiO_2 , which is mostly commonly used for photoelectrodes in dye-sensitized solar cells, are eagerly being conducted. TiO_2 is the most widely used substance as a photocatalyst and it has been proven to be a better catalyst used in photooxidation of various organic materials through a lot of research. The bandgap energy of TiO_2 is about 3.2 eV and the photoreaction of TiO_2 is achieved at wavelengths of 400nm or less.

In fact, of the range of the wavelengths of light that reach the earth, the wavelengths 400nm or less are less than 5% of all sunlight [55] and TiO_2 acts as a catalyst in visible light so it is not that great. New catalysts are required for a wider range of wavelengths. Since the 1990s, a lot of

experiments have been carried out to induce electronic recombination by putting transition metals or nonmetals on TiO_2 and to make the catalysts work at visible light wavelengths by widening the available wavelengths [52, 56].

Mesoporous TiO_2 , is good as it has a very large surface area for electronic transport layers, and it has been used as the basic structure of most DSSCs. Several reports have mentioned that some form mesoporous TiO_2 films have an affect on the performance of DSSCs. [57-59]. Furthermore, their important role, such as trap states of the surface and the recombination of photo generated electrons with dye molecules has been shown in experimental studies [55,57,60,61,]. Reverse photoelectron transfer at the TiO_2 /dye/electrolyte interface has been identified as the major mechanism of loss in DSSCs [55,56]. These studies show the importance of controlling the density of fault status at the TiO_2 /dye/electrolyte interface for improvement of DSSC performance. It was reported that Processing the TiO_2 /dye/electrolyte interface with metal oxide was effective in reducing the recombination losses in DSSCs. In most studies, metal oxides have been used for the previous purposes mentioned. E. Palomares et. al. reported that when Al_2O_3 was included into DSSCs as a recombination blocking layer an increase of 30% was observed in efficiency [57]. To suppress the transport mechanism, a low density surface state or a less active surface state with a small capture cross section, is required.

Therefore, in this research, an experiment for TiO_2 modification which makes a wide range of sunlight available and a recombination blocking layer for the dye-sensitized solar cell was conducted. The main points of this research are:

First, TiO_2 particles by the sol-gel method were synthesized at different temperatures and their structural characteristics were examined.

Second, TiO_2 nanofibers and Al_2O_3 nanofibers were prepared through electrospinning. The morphology of the electrospun TiO_2 nanofibers was observed by field emission scanning electron microscopy (FE-SEM) (Hitach, S-4800). The X-ray diffraction (XRD) pattern was recorded using a Philips (X'Pert PRO MPO) diffractometer (Cu K α radiation). And we investigated the synthesis of alumina nanofibers using a technique that combined the sol-gel and electrospinning methods using aluminum isopropoxide (AIP), an organometallic compound, as the precursor and a PVP polymer solution. The formation, morphology, and crystallinity of the electrospun alumina nanofibers were determined through thermogravimetric analysis (TGA), scanning electron microscopy (SEM), X-ray diffraction (XRD) and Fourier transform-infrared (FT-IR) spectroscopy.

Finally, in order to know the possibility of applying this to the energy field and environment, experiments for the photo conversion efficiency were measured using the DSSCs made in this research. Synthesized sol-gel TiO_2 particles, electrospun TiO_2 nanofibers and electrospun Al_2O_3 nanofibers are used for the photoelectrodes and the main experiment to find how this affects the efficiency of DSSCs is conducted.

1.3 Overview

This paper is organized as follows.

Chapter 1. General introduction, literature review and research purposes are described.

Chapter 2. The general theory of dye-sensitized solar cells are given.

Chapter 3. Experimental methods mainly consists of 1) preparation of TiO_2 particles by the sol-gel method, 2) preparation of TiO_2 and Al_2O_3 nanofibers by electrospinning, 3) preparation and measurement of dye-sensitized solar cells.

Chapter 4. The results and discussion of the experiments are described. In chapter 4.1, as the preparation of materials for the DSSC, Synthesised TiO_2 particles by the sol-gel method were calcined at various temperatures and the characteristics of the synthesized sol-gel TiO_2 particles explained. Synthesis and characterization of TiO_2 and Al_2O_3 nanofibers made by electrospinning was investigated. In chapter 4.2, synthesized sol-gel TiO_2 particles, electrospun TiO_2 nanofibers and electrospun Al_2O_3 nanofibers are used for the photoelectrodes and the efficiency of photo conversion for the each experiment is discussed.

Chapter 5. The main conclusions of this paper are summarized.

This paper consists of five chapters.

Chaper II. Theoretical background of dye-sensitized solar cells

2.1 Working Principle of Dye-Sensitized Solar Cells

At its simplest configuration (Figure 1-5), the DSSC is comprised of a transparent conducting glass electrode coated with porous nanocrystalline TiO_2 , dye molecules attached to the surface of the TiO_2 , and an electrolyte containing a reduction-oxidation couple such as I^-/I_3^- and a catalyst coated counter-electrode. The absorption of light in the DSSC occurs by dye molecules and the charge separation by electron injection from the dye to the TiO_2 at the semiconductor electrolyte interface. A single layer of dye molecules however, can absorb only less than one percent of the incoming light [52]. While stacking dye molecules simply on top of each other to obtain a thick dye layer increases the optical thickness of the layer, only the dye molecules in direct contact to the semiconductor electrode surface can separate charges and contribute to the current generation. A solution to this problem, developed by the Grätzel group, was to use a porous nanocrystalline TiO_2 electrode structure in order to increase the internal surface area of the electrode to allow large enough amount of dye to be contacted at the same time by the TiO_2 electrode and the electrolyte (Figure 1-5).

Figure 2-1 shows principle of operation and energy level scheme of the dye-sensitized nanocrystalline solar cell.

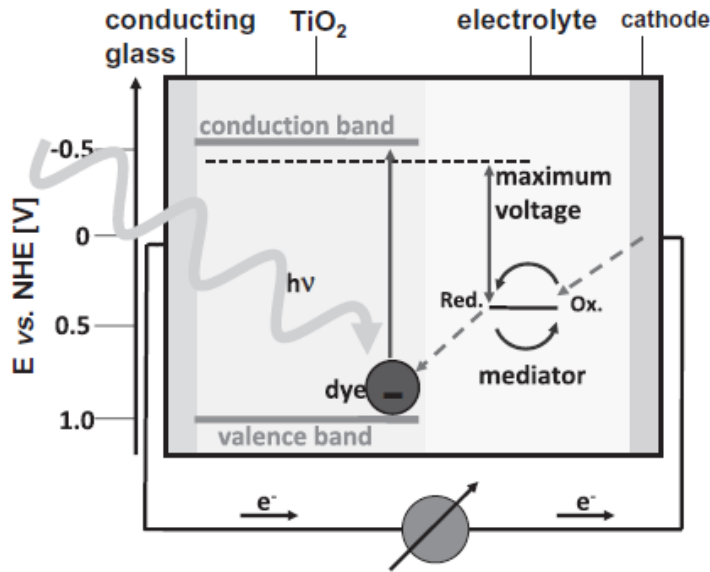
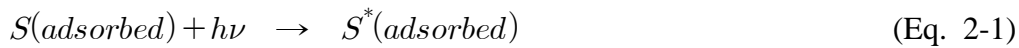


Figure 2-1 The working principles and energy level diagram of dye-sensitized solar cell (DSSC).

DSSCs are based on a process called photoinduced electron transfer, which can be described as follows [65].

The first step is the absorption of a photon by the dye(S) (**photoexcitation**):

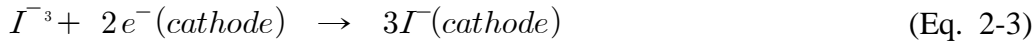


Once in its excited state, the dye can either relax by reemitting a photon, or inject an electron into the conduction band of TiO₂ (**electron injection**):

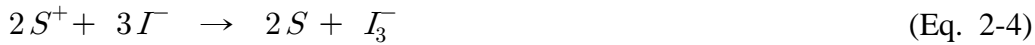


The injected electron travel through the mesoporous network of

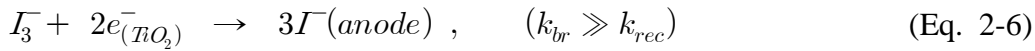
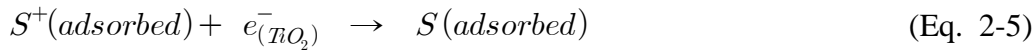
semiconductor by diffusion, before reaching the anode, when they are collected to power a load through an external circuit. Reaching the cathode, the electrons engage in the reduction of the triiodide contained in the electrolyte (**back reaction or br**):



The iodide reacts with the oxidized dye so that it returns to its ground state, and the cycle is completed,



However some undesirable reactions resulting in losses in the cell efficiency occur. DSSCs work because the recombination of the injected electrons with oxidized (Eq. 2-5) or the reduction of triiodide at the TiO_2 surface (Eq. 2-6) is much slower than the back reaction (recombination or rec).



The total efficiency of the dye-sensitized solar cell depends on optimization and compatibility of each of these constituents, in particular on the semiconductor film along with the dye spectral responses [66]. A very important factor is the high surface area and the thickness of the

semiconductor film which leads to increased dye loading, thus optical density resulting in efficient light harvesting [67].

2.2 Photovoltaic Energy Conversion

2.2.1 The Solar Spectrum

Solar power is associated with the survival of all organics on Earth as well as human a very important source of energy. The solar spectrum is one of the electromagnetic spectrum which represented all waves at electromagnetic fields. The solar radiation spectrum corresponds to the sun surface temperature which is about 6000 °C (i.e., the emitted solar spectrum as seen in space). As observed on Earth, it is shifted slightly from the black body radiation spectrum, due to the scattering of blue light and the absorption of red light into the atmosphere. Figure 2-2 shows the spectrum of solar radiation in space and the solar radiation after the scattering and absorption processes by atmospheric aerosols within entering the atmosphere [68,69].

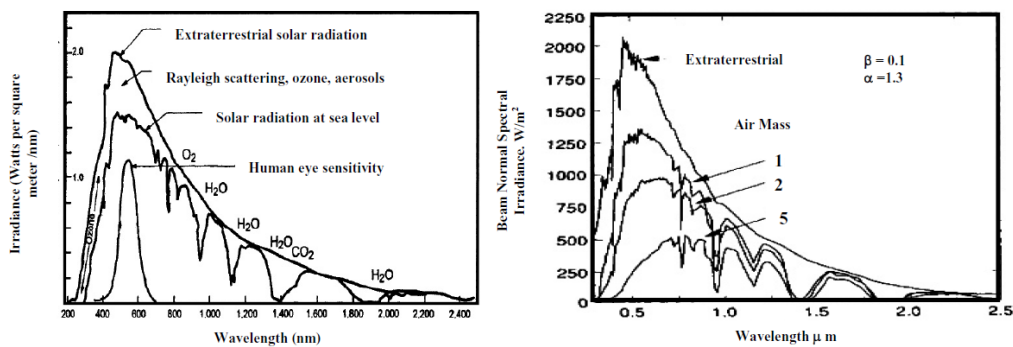


Figure 2-2 Solar radiation spectrum in space and after entering the atmosphere (a) and the spectral distribution of air masses(0, 1, 2 and 5) (b).

2.2.2 Air Mass

Approximately 30 % of sunlight is reflected into the space from the atmospheric boundary layer and the remaining 70% reaches the earth's atmosphere. 3 % of them will disappear due to reflection, reflection and absorption in the atmosphere and sunlight to arrive at the earth's surface is about 67 %. Sunlight, which is passed through the atmosphere to the surface, changes constantly depending on the weather conditions, such as temperature, humidity, clouds. According to these changes, the extent to which the reduction of optical (light) is appears differently and reduced degree of sunlight are represented by the Air Mass (AM).

Namely, air mass is defined as the relative length of the direct-beam path through the atmosphere compared with a vertical path directly to Sea level. Under the assumption of an ideal homogenous atmosphere, simple geometrical considerations lead to:

$$AM=1/\cos z_s \quad (Eq\ 2-7)$$

where, AM is the air mass and z_s is the zenith angle of sun.

AM may be described as follows(Figure 2-3). AM0 is Energy arriving at the edge of earth's atmosphere from the sun, and AM1 ($\Theta = 0^\circ$) is mean Energy that reaches the vertical to earth surface through the atmosphere. Typically AM was calculated using equation 2-1, depending on the angle of the sun from the zenith to the horizon inclined. AM1.5 has an angle of 48.2° and emits approximately 844 W/m^2 of energy. AM1.5 is similar to the value that is used to measure the efficiency of the solar cell

(100 mW/cm²). Global AM1.5 is no cloud and means the distribution of solar energy that irradiate above sea level, slanting 37° from the sun, in air state with the field of vision of 26 km [69].

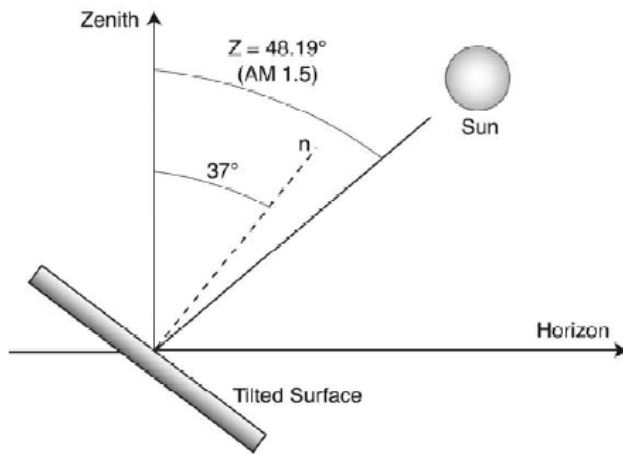


Figure 2-3 Reference spectral distributions geometry and Global AM_{1.5} model.

2.2.3 Basic Parameters of Solar Cell Performance

As a solar cell is illuminated, a current and voltage are generated. The current depends on voltage, and a plot of current versus voltage is called the I-V curve of the cell. The characteristics of an I-V curve is depend on illumination as well as the temperature.

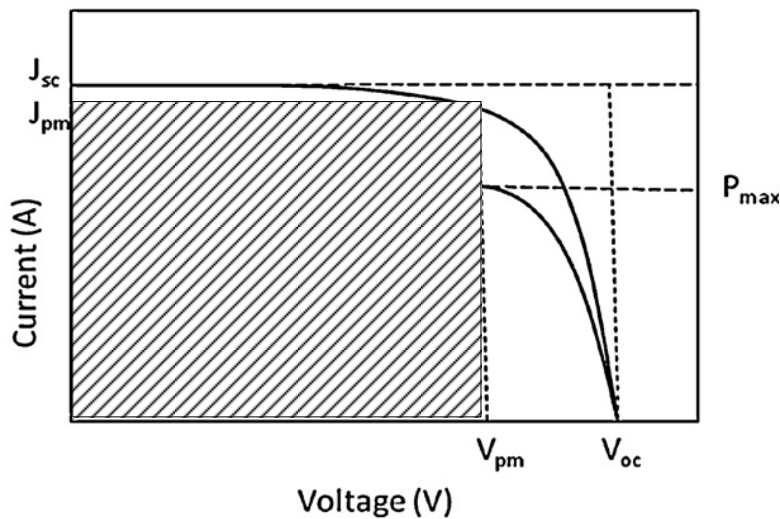


Figure 2-4 Dye-sensitized solar cells : I-V plots of solar cell.

The following terms are used to parameters of solar cell performance, a typical I-V curve shows in Figure 2-4 [48,70,71].

- (1) **Air mass:** As already mentioned, it is the ratio of the path length of the sun rays through the atmosphere when the sun is at a given angle u to the zenith. An air mass distribution of 1.5, as specified in the standard condition, corresponds to the spectral power distribution observed when

the sun's radiation is coming from an angle to over head of about 48 °.

- (2) **Open-circuit voltage (Voc):** When the cell is operated at open circuit, $I = 0$ and the voltage across the output terminals is defined as the open-circuit voltage.
- (3) **Short-circuit current (Isc):** When the cell is operated at short circuit, $V = 0$ and the current I through the terminals is defined as the short-circuit current.
- (4) **Maximum power point (PM):** (I_{pm} , V_{pm}) on the I-V curve is the point where maximum power is produced. Power (P) is the product of current and voltage ($P = IV$) and is illustrated in the Figure 2-4 as the area of the rectangle formed between a point on the I-V curve and the axes. The maximum power point is the point on the I-V curve where the area of the resulting rectangle is largest.
- (5) **Fill factor (FF):** This is the ratio of the maximum power point to the product of open circuit voltage (V_{oc}) and the short circuit current (I_{sc}):

$$FF = \frac{V_{max} I_{max}}{V_{oc} I_{sc}} \quad (\text{Eq. 2-8})$$

- (6) **Power conversion efficiency (PCE or η_{eff}):** The ratio of power output to power input. In other words, PCE measures the amount of power produced by a solar cell relative to the power available in the incident solar radiation (P_{in}). P_{in} here is the sum over all wavelengths and is generally fixed at 1000 W/m² when solar simulators are used.

$$\eta_{eff}(\%) = \frac{P_{out}}{P_{in}} \times 100 = \frac{V_{max} J_{max}}{P_{in}} \times 100 = \frac{V_{oc} J_{sc} FF}{P_{in}} \times 100 \quad (\text{Eq. 2-9})$$

where, the V_{oc} (V), J_{sc} (mA/cm²), P_{in} (mW/cm²), and FF represent the open-circuit voltage, short-circuit current density, incident light intensity (100 mW/cm² at STC), and fill factor, respectively.

- (7) **Incident photon to current conversion efficiency (IPCE):** It is defined as the number of electrons flowing through the external circuit divided by the number of photons incident on the solar cell surface at particular wave length λ [48]. In the case of DSSCs, it is defined as the ratio between the observed photocurrent (short circuit current) and by the incident photon flux, uncorrected for reflective losses during optical excitation through the conducting glass electrode. It can also be considered as a product of three components as follows [49,65]

$$IPCE(\lambda) = LHE(\lambda) \Phi_{inj} \eta_{el} = 1,240 \frac{I_{sc}(\lambda)}{\lambda \Phi_{hv}(\lambda)} \quad (\text{Eq. 2-10})$$

where the light harvesting efficiency (LHE) depends on the spectral properties of the dye, charge injection yield (Φ_{inj}) depends on the excited state redox potential and life time, and charge collection efficiency (η_{el}) depends on the structure and morphology of the TiO₂ layer. Further explanation of the different factors of Equation 2.10 can be found in Nazeeruddin et al. IPCE is often referred to as photocurrent action spectrum, spectral response or (external) quantum efficiency [49].

Reliable and comprehensive I-V measurements of DSSCs basically lies on the coincidence of the two curves from the forward and reverse directions of the applied voltage by monitoring the short-circuit photocurrent (I_{sc}). Koide et al. have reported that the dependence of the measurement of the transient photocurrent on the sweep directions and sampling delay time may be explained by the longer time constant of DSSCs [50]. To improve accuracy, measurements should be carried out with a sampling delay time exceeding several seconds. However, it was also found that the average value of the efficiency measured by the two sweeping directions is constant when the sampling delay time is longer than 40 ms.

The fill factor is a important part of the efficiency of the cell. High open circuit voltage and short circuit current are essential in achieving high efficiencies. But paired with a low fill factor, the overall efficiency of the cell will remain low. In the standard condition used for testing of terrestrial solar cells the light intensity is 200 W/m^2 , the spectral distribution of the light source is that of AM 1.5 global standard solar spectrum, and temperature of the cell is 25°C . In practice, special solar simulator light sources are used for the standard measurements. Figure 2-5 shows the solar simulation system installed in our laboratory. In this thesis, the current-voltage (I - V) curves are measured using a source measure unit under irradiation of white light from a 150 W Xenon lamp (K401 CW150 Lamp power supply; McScience Co.). The incident light intensity and the active unit cell area are 100 mW/cm^2 and 0.25 cm^2 .

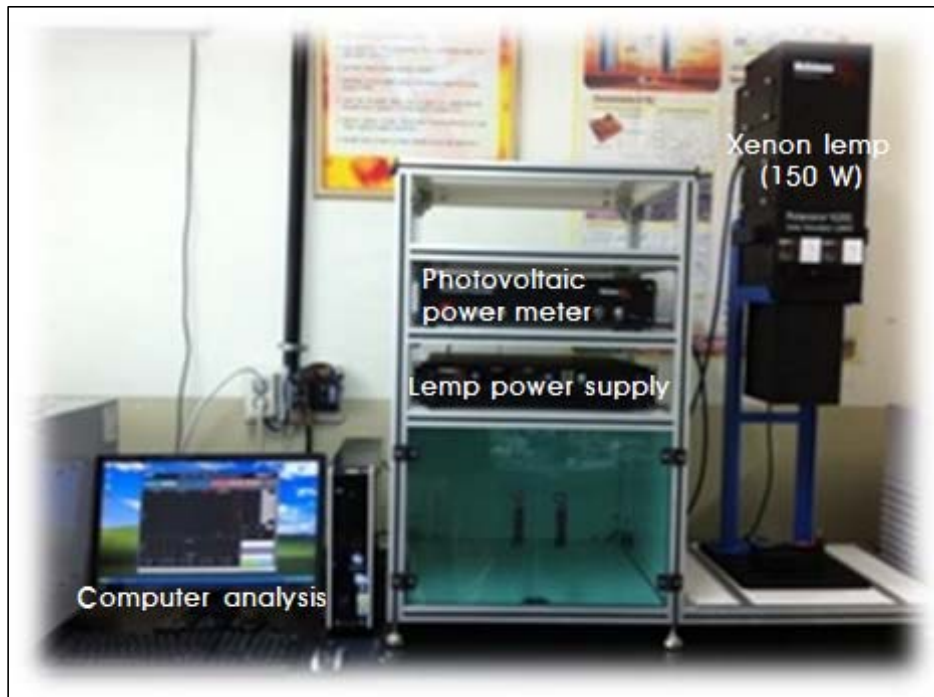


Figure 2-5 A solar simulation system.

2.3 Panchromatic Sensitizers

2.3.1 Light Absorption via MLCT Excitation

The absorption of a photon by the dye molecule happens via an excitation between the electronic states of the molecule. For example the N3 dye has two absorption maxima in the visible region at 518 nm and at 380 nm [49]. The excitation of the Ru complexes via photon absorption is of metal to ligand charge transfer (MLCT) type. Figure 2-6 illustrates Charge transfer process at the metal oxide (TiO₂)/dye interface and electron injection into metal oxide [74-76]. This means that the highest occupied molecular orbital (HOMO) of the dye is localized near the metal atom, Ru in this case, whereas the lowest unoccupied molecular orbital (LUMO) is localized at the ligand species, in this case at the bipyridyl rings. At the excitation, an electron is lifted from the HOMO level to the LUMO level [77]. Furthermore, the LUMO level, extending even to the COOH anchoring groups, is spatially close to the TiO₂ surface, which means that there is significant overlap between the electron wave functions of the LUMO level of the dye and the conduction band of TiO₂. This directionality of the excitation is one of the reasons for the fast electron transfer process at the dye-TiO₂ interface.

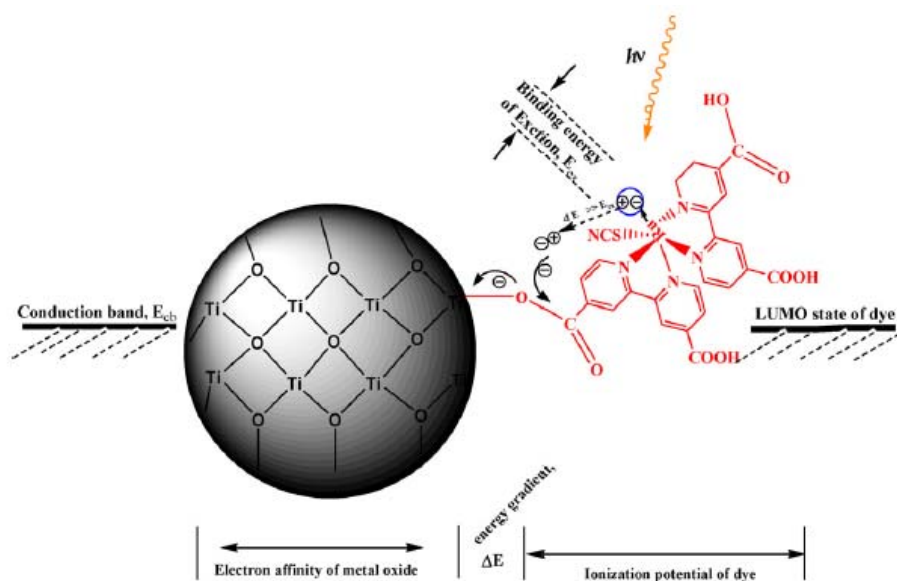


Figure 2-6 Schematic illustration of Charge transfer poceses at the metal oxide (TiO_2)/dye interface and electron injection into metal oxide.

2.3.2 Dye Molecule Sensitizers

The absorption of incident light in the DSSCs is realized by specifically engineered dye molecules placed on the semiconductor electrode surface. To achieve a high light to energy conversion efficiency in the DSSCs, the properties of the dye molecule as attached to the semiconductor particle surface are essential. Such desirable properties can be summarized as:

The dye should absorb light at wavelengths up to about 920 nm, i.e. the energy of the exited state of the molecule should be about 1.35 eV above the electronic ground state corresponding to the ideal band gap of a single band gap solar cell. To minimize energy losses and to maximize the photovoltage, the exited state of the adsorbed dye molecule should be only

slightly above the conduction band edge of the TiO_2 , but yet above enough to present an energetic driving force for the electron injection process. For the same reason, the ground state of the molecule should be only slightly below the redox potential of the electrolyte. The process of electron injection from the excited state to the conduction band of the semiconductor should be fast enough to outrun competing unwanted relaxation and reaction pathways. The excitation of the molecule should be preferentially of the MLCT-type.

The adsorbed dye molecule should be stable enough in the working environment (at the semiconductor-electrolyte interface) to sustain at least 10^8 redox turnovers [77]. The dye molecules are adhered onto the nanostructured TiO_2 electrode by immersing the sintered electrode into a dye solution, typically 0.2 mM in ethanol [48], for a long enough period to fully adsorb the electrode. During the adsorption process the electrode is sensitive to water [78]. To minimize water vapor content inside the pores of the electrode, the electrode should be warm upon immersion to the dye solution. The adsorption process lasts from one to several hours depending on the TiO_2 layer thickness and whether the dye solution is heated or kept in room temperature. The stability of the dye is intrinsically high, because there is no band gap excitation of the TiO_2 semiconductor substrate and therefore no photo-excited hole generation to oxidize the dye [79]. The dye stability becomes an important factor during manufacturing of the cell and during operation. The humidity and water are to be avoided because of their degrading effect on the dye molecules. In addition, UV-light has some deteriorative effect. If the solar cell is manufactured properly, the dye can

last in excess of 20 years [80].

While the high efficiency of the dye sensitized solar cell arises from a collective effect of numerous well-tuned physical-chemical nano scale properties as will become apparent later, the key issue is the principle of dye-sensitization of large band-gap semiconductor electrodes. As already mentioned, in the DSSCs, this is accomplished by coating the internal surfaces of the porous TiO_2 electrode with special dye molecules tuned to absorb the incoming photons. Figure 2-7 represents the molecular structures of three efficient photosensitizers for DSSCs including the so called N3 dye, N719 dye, and the black dye [72]. Figure 2-7 compares the spectral response of the photocurrent observed with the two sensitizers. The incident photon to current conversion efficiency (IPCE) of the DSSCs is plotted as a function of excitation wavelength. Both chromophores show very high IPCE values in the visible range. However, the response of the black dye extends 100 nm further into the IR than that of N3. The photocurrent onset is close to 920 nm, i.e. near the optimal threshold for single junction converters. From there on the IPCE rises gradually until at 700 nm it reaches a plateau of ca. 80%. If one accounts for reflection and absorption losses in the conducting glass the conversion of incident photons to electric currents is practically quantitative over the whole visible domain [81].

The adsorption of the dye to the semiconductor surface usually takes place via special anchoring groups attached to the dye molecule. In the N3 dye these are the four carboxylic groups (COOH) at the end of the pyridyl rings (Figure 2-4). The COOH groups form a bond with the TiO_2 surface by donating a proton to the TiO_2 lattice [77]. The area occupied by one N3

molecule at the TiO_2 surface at full monolayer coverage is 1.65 nm^2 .

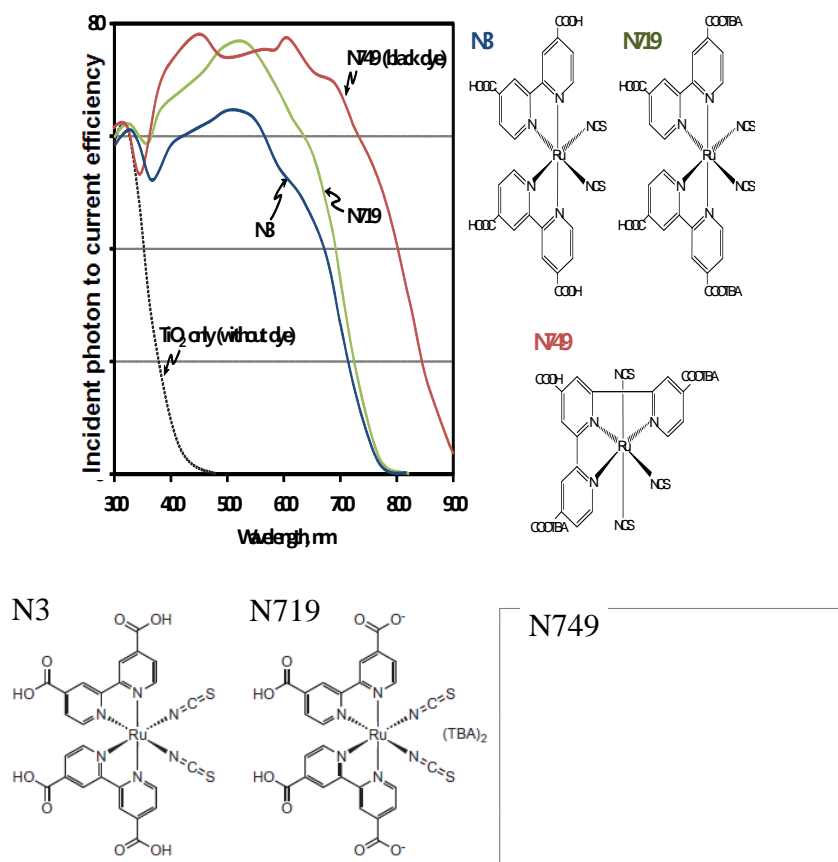


Figure 2-7 Photocurrent action spectra of nanocrystalline TiO_2 films sensitized by N3, N719 and the black dye (N749).

The efficient spectral sensitization in the DSSC is made evident in Figure 2-7, where the spectral response (IPCE) curves, i.e. the photon to current efficiency curves, for cells sensitized with different dyes is compared with a naked TiO_2 electrode. The actual sensitization effect can be seen in Figure 2-7 as a shift of the IPCE curve of the naked TiO_2 to the higher

wavelength when coated with the dye. The current efficiency of the cell is related to the 'height' of the IPCE curve, which depends on the charge separation and charge collection efficiencies. The IPCE curves in Figure 2-7 are not corrected for the optical losses in the glass substrate, which only makes the obtained peak IPCE values more significant.

The incident monochromatic photon-to-current conversion efficiency (IPCE), sometimes referred to also as the “external quantum efficiency” (EQE), is an important characteristic of a device. In particular, using devices with same architecture, it is possible to compare the light-harvesting performance of sensitizers. It is defined as the number of electrons generated by light in the external circuit divided by the number of incident photons as a function of excitation wavelength.

2.4 Interfacial Principle of DSSCs

2.4.1 Interfacial Kinetics

Figure 2-8 shows control of electron injection and transport at the materials interfaces that can be at the core of the DSSCs design. The materials interfaces such as on three core elements (i) metal oxide, (ii) dye sensitizer, and (iii) metal oxide/dye/electrolyte interface, is that influence efficient electron injection and transportation, especially which are mainly determinants in the overall performance of DSSCs [82].

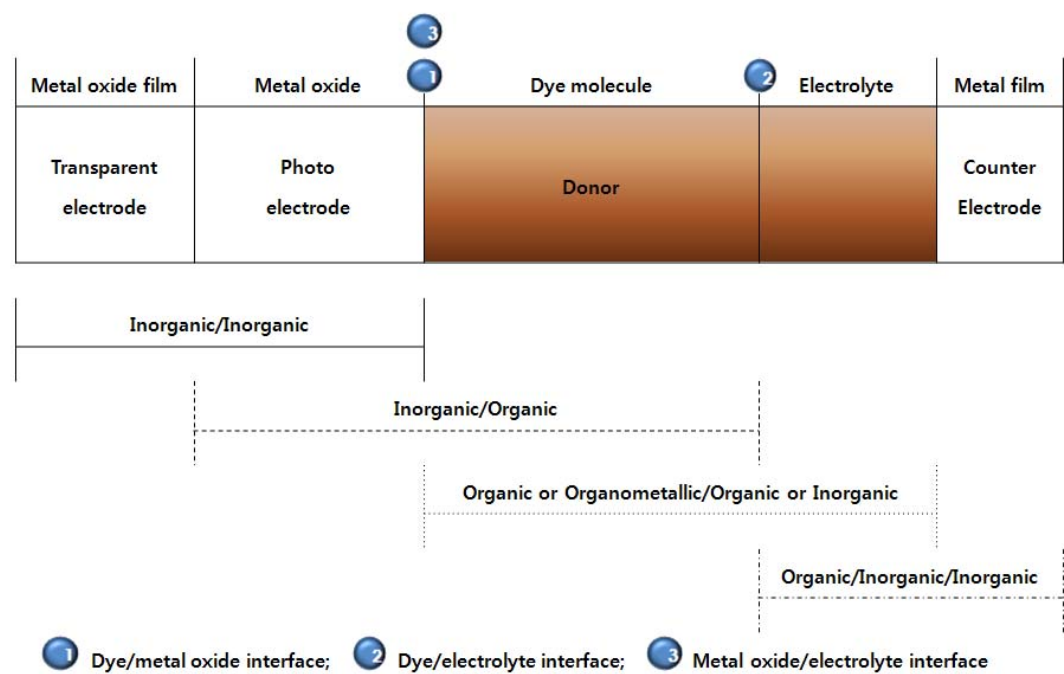


Figure 2-8 Combination of materials and interfaces involved in DSSCs.

The DSSCs are based on photoelectrochemical reactions at the semiconductor-electrolyte interface, and depending on the operation of the cells, it is due to competition of the chemical reactions with the other rate constants. Dye molecules of a DSSCs are chemisorbed on a TiO₂ porous layer surface and visible light is absorbed by the sensitizer dye to generate excited electrons. Electron injection from the excited state of the dye into the conduction band of the TiO₂ is followed by the subsequent regeneration of the dye by an I⁻/I₃⁻ redox couple. Efficient operation of a DSSCs device relies on minimization of the possible recombination pathways occurring at the TiO₂/dye/electrolyte interface to allow efficient charge transport through the TiO₂ porous layer and subsequent charge collection at the device contacts [83,84].

2.4.2 Charge Transport

In the DSSCs charge transport happens by electron transport in the nanostructured TiO₂ electrode and hole transport in the electrolyte as I₃⁻. Although the electron transport process has attracted an intensive study due to several interesting fundamental questions concerning it, both charge transport mechanisms are equally important for the operation of the solar cell.

Electron Transport in the Nanostructured Semiconductor Electrode

The semiconductor nanoparticle network works not only as a large surface area substrate for the dye molecules but also as a transport media for the electrons injected from the dye molecules.

Because of the porous structure of the electrode and the screening effect

of the electrolyte, the electrode can be viewed as a network of individual particles through which electrons percolate by hopping from one particle to the next [77]. As mentioned above, the small size of the particles prevents the formation of a space charge layer and a built-in electric field inside the particles, and therefore the transport of electrons cannot be drift in an electric field. Recombination processes being efficiently blocked at the semiconductor electrolyte interface the generation of electrons to the conduction band of the TiO_2 particles under illumination results in an electron concentration gradient in the electrode and the electrons are transferred to the transparent conducting oxide (TCO) back contact layer by diffusion.

Measurements have shown that the diffusion of electrons is characterized by a distribution of diffusion coefficients, which have been related to hopping of electrons via surface traps of different depths [77]. These electron traps are localized energy states just below the conduction band edge of the TiO_2 and they play a significant role in the electron transport. Because of the majority carrier nature of the TiO_2 electrode, trapping of electrons in the bulk states does not lead to recombination losses. Instead trapping of electrons at the TiO_2 surface may be a pathway for recombination, resulting in photocurrent losses and also photovoltage losses for kinetic reasons [49]. In addition, the trap states will lead to a lower quasi-Fermi level for the electrons under illumination and thus to a reduced photovoltage [49].

The diffusion coefficient of electrons depends on the electron quasi-Fermi level under illumination. At low light conditions only deep traps participate in the electron transport causing a low diffusion coefficient. Increasing the

light intensity raises the electron quasi-Fermi level and deep traps are filled at steady state condition, while shallow traps contribute to the electron motion, resulting in a larger diffusion coefficient [77]. Increasing the illumination level thus increases the conductivity of the TiO_2 electrode by filling the trap states.

It has also been suggested that the motion of the electrons in the semiconductor particles is coupled to the species in the electrolyte at the semiconductor-electrolyte interface [77]. Cahen et al. [85] calculated that the screening by the electrolyte keeps the electrons near the particle surface, consistently with the picture of electron transport via surface electron traps. The electron together with its screening charge in the electrolyte side of the particle surface can be viewed as a polaron moving by the electron diffusion towards the back contact where the electron is subsequently separated.

All in all, the picture of the electron transport in the nanostructured electrode of the DSSCs is presently incomplete and a lot of basic research has to be done. Understanding the mechanisms of charge transport in the nanostructured electrode electrolyte systems is important for the further development of the dye-sensitized nanostructured solar cell concept and especially for designing cells with solid polymer or gel electrolytes.

Ion Transport in the Redox Electrolyte

The electrolyte in the DSSCs is usually an organic solvent containing the redox pair I^-/I_3^- , which in this case works as a hole-conducting medium. At the TiO_2 electrode the oxidized dye, left behind by the electron injected to the TiO_2 , is regenerated by I^- in the electrolyte while at the counter-electrode I_3^- is reduced to I^- . In other words, I_3^- is produced at the

TiO₂ electrode and consumed at the counter electrode and thus diffused across the electrolyte correspondingly. This is why I₃⁻ is often labeled as the hole carrier to draw similarities with the conventional *pn* junction solar cells. Similarly, I⁻ is produced at the counter-electrode and diffused to the opposite direction in the electrolyte.

The most simple way of dealing with the electrolyte might be to think it as an essentially neutral sink of I⁻ and I₃⁻ at the electrodes and maintaining the redox potential in the bulk of the electrolyte via the fast redox reaction of the I/I₃⁻ pair. This redox reaction in the electrolyte is a two-electron reaction [86]. The redox electrolyte chemistry appears to be a more or less standard and established area of chemistry, or at least it is only rarely discussed in much more detail than this in conjunction with DSSC research reports in the literature.

A schematic of energy level diagram describing the charge transfer processes involved in DSSCs is shown in Figure 2-9 [87]. It is to be noted that the rate of electron injection is significantly contributed from unthermalized excited state and plays major role in the electron injection efficiency[88,89].

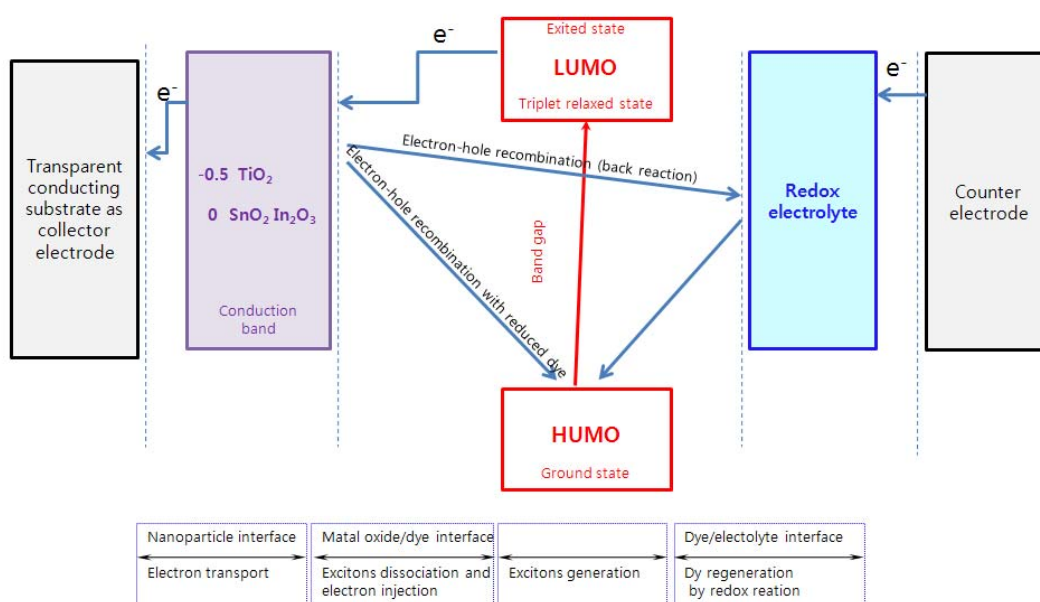


Figure 2-9 A schematic of energy level diagram for metal oxide/dye/electrolyte interfaces.

2.4.3 Charge Recombination

Charge recombination between dye cations and injected photoelectron occurs quickly on its way to the electrical back contact. The wide range of recombination time is usually attributed to the trapping of electrons by localized states on the semiconductor surface [90-93].

Experiments, which can be controlled by changing the intensity of the light source or the surrounding electrolyte composition, or by applying the external bias, were able to get strong sensitivity of the recombination rate to the occupancy of trap levels [90].

Illumination of the dye-sensitized electrode initially in equilibrium (in the dark) generates a transient electric field between the injected electrons in the

TiO₂ and the oxidized species in the electrolyte. This electric field could in principle oppose further charge separation and promote recombination. However, in the dye cell the mobile ions in the electrolyte can easily rearrange and effectively screen the light induced opposing fields in steady state conditions through out the electrode film, and thus enable an efficient charge separation [94].

In the absence of holes in the semiconductor particles, the recombination occurs mostly by loss of electron to an oxidized dye molecule or to a hole in the electrolyte, i.e. the oxidized triiodide. The former process is negligible, as assumed in most electrical models of the cell, but may be important in near open circuit conditions, i.e. in the case of the accumulation of electrons into the TiO₂ particles [95]. The latter recombination pathway on the other hand, is made inefficient by reaction kinetic reasons. According to Huang et al. the net recombination reaction at the TiO₂-electrolyte interface is a two electron reaction [96]

The last of which is a slow dismutation reaction and rate limiting in the net recombination reaction. The reaction equation 2.12 also tells, that the actual electron acceptor in the recombination reaction is I₂. Because of the porous structure of the electrode the conducting glass substrate may be partly exposed to the electrolyte setting up a potential recombination pathway between electrons in the conducting substrate and hole carriers in the electrolyte. However, there is experimental evidence that this effect is insignificant, most likely due to low electrocatalytic activity of Pt-free SnO₂:F (FTO, as well as ITO) surface for the iodine/triiodide redox system [85].

Chapter III. Experimental Procedure

3.1 Preparation of Materials for DSSCs

3.1.1 TiO₂ Particle by Sol-gel Method

The nanoparticles of titanium dioxide were synthesized by sol-gel method in which the sol was obtained through hydrolysis of titanium isopropoxide (TIP, Junsei Chemical Co., >98%). The formation of TiO₂ nanoparticles through hydrolysis take place based on the following reactions:



Figure 3-1 shows the schematic diagram for the synthesis of nanocrystalline TiO₂ particles by sol-gel method. TIP was used as a main starting material without further purification. An appreciated amount (20 mL) of TIP was slowly dropped in ethanol (200 mL) at room temperature for 5 min. Consequently, a drop-wise addition of hydrochloric acid solution (0.05 M) into the TIP solution was conducted for 24 h under vigorous stirring condition. The suspension was then ultrasonicated at room temperature for 1 h and centrifugated at 4 °C and 8,000 rpm for 20 min. The white precipitate formed was filtered and dried at room temperature for 1 h. After the TiO₂ sol was drying, this was finally calcined in a furnace at the temperature in the range of 250-700 °C for 3 h, the TiO₂ particles was made.

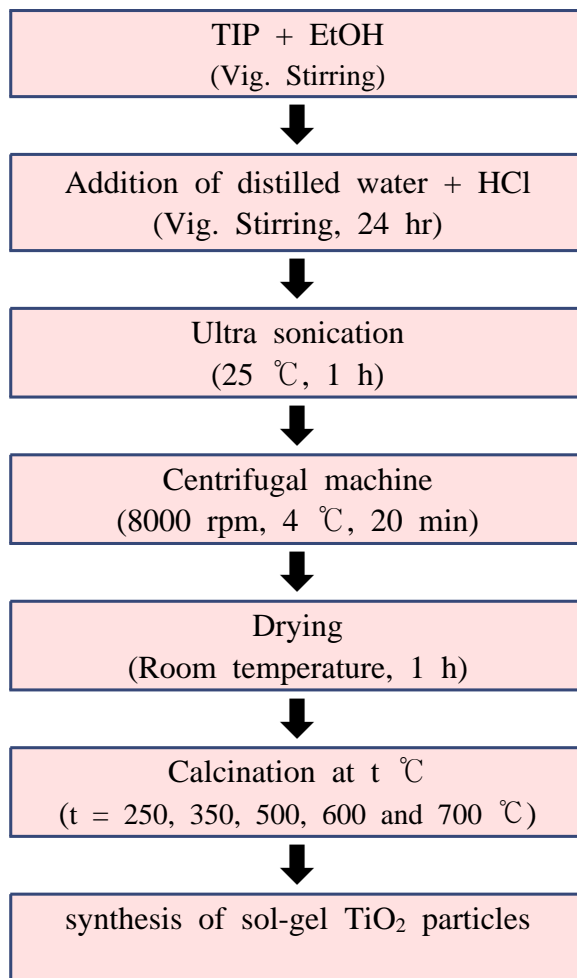


Figure 3-1 Experimental procedure for preparation of the TiO₂ nanoparticles by sol-gel method.

X-ray diffraction is a non-destructive analytical technique which reveals information about the crystallographic structure, chemical composition, and physical properties of materials and thin films. It is based on observation of the scattered X-ray beam after hitting a sample as a function of incident and scattered angle, polarization, and wavelength or energy. The X-ray diffraction data was obtained with an X'Pert PRO MPD (PANalytical)

SEM(S4800, Hitachi Ltd, Japan) is a microscope that uses electrons instead of light to form an image. The scanning electron microscope has many advantages over traditional microscopes. The SEM has a large depth of field, which allows more of a specimen to be in focus at one time. The SEM also has much higher resolution, so closely spaced specimens can be magnified at much higher levels. Because the SEM uses electromagnets rather than lenses, the researcher has much more control in the degree of magnification. Field-emission scanning electron microscope provides ultra high resolution images down to 1nm resolution thanks to the inherent brightness of the field emission electron gun. Morphology and surface of TiO₂ particles were analyzed.

X-ray photoelectron spectroscopy (XPS) analysis was conducted using a photoelectron spectrometer (VG Scientific MultiLab 2000 system) equipped with a non-monochromatic Mg *ka* radiation of 1,253.6 eV. The C1s peak (285.0 eV) was used to calibrate the binding energy values.

3.1.2 Electrospun TiO₂ Nanofibers

For the preparation of TiO₂ nanofiber, titanium isopropoxide (TIP) was directly added to an alcohol solution containing polyvinylpyrrolidone (PVP) to prepare TiO₂/PVP composite nanofibers. PVP was selected as the base polymer because of its good solubility in alcohols and acetic acid and its compatibility with some titania precursors. In addition to PVP solution in ethanol, acetic acid had to be added to stabilize the solution and to control the hydrolysis reaction of the sol-gel precursor. In a typical procedure, 6 mL of TIP was mixed with 12 mL of acetic acid and 12 mL of ethanol. After 60 min, this solution added to 30 g of ethanol that contained 10 wt % PVP, followed by magnetic stirring for 24 hr. The mixture was immediately loaded into a glass syringe equipped with a 21 G needle made of stainless steel. The needle was connected to a high voltage supply (DC power supply PS/ER 50R06 DM22, Glassman High Voltage Inc., USA) that is capable of generating DC voltages up to 50 kV. The flow rate (100 μ L/min) for the precursor spinning solution was controlled using a syringe pump (200 series, KD Scientific Inc., USA). Aluminum foil was placed 15 cm of TCD (tip-to-collector distance) to collect the nanofibers. Electro spinning process was carried at the room temperature. The TiO₂ nanofibers were calcined at 500 $^{\circ}$ C for 1 hr. The procedure of electrospun TiO₂ nanofiber was shown in Figure 3-2.

The morphology of TiO₂ nanofibers were observed by field emission scanning electron microscopy (FE-SEM) (Hitach, S-4800). X-ray diffraction (XRD) pattern was recorded using a Philips (X'Pert PRO MPO) diffractometer (Cu Ka radiation).

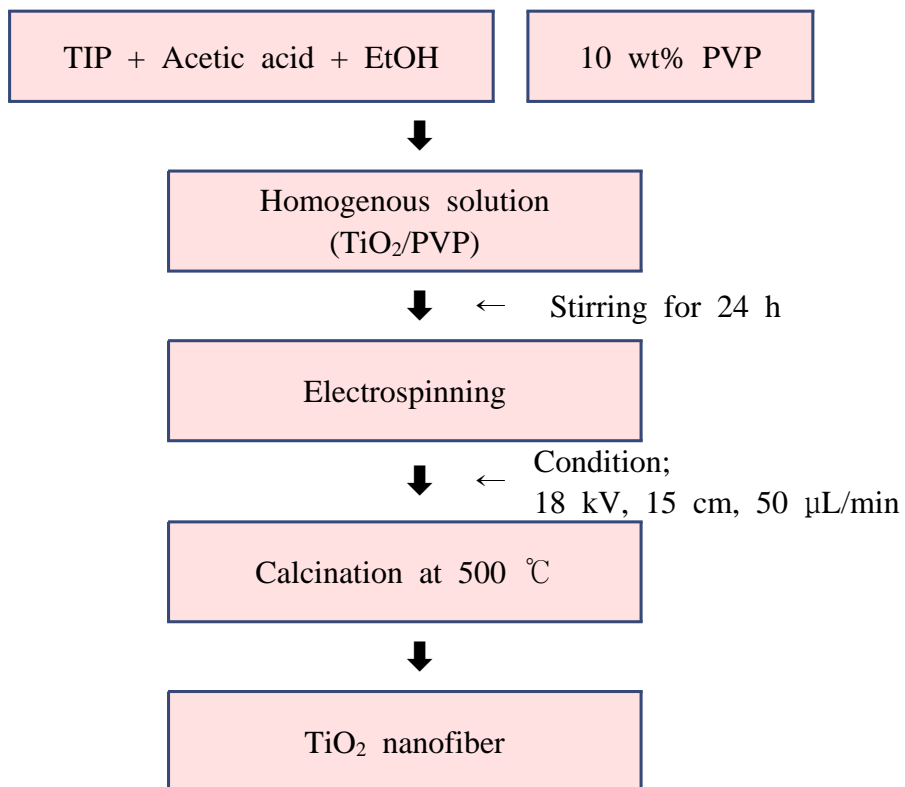


Figure 3-2 Experimental procedure for preparation of the TiO₂ nanofiber by electrospinning method.

3.1.3 Electrospun Al₂O₃ Nanofibers

The polymer polyvinylpyrrolidone (PVP) (MW=1300000; Kanto, Japan), aluminum isopropoxide (AIP) (C₉H₂₁O₃Al) (>97.0%; Sigma-Aldrich), ethanol (94.0%; Daejung, Korea), and nitric acid (60%; Daejung, Korea) were obtained commercially and used as-received without further purification. All the equipment used in the study was thoroughly cleaned prior to the experiments.

A typical synthesis run was as follows: A certain amount of nitric acid and 10 mmol of the aluminum precursor AIP were added to 20 mL of ethanol, and the solution stirred vigorously. The final composition of the mixed solution was such that the molar ratio of AIP: nitric acid: ethanol was 1:m:34, where m (=2.57) is the molar ratio of the acid (HNO₃) to the alkoxide [97]. The mixture was covered with polyethylene (PE) film and then stirred vigorously at room temperature for at least 5 h. The PVP solution (10 wt%) was prepared by dissolving the PVP polymer powder in ethanol under constant and vigorous stirring. The weight ratio of the polymer to the aluminum precursor was maintained at 3:1 (Figure 3-3).

The AIP and PVP solutions were then mixed, and the resulting AIP/PVP solution was loaded into a 10 mL syringe (SGE LL type) that was fitted with a metallic needle. The positive terminal of a variable high-voltage power supply was connected to the metallic needle and the negative terminal to a rotating collector (speed = 200 rpm) that was covered with the aluminum foil and served as the counter electrode. During a typical procedure, the voltage and the feeding rate were kept at 15 kV and 3.0 mL/h, respectively. The distance between the needle tip and the collector

was maintained at 15 cm. The relative humidity was controlled and maintained between 35-45 % at room temperature (Figure 3-4).

After the electrospinning was complete, the as-spun nanofibers were dried at 80 °C for 24h. Some of the dried nanofibers were used for the characterization by TGA, SEM, FTIR spectroscopy, and XRD analysis. The remaining as-spun AIP/PVP composite nanofibers were calcined at 800 °C and at 1200 °C for 2 h each at a heating rate of 5 °C/min in order to obtain pure alumina nanofibers.

As mentioned previously, the morphology of the fibers was examined by SEM (S4800, Hitachi Ltd, Japan). The diameter of the nanofibers were calculated from the SEM images using the Image J (National Institutes of Health, USA) software. The X-ray diffraction data was obtained with an X'Pert PRO MPD (PANalytical) diffractometer using Cu K α radiation. FT-IR spectroscopy was performed on the samples using a NICOLET6700 (Thermo Scientific) spectrometer that had a KBr beam splitter (operational wavelength range = 7800-350 cm⁻¹). TGA was performed using a thermogravimetric analyzer (TGA2050, TA Instruments) in air with a heating rate of 10 °C/min.

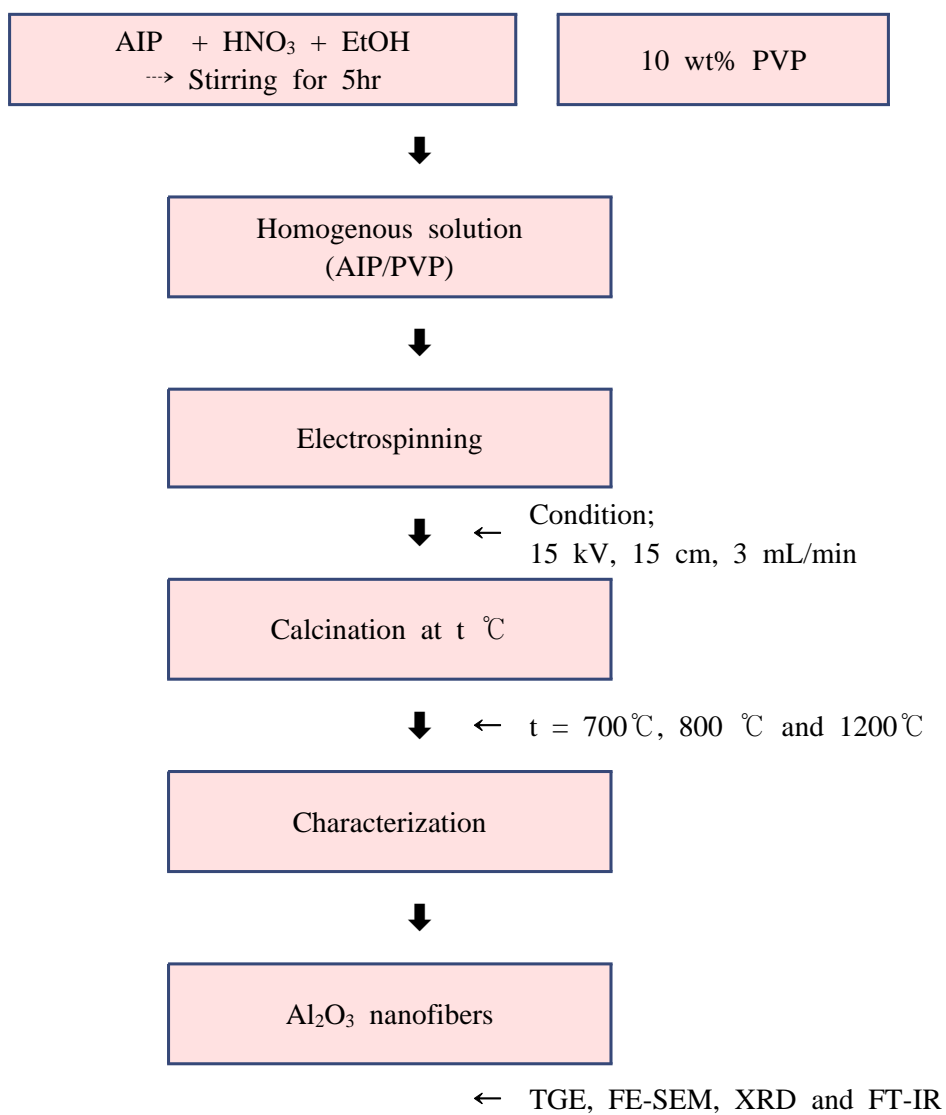


Figure 3-3 Flow chart of the preparation of alumina nanofibers.

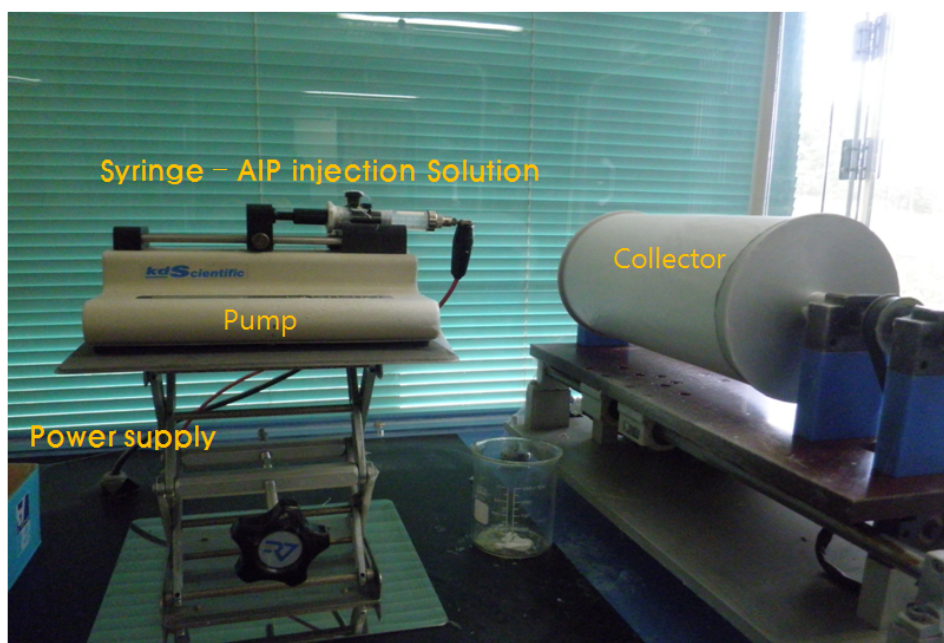


Figure 3-4 Schematic diagram of the electrospinning apparatus.

3.2 Preparation and Measurement of DSSC

3.2.1 Preparation of DSSC

Table 3-1 shows experimental condition of Dye-sensitized solar cell for this study.

Table 3-1 Experimental condition of DSSC

Items	Parameters
Electrode	TiO ₂ particle (P25)
	TiO ₂ particle (by sol-gel method)
	Dopant TiO ₂ nanofiber (by electrospinning; ~ 1.5 %)
	Al ₂ O ₃ nanofiber (by electrospinning; ~ 1.5 %)
Dye	N719
Electrolyte	0.3 M 1,2-dimethyl-ε-propyl imidazolium iodide
	0.5 M LiI
	0.05 M I ₂ (Aldrich Co.)
	0.5 M 4-TBP
	3-MPN
Counter electrode	Pt-Catalysts T/SP, Solaronix Co.
Substrate	FTO glass
	(fluorine-tin-oxide, TEC 8Ω/sq)

3.2.1.1 Thin Film

The preparation of nanocrystalline TiO₂ thin films was first developed by Grätzel's research [80]. Grätzel et. al. introduced a preparation method of TiO₂ nano powder consisting of sol-gel synthesis and hydrothermal treatment [98]. In a typical sol-gel experiment, titanium isopropoxide (125 mL) was added drop wise at room temperature to 0.1 M nitric acid solution (750 mL) under vigorous stirring. A white precipitate formed instantaneously. After that, the slurry was heated to 80 °C and stirred vigorously for 8 h. To achieve peptization (i.e., destruction of the agglomerates and redispersion into primary nanocrystallites), the solution upon filtration to remove non-peptized agglomerates was diluted with water to adjust the final solids concentration to ~5 % [W/V].

Preparation of the photoanode involves deposition of the TiO₂ nanoparticles on fluorine-doped tin oxide (FTO) glass, sintering/annealing, post-treatment and sensitization. Nanoparticle deposition most commonly involves preparation of a paste and application by doctor-blade [66] or screen printing [99].

In typical method, the fabrication scheme for TiO₂ mixtures pastes is shown in Figure 3-5. First the nanotitania particles are manually ground after mixing with acetic acid, water and ethanol. The TiO₂ slurry is transferred with the excess ethanol to a beaker where it is magnetically stirred and then homogenized using a sonicator. This is filled with the addition of a mixture of anhydrous terpeneol and a mixture of ethyl cellulose and ethanol by stirring and sonication again. Finally, the contents are concentrated by evaporation [100].

The TiO_2 powder is initially dispersed by grinding with dispersion agent and followed by the addition of distilled water and a wetting agent. The binder such as hydroxypropyl cellulose (Aldrich Co.) is also used. The paste is then spread with doctor blade or screen printing onto the FTO glass ($10 \Omega/\text{cm}^2$, Pilkington Co.). At that time, TiO_2 thin film is formed a thickness of $50 \mu\text{m}$ to $100 \mu\text{m}$. Also, the TiO_2 thin film coated thus on the FTO glass is $0.5 \text{ cm} \times 0.5 \text{ cm}$ (0.25 cm^2) in size. The fabricated TiO_2 thin film is sintered at 500°C for 1 h. The sintering rate should be very slow. In the temperature interval $200 < T < 350^\circ\text{C}$, organic materials such as dispersant and organic solvents used during the TiO_2 film deposition stage decompose.

The decomposition process induces mechanical stress into the TiO_2 layer. If the heating is done too fast, the adhesion to the FTO substrate is not firm. Consequently, cracks form within the layer and the film becomes brittle. The cooling rate of the sintered TiO_2 electrode also needs to be slow in order to minimize the stress within the TiO_2 layer. Finally, sintered TiO_2 thin film has a thickness of $5 \mu\text{m}$ to $10 \mu\text{m}$. The performance of the TiO_2 layer can be further improved by adding a further layer of TiO_2 after sintering (i.e., Multi layer coating) [101].

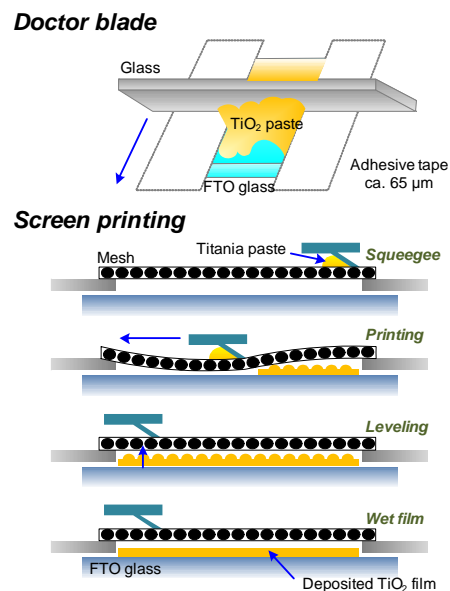
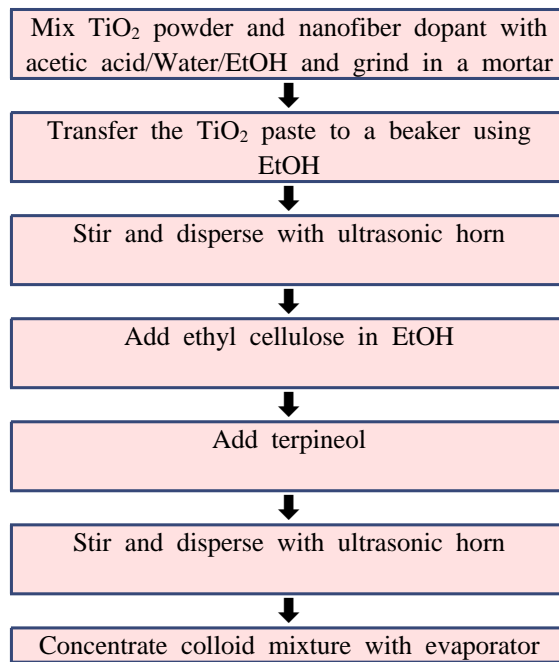


Figure 3-5 The typical preparation for TiO_2 paste and the various coating method for the fabrication of nanocrystalline TiO_2 thin film.

3.2.1.2 Electrode

(1) TiO₂ Particle Electrode

For the preparation of nanostructured TiO₂ electrode, TiO₂ paste was prepared by mixing of 2 g TiO₂ particles, 0.68 mL 10 %[V/V] acetyl acetone and 1 g hydroxy-propylcellulose (HPC, Mw. 80,000 g/mol, Aldrich Co.) in 10.68 mL water for 12 h at 300 rpm using a ZrO₂ ball mill (Planetary mono mill, Fritsch Co.). A TiO₂ film was fabricated by coating a precursor paste onto the FTO glass plates (15 Ω/cm^2 , Asahi glass Co.) by using a doctor blade technique (adhesive tape was used as spacer of ca. 65 μm thickness).

Based on the thermal gravity analysis (TGA) report (Figure 3-6), the sol-gel TiO₂ film heated at 500 $^{\circ}\text{C}$ for 2 h for the complete removal of HPC. Thus, The sol-gel TiO₂ film formed on the FTO glass was 4-5 μm thickness and 0.5 cm \times 0.5 cm size. To fabricate the DSSCs, the prepared thin film electrode was immersed in the N719 dye (Solaronix Co.) solution of 0.3 mM at 20 $^{\circ}\text{C}$ for 12 h followed by rinsing with an anhydrous ethanol and drying. Pt coated FTO glass (15 Ω/cm^2 , Asahi glass Co.) electrode was prepared as a counter electrode with an active area of 0.25 cm^2 . The Pt electrode was placed over the dye-adsorbed TiO₂ electrode, and the edges of the cell were sealed with 5 mm wide stripers of 60 μm thick sealing sheet (SX 1170-60, Solaronix Co.). The sealing was accomplished by hot pressing the two electrodes together at 80 $^{\circ}\text{C}$. The redox electrolyte pass into the cell through the small holes and it was sealed with a small square of sealing sheet. The redox electrolyte consists of 0.3 M 1,2-dimethyl-3-propyl imidazolium iodide (Solaronix Co.), 0.5 M LiI (Aldrich

Co.), 0.05 M I_2 (Aldrich Co.), and 0.5 M 4-TBP (Aldrich Co.), and 3-MPN (Fluka Co.) as a solvent.

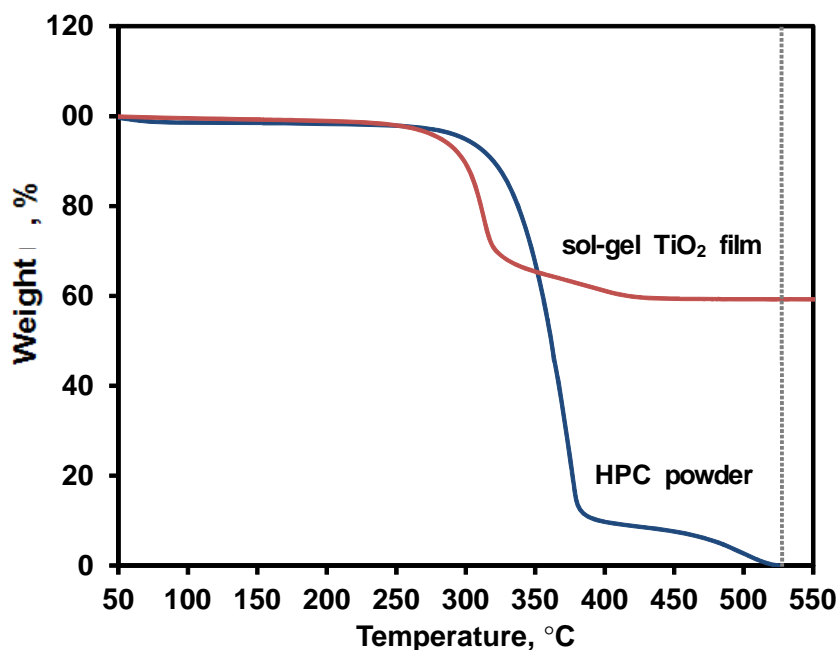


Figure 3-6 TG analysis of sol-gel TiO_2 film and HPC powder.

(2) TiO_2 Nanofiber Dopant

For the preparation of TiO_2 nanofiber doped TiO_2 thin film, TiO_2 slurry was prepared by mixing of 2 g synthesized TiO_2 particles [102], 0.68 mL 10 %[V/V] acetylacetone, 1g hydroxypropylcellulose (Mw.80,000, Aldrich), and 10.68 mL water for 20 h at 300 rpm using a paste mixer (PDM-300, Korea mixing technology Co.). Thus, synthesized TiO_2 film was fabricated by a coating of blended paste on to the fluorine-doped SnO_2 conducting glass

plates (FTO, $10 \Omega/\text{cm}^2$, Asahiglass Co.) by using as squeeze printing technique (adhesive tape was used as spacer of ca.65 μm thickness). The TiO_2 film was heat-treated at 500 $^\circ\text{C}$ for 1h. Then, the TiO_2 film formed on the FTO glass was 7 μm thickness and 0.5 cm \times 0.5 cm in size. TiO_2 thin film which is prepared from the anatase crystalline phase has transparency, dispersibility and high efficiency for photoelectrode. The TiO_2 thin film was prepared under the different addition ratio of the TiO_2 nanofibers (0.5~1.5 wt%) for photoelectrode with high efficiency.

(3) Al_2O_3 Nanofiber Dopant

For the preparation of Al_2O_3 nanofiber doped TiO_2 thin film, TiO_2 slurry was prepared by mixing of 2 g synthesized TiO_2 particles [102], 0.68 mL 10% [V/V] acetylacetone, 1 g hydroxypropylcellulose (Mw.80,000, Aldrich), and 10.68 mL water for 20 h at 300 rpm using a paste mixer (PDM-300, Korea mixing technology Co.). Thus, synthesized TiO_2 film was fabricated by a coating of blended paste on to the fluorine-doped SnO_2 conducting glass plates (FTO, $10 \Omega/\text{cm}^2$, Asahiglass Co.) by using as squeeze printing technique (adhesive tape was used as spacer of ca.65 μm thickness). The TiO_2 film was heat-treated at 500 $^\circ\text{C}$ for 1h. Then, the TiO_2 film formed on the FTO glass was 7 μm thickness and 0.5 cm \times 0.5 cm in size. TiO_2 thin film which is prepared from the anatase crystalline phase has transparency, dispersibility and high efficiency for photoelectrode. The TiO_2 thin film was prepared under the different addition ratio of the Al_2O_3 nanofibers (0.5~1.5 wt%) for photoelectrode with high efficiency.

The film thickness and surface morphology of metal oxide nanofiber

doped TiO₂ electrode were measured by field-emission scanning electron microscope (FE-SEM; S-4700, Hitachi Co.). X-ray photoelectron spectroscopy (XPS) analysis was conducted using a photoelectron spectrometer (VG Scientific MultiLab 2000 system) equipped with a non-monochromatic Mg *k* α radiation of 1,253.6 eV. The C1s peak (285.0 eV) was used to calibrate the binding energy values.

3.2.1.3 Dye

One of the first dye that was introduced with the nonocrystalline solar cell was cis-RuL₂-(NCS)₂, where L stand for 2,2'-bipyridyl- 4,4'-dicarboxylic acid, the dye is also known as N3. It sensitizes very efficiently wide band-gap oxide semiconductors, like titanium oxide, up to a wavelength of 750 nm. A two-fold deprotonated form of N3, called N719 [cis-bis(isothiocyanato)bis(2,2'-bipyridyl-4,4'-dicarboxylato)-ruthenium(II)bis-tetrabutylammonium dye, Solaronix Co.], was used in this work (Mw.: 1,185.5 g/mol).

The dye molecules are adhered onto the nanostructured TiO₂ electrode by immersing the sintered electrode into a dye solution, typically 0.2 mM in ethanol [48], for a long enough period to fully adsorb the electrode. During the adsorption process the electrode is sensitive to water [78]. To minimize water vapor content inside the pores of the electrode, the electrode should be warm upon immersion to the dye solution. The adsorption process lasts from one to several hours depending on the TiO₂ layer thickness and whether the dye solution is heated or kept in room temperature. The stability of the dye is intrinsically high, because there is no band gap

excitation of the TiO_2 semiconductor substrate and therefore no photo-excited hole generation to oxidize the dye [103]. The dye stability becomes an important factor during manufacturing of the cell and during operation. The humidity and water are to be avoided because of their degrading effect on the dye molecules. In addition, UV-light has some deteriorative effect. If the solar cell is manufactured properly, the dye can last in excess of 20 years [80].

3.2.1.4 Electrolyte

Between the TiO_2 electrode and the counter electrode is the electrolyte. The electrolyte used in the DSSCs consists of iodine (I) and triiodide (I_3^-) as a redox couple in a solvent with possibly other substances added to improve the properties of the electrolyte and the performance of the operating DSSC. Since the discovery of the DSSC about ten years ago [52] no redox couple preceding the performance of the I/I_3^- couple in the DSSC has been discovered [104]. The I/I_3^- redox electrolyte is prepared by adding I_2 to the solvent together with some iodine salt such as KI [52], LiI [104]. A recent report by Wolfbauer et al. [104] clearly highlights the importance of the cation of the iodine salt to the performance of the DSSC. The photocurrent output was found to increase linearly with decreasing cation radius, the smallest cations Li^+ and K^+ showing the best performance. The results also showed that the relative concentration of I_3^- to I in the electrolyte is an important factor to the cell performance.

Examples of the solvents used in the electrolytes in DSSCs are: acetonitrile (ACN) [52], methoxyacetonitrile (MAN) [104], methoxypropionitrile

(MPN) [105]. The solvent in electrolyte used already in the early DSSC, ACN, seems to be still the best choice when the cell efficiency is to be maximized. However, with respect to the preferred solvent properties listed above, acetonitrile immediately fails at least in two points. Firstly, it is highly volatile with boiling point of 82 °C, which is about the maximum temperature that a roof-top solar cell can reach at full sunlight [106], and due to the high volatility it easily escapes from the cell through the sealing. Secondly, acetonitrile is highly toxic and carcinogenic chemical and cannot be used in the commercial DSSC. The choice of solvent is thus always a trade-off between low viscosity with better ion diffusion properties and high viscosity with ease of manufacturing and less stringent sealing requirements [107]. The MPN seems arise as a potential candidate for the commercial DSSCs. In contrast to ACN it is nontoxic and has a boiling point of 160 °C.

The 3-methoxypropionitrile (3-MPN, Fluka Co.) was used in this work. The performance achievable with ACN is nevertheless greater due to lower viscosity. In this work, the used redox electrolyte consists of 0.3 M 1,2-dimethyl-3-propyl imidazolium iodide (Solaronix Co.), 0.5 M LiI (Aldrich Co.), 0.05 M I₂ (Aldrich Co.), and 0.5 M 4-tert-butylpyridine (4-TBP, Aldrich Co.) and 3-MPN as a solvent.

3.2.1.5 Counter Electrode

The function of the counter electrode is the reduction of triiodide to iodide. The plain SnO₂:F (FTO) layer does this rather poorly, so a small amount of platinum (Pt) is deposited to the electrode to fast catalyze the

kinetic reaction. Charge transfer resistance, R_{ct} , is a measure of the electrodes performance in an electron transfer process. The platinized counter electrode has a charge transfer resistance of ca. $1 \Omega/\text{cm}^2$, while the resistance of the plain electrode is seven orders of larger magnitude [105,108]. In this work, Pt-sol (Pt-catalyst T/SP, Solaronix Co.) was used. Pt counter electrodes were prepared by doctor blade or screen printing of Pt-sol on to FTO glass (TEC 8: $10 \Omega/\text{cm}^2$, Pilkington Co.) and successive sintering at 450°C .

3.2.1.6 Substrate

The electrodes of the standard DSSC are prepared onto TCO coated glass substrates, between which the cell is assembled. The conducting coating of the substrate works as a current collector and the substrate material itself both as a support structure to the cell and as a sealing layer between the cell and the ambient air. Fluorine-doped tin oxide ($\text{SnO}_2\text{:F}$) and indium tin oxide ($\text{In}_2\text{O}_3\text{:Sn}$ or ITO) are the most frequently used TCOs in thin film photovoltaic cells. The standard preparation procedure of the nanostructured TiO_2 electrode includes sintering of the deposited TiO_2 film at $450\sim 500^\circ\text{C}$. As the only TCO coating stable at these temperatures [109], the $\text{SnO}_2\text{:F}$ (TEC 8: $10 \Omega/\text{cm}^2$, Pilkington Co.) has been the material of choice in this work.

3.2.1.7 Fabrication of Dye-sensitized Solar Cell

To fabricate the DSSCs, the prepared sol-gel TiO_2 particle, TiO_2 nanofiber and Al_2O_3 nanofiber thin film electrode was immersed in the

N719 dye solution of 0.3 mM at 20 °C for 12 h, rinsed with anhydrous ethanol and dried. Pt coated FTO glass electrode was prepared as a counter electrode with an active area of 0.25 cm². The Pt electrode was placed over the dye-adsorbed TiO₂ electrode, and the edges of the cell were sealed with 5 mm wide stripers of 60 µm thick sealing sheet (SX 1170-60, Solaronix Co.) (Figure 3-7).

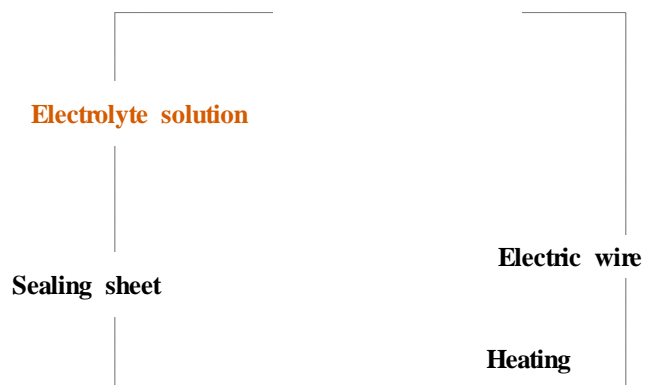
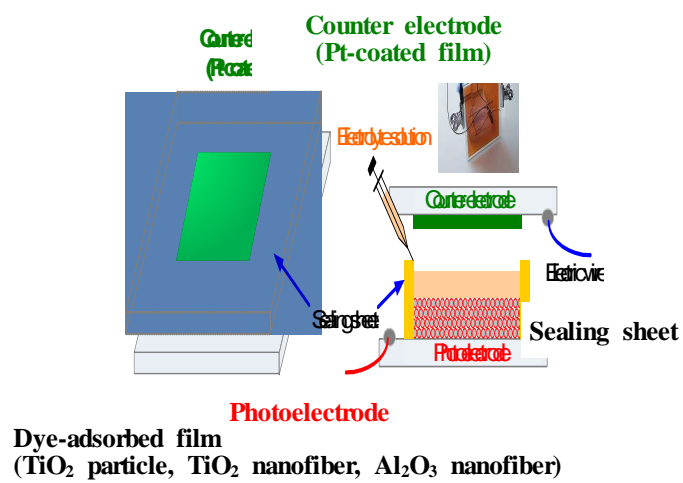


Figure 3-7 Fabrication method of dye-sensitized solar cell.

3.2.2 Measurement of DSSC

3.2.2.1 Characterization of Photoelectrode

The crystallinity of the synthesized TiO_2 was characterized by an X-ray diffractometer (**XRD**; D/MAX-1200, Rigaku Co.) using a Cu $k\alpha$ X-ray and Ni filter at 35 kV and 15 mA. The film thickness and surface morphology were measured by field-emission scanning electron microscope (FE-SEM; S-4700, Hitachi Co.). X-ray photoelectron spectroscopy (**XPS**) analysis was conducted using a photoelectron spectrometer (VG Scientific MultiLab 2000 system) equipped with a non-monochromatic Mg $k\alpha$ radiation of 1,253.6 eV. The C1s peak (285.0 eV) was used to calibrate the binding energy values. Nitrogen adsorption and desorption isotherms on TiO_2 were measured at $-196\text{ }^\circ\text{C}$ using an automatic analyzer (**BET**; ASAP 2010, Micromeritics Co.). Before the measurements, the samples were out gassed for 2 h in the degas port of the adsorption apparatus. The measurement of the adsorption-desorption isotherms required 1 day. The BET surface areas were determined from the adsorption of isotherms of nitrogen. In addition, the pore size distributions were also calculated by the Barrett, Joyner, and Halenda (BJH) method. Moreover, the fourier transform infrared spectrophotometer (**FT-IR**; DA-8, Bomem Co.) was used for the analysis of the bonding structure between dye molecules and TiO_2 surface.

3.2.2.2 Efficiency of DSSC

In this study, efficiency measurement of each photoelectrode (sol-gel TiO_2 , TiO_2 nanofiber dopant, Al_2O_3 nanofiber dopant) is followed;

The current-voltage (I - V) curves were measured using a source measure

unit under irradiation of white light from a 150 W Xenon lamp (K401 CW150 Lamp power supply; McScience Co.) (Figure 2-2). The incident light intensity and the active cell area were 100 mW/cm^2 and 0.25 cm^2 , respectively. The I - V curves were used to calculate the short-circuit current (I_{sc}), open-circuit voltage (V_{oc}), fill factor (FF), and overall conversion efficiency (η_{eff}) of DSSCs (Equation 2.1 and 2.2).

Chapter IV. Results and Discussion

4.1 Materials

4.1.1 TiO₂ Particles by Sol-gel Method

XRD pattern of the TiO₂ particle by sol-gel method (expressed as the hereafter, sol-gel TiO₂) calcined at different temperature is shown in Figure 4-1. Because the X-ray peak did not appear at the calcination temperature, 250°C, it was certain that the synthesized sol-gel TiO₂ was amorphous. As the calcination temperature went up, the peaks - (101) at 25.28°, (004) at 38.08°, (200) at 47.92°, (105) at 53.32°, and (211) at 62.66° were observed. This was the typical crystal structure of the anatase-type TiO₂.

When the deposition temperature was changed from 350°C to 600°C, the diffraction peaks became narrow. This showed that the sol-gel TiO₂ particles got bigger as the calcination temperature rose. It started to form the rutile structure at the temperature of 600°C.

The crystallite size of TiO₂ particles was measured through Scherrer's equation (Equation 4.1) and it was 34 at 350°C, 29 at 500°C, 27 at 600°C, and 32 nm at 700°C. Scherrer's equation is [110]:

$$D = \frac{K\lambda}{\beta \cos \theta} \quad (\text{Eq. 4.1})$$

where D is crystalline size of the particles (nm), K is the apparatus constant, and taken as 0.89; λ the wavelength of Cu $k\alpha$ line (0.1542 nm); θ the Bragg's angle; and β the full width at half-maximum of the diffraction peak (radian).

TiO₂ powders which were made via the sol-gel method were calcined at various temperatures and SEM photographs of the sol-gel TiO₂ particle are shown in Figure 4-2. The TiO₂ powders were calcined at 250, 350, 500, 600 and 700°C for 2 hours and they were analyzed by SEM. As a result of the analysis, the size of sol-gel TiO₂ particles got bigger as the calcination temperature rose. Especially, when the calcination temperature rose from 600°C to 700°C, the size of TiO₂ particles got bigger sharply.

The particles of anatase-type TiO₂ increased in proportion to the rise of the calcination temperature. As the anatase type changed into the rutile type, the rate of size increase of TiO₂ particles went down.

The change from anatase type to rutile type occurred at 700°C [111]. The size of anatase nanoparticles got bigger as the temperature of the reactor's center rose. And once rutile type appeared, the size of the particles got smaller [112].

The sol-gel TiO₂ particles were relatively uniform in size. According to the result of XRD analysis, all TiO₂ powders calcined at up to 500°C were anatase type.

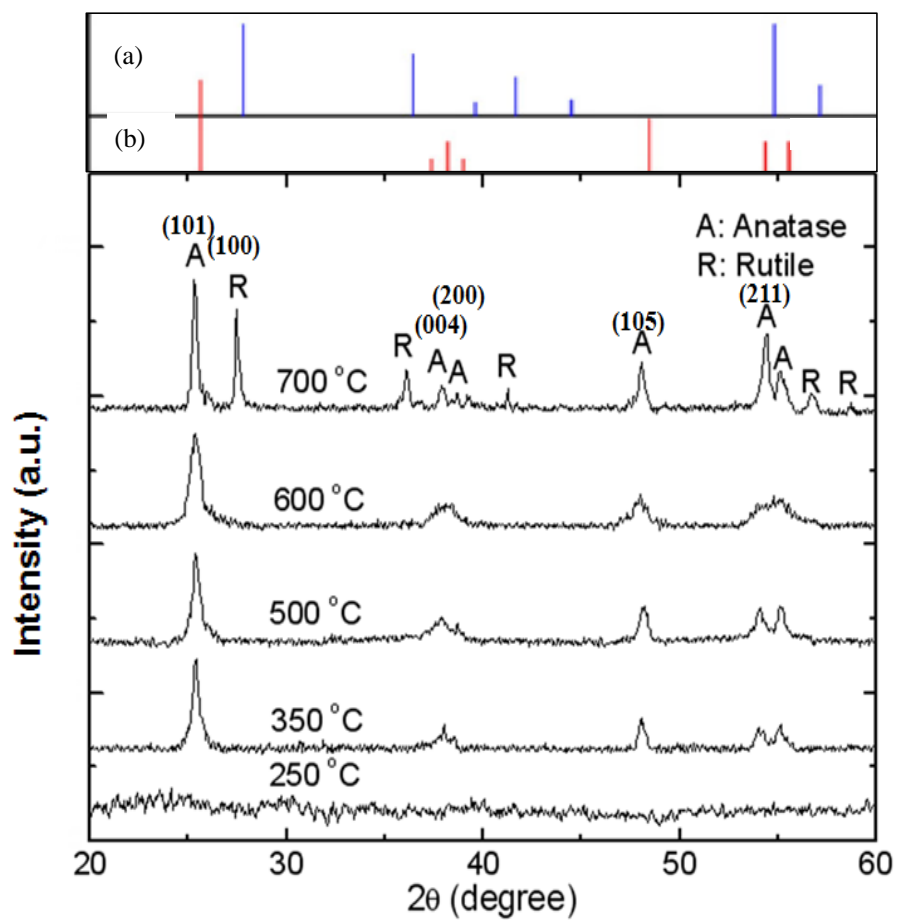


Figure 4-1 XRD patterns of sol-gel TiO_2 particles calcinated at 250, 350, 500, 600 and 700 °C. (a) Rutile, JCPDS No. 21-1276, (b) Anatase. JCPDS No. 21-1272.

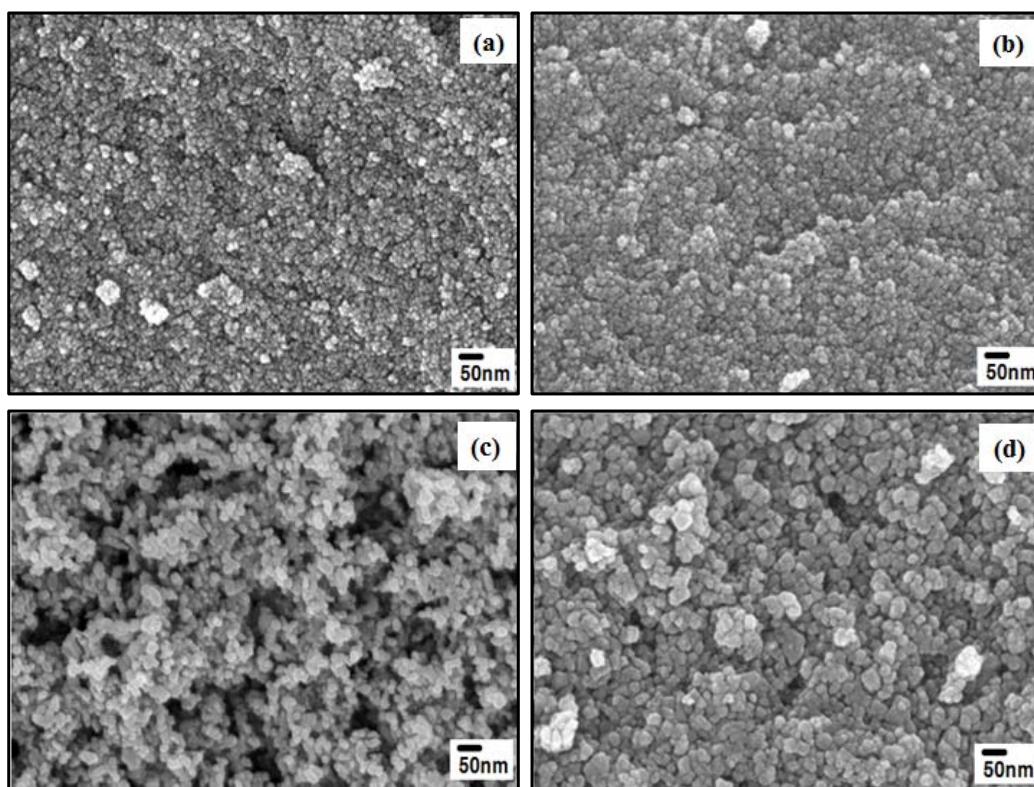


Figure 4-2 SEM photographs of sol-gel TiO₂ particle calcined at various temperatures: (a) 350°C , (b) 500°C , (c) 600°C and (d) 700°C.

Figure 4-3 shows XRD patterns of sol-gel particle and commercial TiO₂ (P25-TiO₂, Degussa Co.) with heat treatment at 450 °C for 30 min. Sol-gel TiO₂ particle showed almost single-phase anatase nanocrystallites without rutile, while P25-TiO₂ particle has the mixture of anatase and rutile phases (7:3).

XPS analysis provides important information about physicochemical changes of porous materials. Figure 4-4 is the quantitative XPS analysis of sol-gel TiO₂. XPS data of the sol-gel TiO₂ clearly show signatures of O, Ti and contains the Ti 2p and O 1s peaks of the titanium dioxide (Figure 4-4a). The Ti 2p¹ and Ti 2p³ spin-orbital splitting photoelectrons are located at binding energies of 464.4 eV and 458.7 eV, respectively (Figure 4-4b). The O 1sA peak of sol-gel TiO₂ is shown at 530.64 eV and a shoulder located toward the side of higher binding energies (Figure 4-4c). The contents of Ti and O of sol-gel TiO₂ are 27.01 % and 52.23 % corresponding to closely Ti⁴⁺ state. Generally, similar results are observed in TiO₂ porous materials^[71,113].

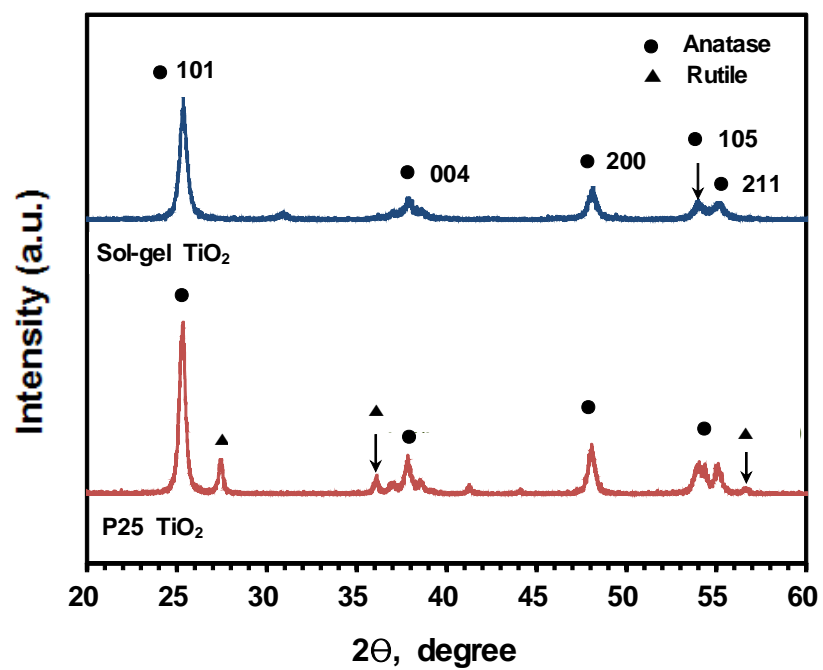


Figure 4-3 X-ray diffraction spectra of sol-gel TiO_2 and P25- TiO_2 .

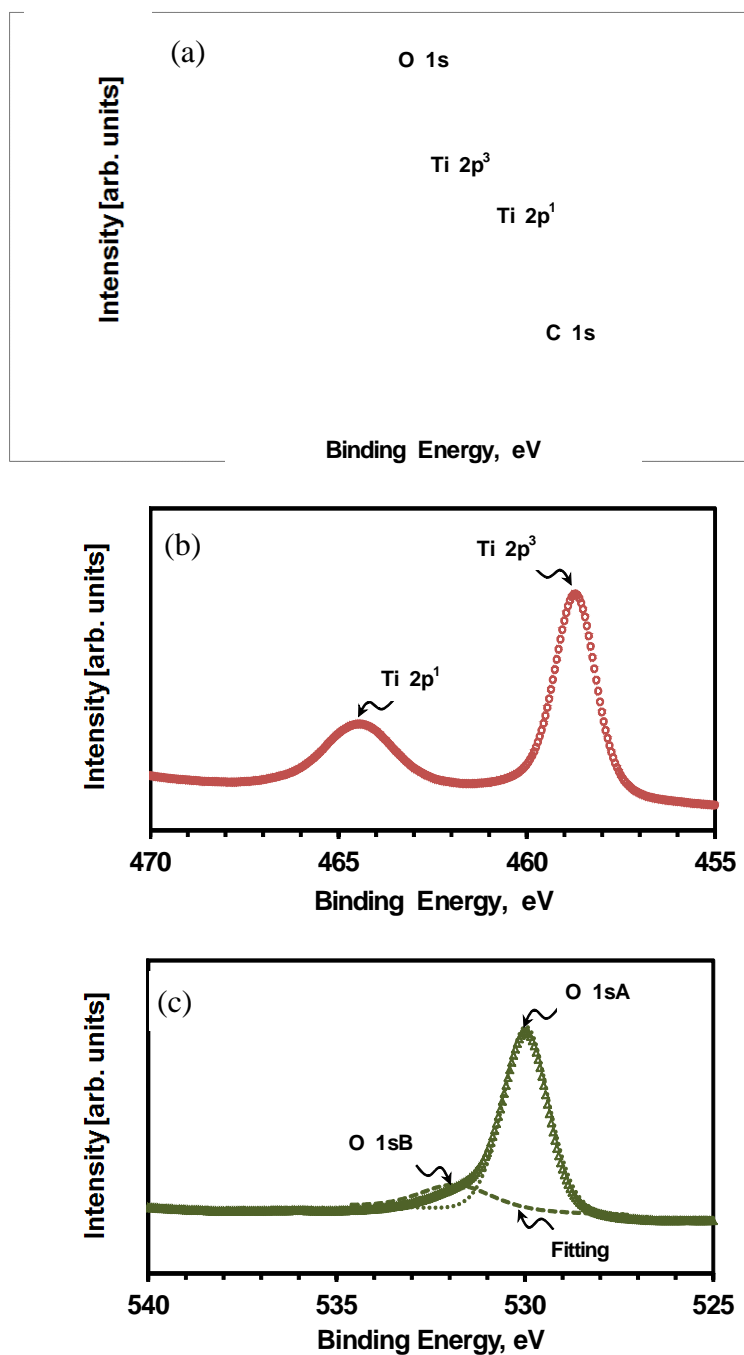


Figure 4-4 X-ray photoelectron spectra of (a) the sol-gel TiO₂ particle, (b) Ti 2p core level and (c) O 1s core level.

4.1.2 Electrospun TiO₂ Nanofibers

The synthesized TiO₂ nanofibers were characterized by FE-SEM, XRD, and BET analysis. Contrary to the commercial P-25 titania, the TiO₂ nanofibers prepared by electrospinning method in this work consist mainly of anatase from the XRD patterns.

Figure 4-5 shows the FE-SEM image of sol-gel TiO₂ particle and electrospun TiO₂ nanofiber. The TiO₂ spherical nanoparticle (ca.10~20 nm) and nanofibers (ca. diameter of 70~160 nm) are well distributed. The film thickness is about 7 μ m. The diameter of electrospun TiO₂ nanofibers was in the range of 70~160 nm.

Figure 4-6 shows the XRD patterns of the electrospun TiO₂ nanofiber calcined at temperatures 400, 450, 500, 600, 700 and 800 °C. By comparing these patterns with the TiO₂ reference patterns, one can conclude that the samples calcined at 400 and 450 °C are anatase type. But those calcined at 500, 600 and 700 °C are a mixture of anatase and rutile types. The pure rutile nanofiber was obtained by calcining at 800 °C. So a phase transformation from anatase to rutile occurs at 700-800 °C.

From the result of the nitrogen adsorption-desorption isotherm, the TiO₂ sintered at 450 °C for 30 min exhibited the International Union of Pure and Applied Chemistry (IUPAC) type-IV isotherm with a mesoporous structure (Figure 4-7). The BET surface area was about 50 m²g⁻¹ for TiO₂ nanoparticle and 17 m²g⁻¹ for TiO₂ nanofiber. The average poresize of nanoparticle and nanofiber was 67 and 3.2 nm.

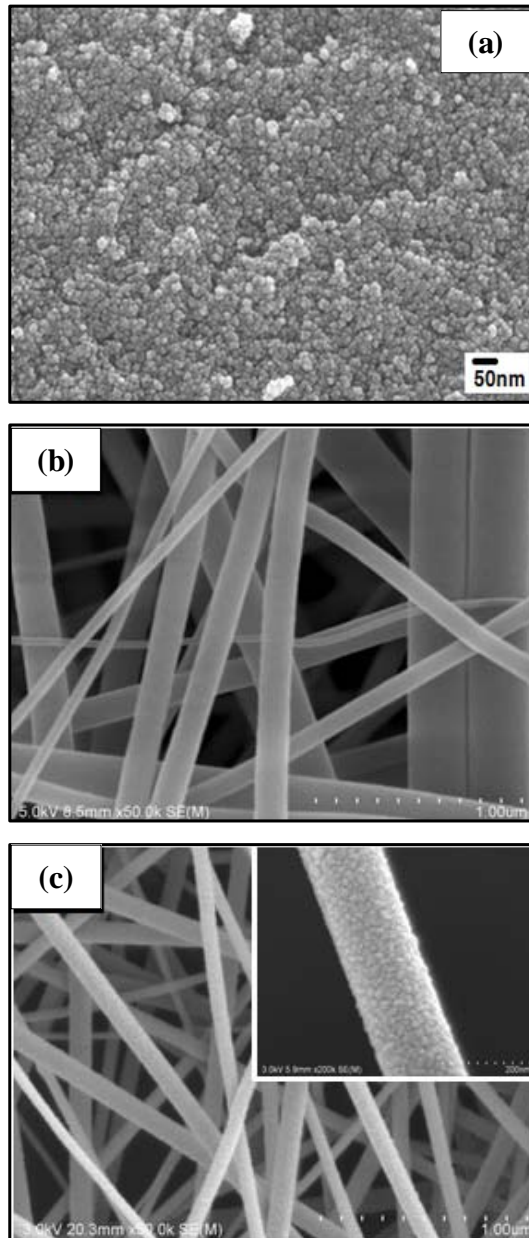


Figure 4-5 FE-SEM image of (a) sol-gel TiO_2 particle, (b) as spun TiO_2 nanofiber at room temperature and (c) calcined at 500 °C.

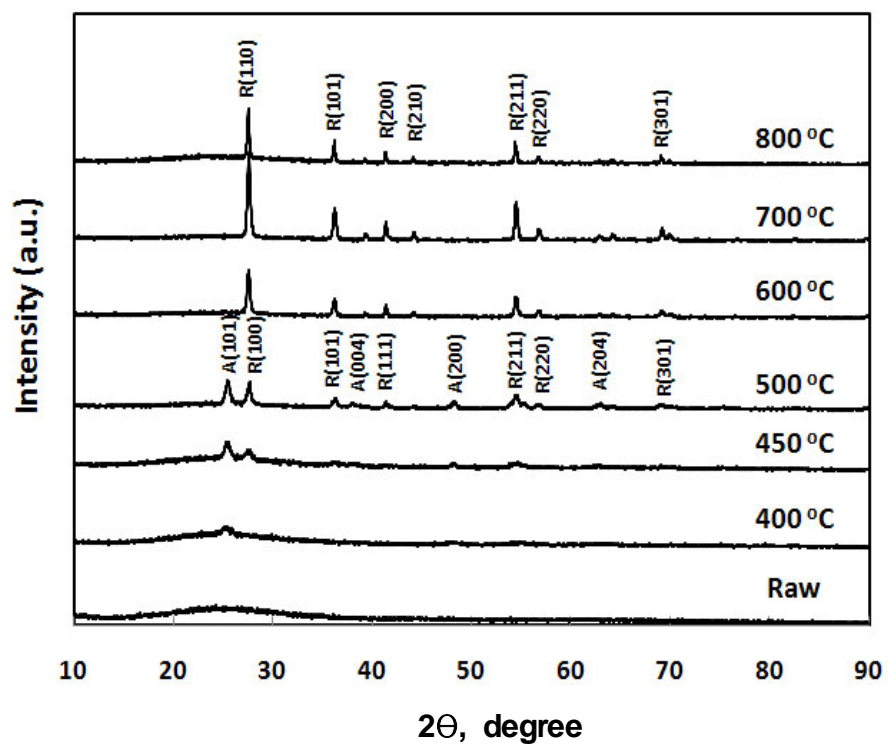


Figure 4-6 XRD patterns of electrospun TiO_2 nanofiber calcined at different temperature.

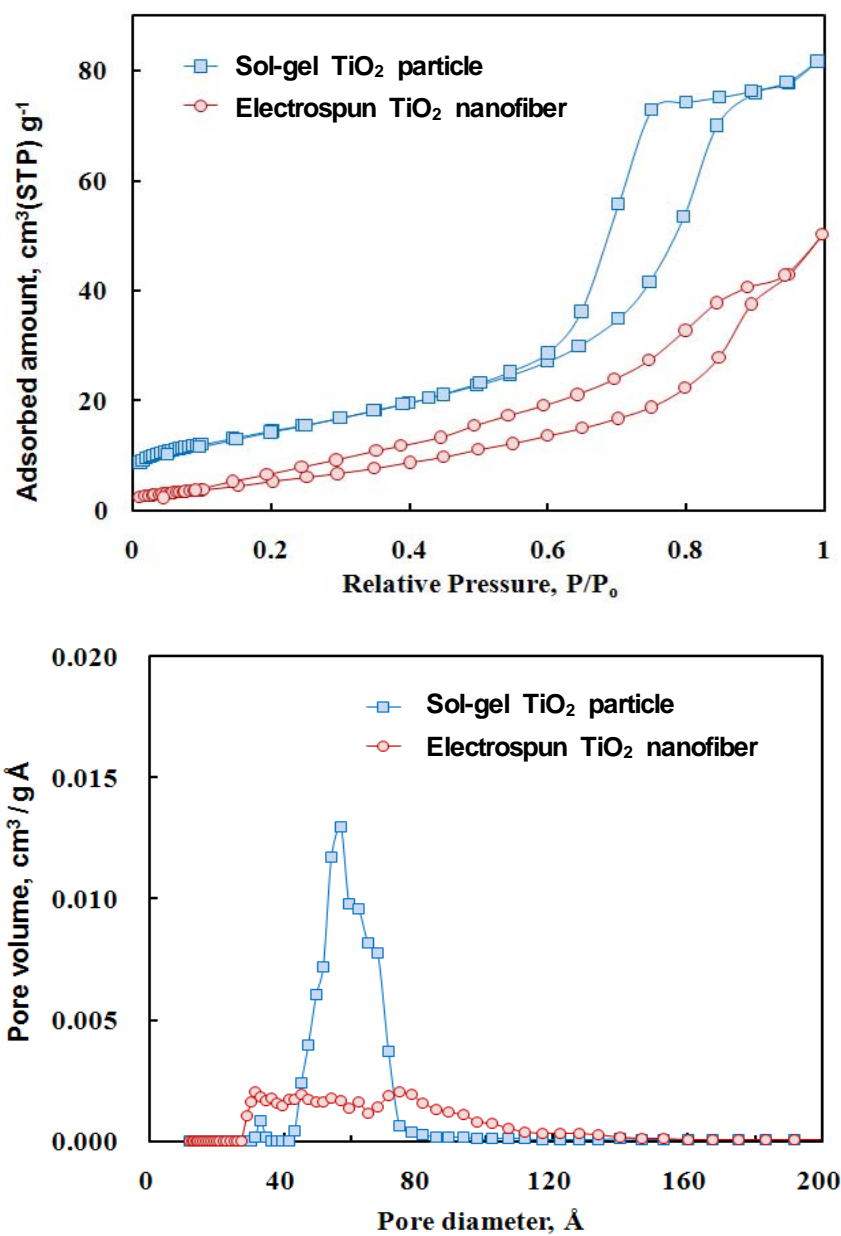


Figure 4-7 N_2 gas adsorption and desorption isotherms (a) and pore volume distributions (b) of sol-gel TiO_2 particle and TiO_2 nanofiber.

4.1.3 Electrospun Al₂O₃ Nanofibers

4.1.3.1 TGA

Figure 4-8 shows the results of the TGA of the as-spun AIP/PVP nanofibers. Endothermic and exothermic peaks were observed, with a corresponding weight loss of 17 %, in the region extending from 50 °C to 150 °C. These peaks were attributed to the vaporization of physically absorbed water and the removal of any remaining solvent from the composite fibers. In the region extending from 150 °C to 250 °C, an exothermic peak was observed that was associated with a weight loss of 26 %. This observation was in accordance with previously reported Kang et al. [114] resulted from the decomposition and burning of the PVP polymer fibers. Two exothermic peaks were observed between 250-600 °C with maxima at 324 and 429 °C, respectively. The weight loss associated with these peaks was 80% and indicated the complete combustion of the PVP polymer fibers and the organometallic compound of AIP. In contrast to a study on sol-gel process without PVP performed by Xu et al. [97], the prominent exothermic peak was observed at 429 °C and indicating the complete combustion of the PVP polymer fibers.

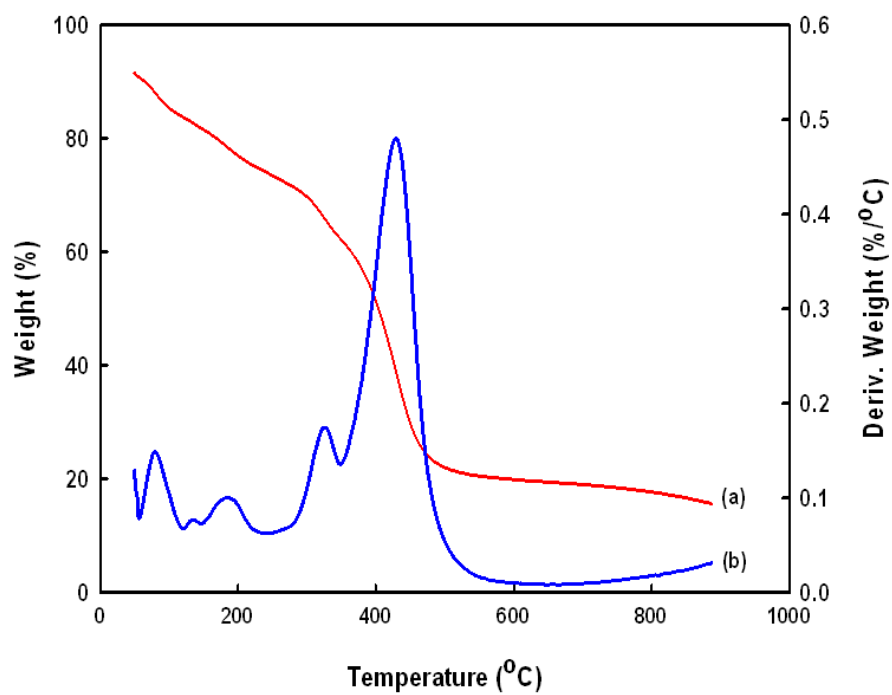


Figure 4-8 (a) The thermogravimetric curve and (b) the derivative weight loss curve of the as-spun AIP/PVP nanofibers. The heating rate was 10 °C/min.

4.1.3.2 SEM

The SEM micrographs of the composite nanofibers, which can be seen in Figure 4-8, Figure 4-10 and Figure 4-11, show that the as-spun fibers as well as those calcined at 800 °C and 1200 °C had similar morphologies. As can be readily seen, in addition to their shapes, the continuous morphology of the as-spun composite nanofibers was maintained in the calcined nanofibers as well. This was despite the decrease in the diameters of the Al₂O₃ nanofibers after the heat treatments at 800 °C and 1200 °C. Cylindrical nanofibers with diameter in the range of 276-962 nm could be successfully prepared using AIP as the precursor (Figure 4-11a). The diameter of these nanofibers decreased after calcinations at 800 °C and 1200 °C, and alumina nanofibers with diameters of 114-390 nm (Figure 4-11b) and 102-378 nm (Figure 4-11c) were obtained after the respective heat treatments. In addition, as the calcination temperature increased, the average diameter of the Al₂O₃ nanofibers decreased continuously, indicating that the organic groups in the fibers were progressively removed till almost none of them remained. However there was no further decrease in the diameter for an increase in the calcination temperature beyond 1200 °C. The Al₂O₃ nanofibers fabricated in this study were thinner and had narrower diameters distributions than those reported by Kang et al. [115].

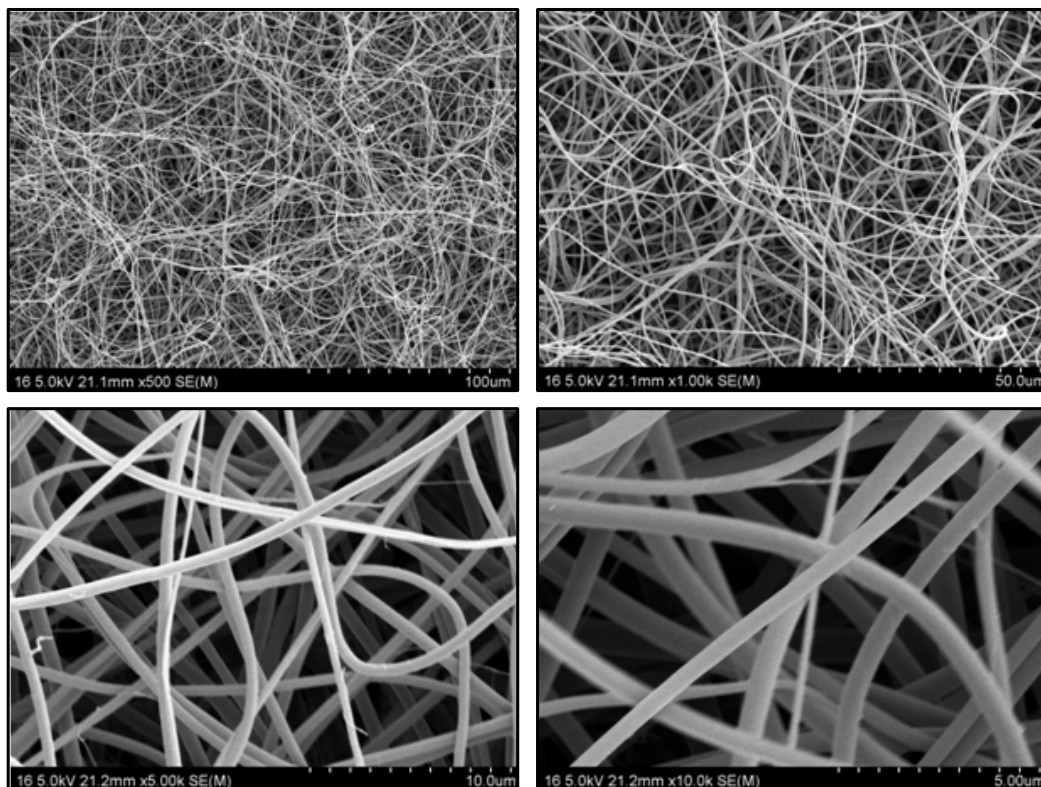


Figure 4-9 SEM images of as-spun AIP/PVP nanofibers.

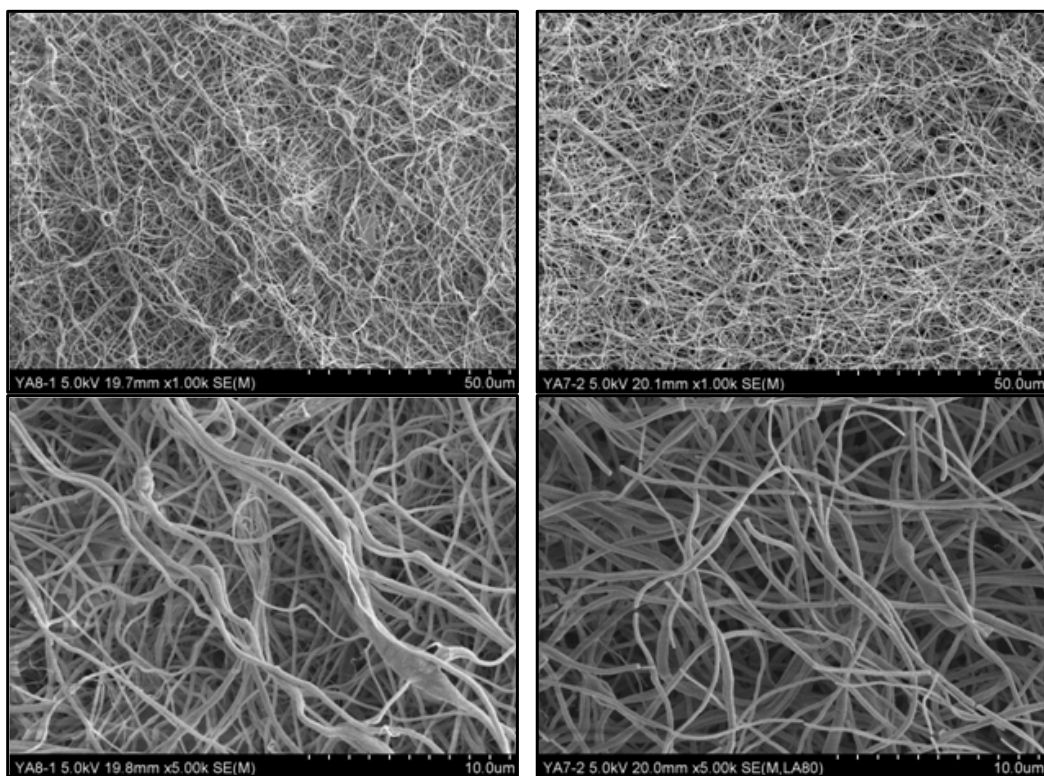


Figure 4-10 SEM images of alumina nanofibers calcinated at 800 (left) and 1200 °C (right).

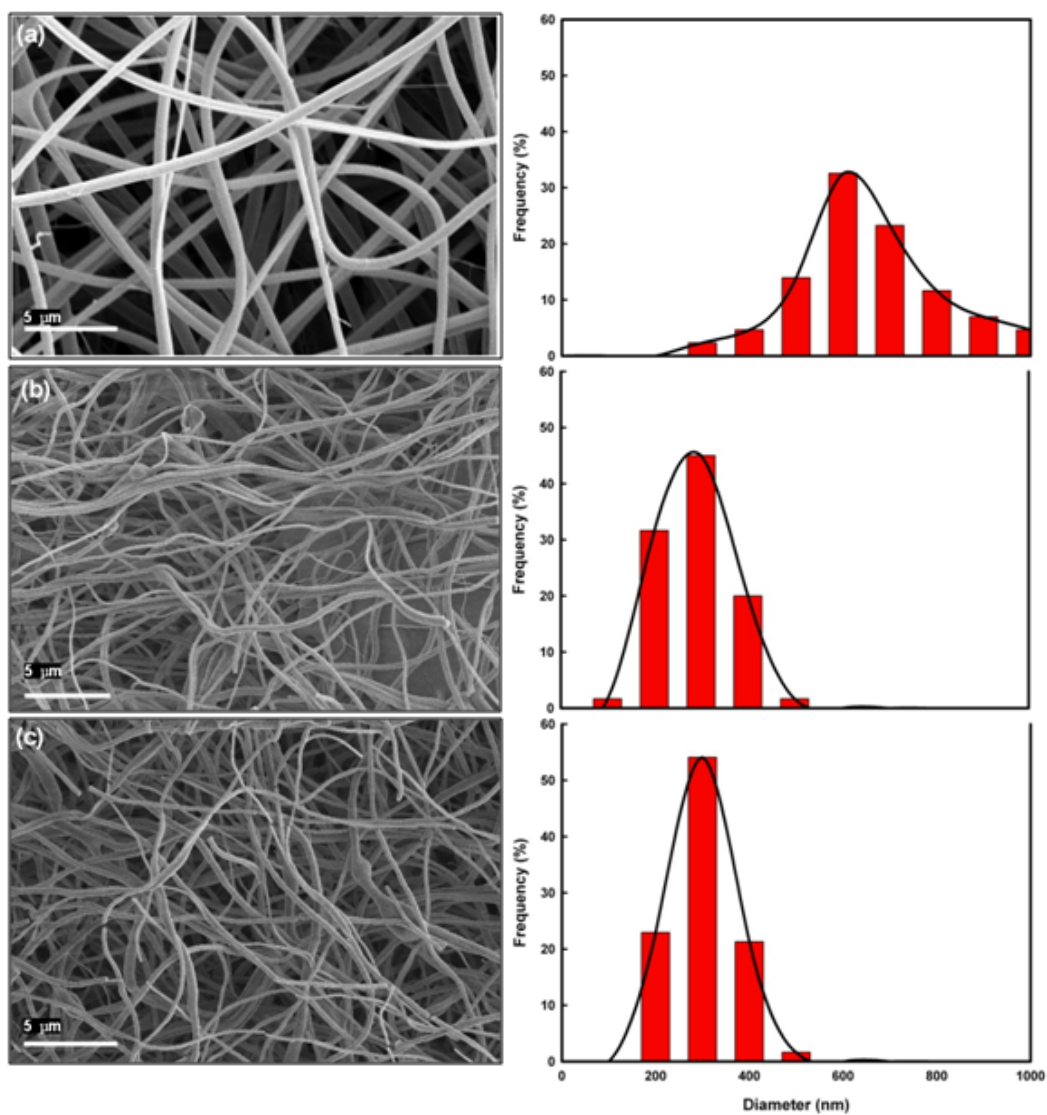


Figure 4-11 SEM images and diameter distributions of (a) the as-spun AIP/PVP nanofibers and the nanofibers calcined at (b) 800 °C and (c) 1200 °C.

4.2.2.3 XRD

Figure 4-12 shows the XRD spectra of the alumina nanofibers calcined at 700 °C, at 800 °C and at 1200 °C. The nanofibers calcined at 700 °C were found to be amorphous/microcrystalline in nature, while those calcined at 800 °C comprised the γ -alumina phase. As expected, the XRD spectrum of the sample calcined at 1200 °C indicated that α -alumina phase was formed. All the observed diffraction peaks matched well with those reported by Favaro et al. (JCPDS Card No;42-1468) [116].

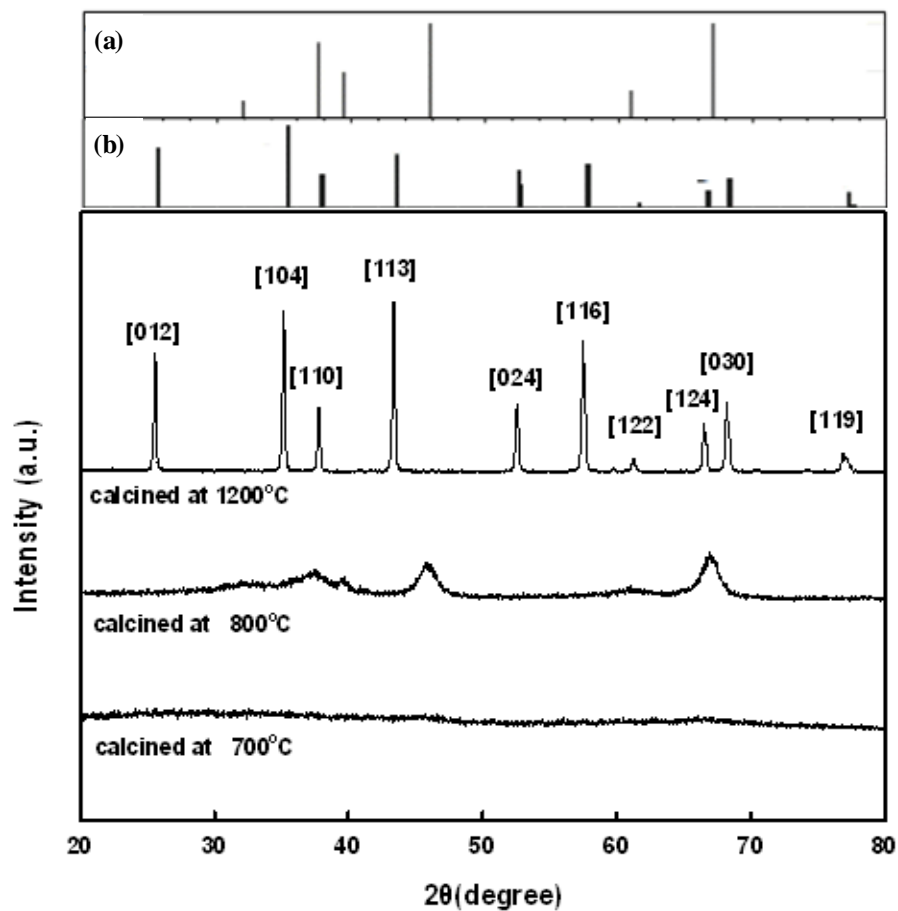


Figure 4-12 XRD spectra of the alumina nanofibers calcined at 700 °C, at 800 °C and those at 1200 °C; (a) γ -Alumina from JCPDS file 10-0425, (b) α -Alumina from JCPDS file 42-1468.

4.1.3.3 FT-IR

Figure 4-13 shows the FT-IR spectra of the (a) AIP solution, (b) AIP/PVP solution, (c) as-spun composite fibers, (d) alumina fibers obtained after calcination of the composite fibers at 800 °C and (e) those obtained after calcination at 1200 °C. Figure 4-13a and 4-13b show the characteristic peaks at around 3400, 2900, 1600, 1000, 881 and 600 cm^{-1} , respectively, which is corresponding to the stretching and bending vibrations of AIP/PVP. The results are in agreement with the experimental and theoretical spectra investigated by Mahapatra [117], Xu [97] and Favaro [116] in the range of the OH- stretching bands of gibbsite. Figure 4-13c shows the FT-IR spectrum of AIP/PVP as spun composite fibers after drying at 800 °C. The three characteristic peaks in the region of 400-1000 cm^{-1} is observed, which is due to removal of ethanol and adsorbed water in air. Figure 4-13d and 4-13e show the appearance of new peaks in the range of 440-860 cm^{-1} . The results are may be attributed to the presence of alumina and is also supported by XRD results [116]. The measured IR spectra corresponding to temperatures show a spectrum that was observed in other works [116] with three main structures visible between 400 and 650 cm^{-1} . When the fibers was calcined at 800 °C and 1200 °C, the characteristic peaks of PVP and O-H stretching band disappeared because of removal of polymer and decomposition of AIP precursors at calcination temperature [1187].

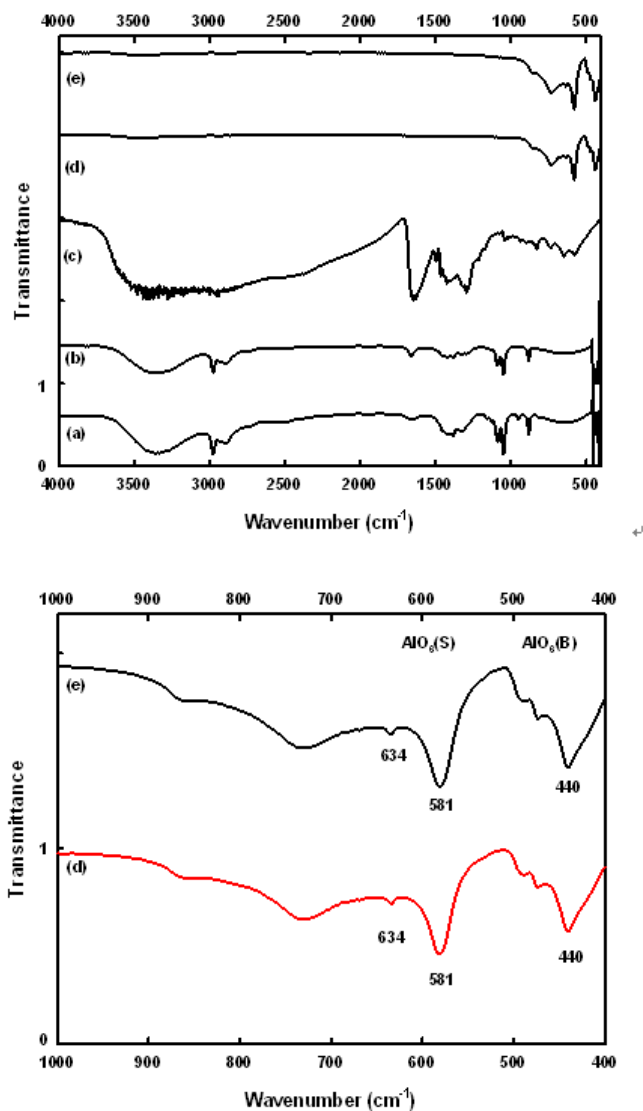


Figure 4-13 FT-IR spectra of (a) AIP solution, (b) AIP/PVP solution, (c) as-spun AIP/PVP composite nanofibers, (d) alumina nanofibers calcined at 800 $^{\circ}\text{C}$, (e) and those calcined at 1200 $^{\circ}\text{C}$. (B:Al-O bending, S:Al-O stretching).

4.1.3.4 Effects of Humidity on Al₂O₃-based PVP Electrospun Fibers

Humidity effects on Al₂O₃ nanofibers were studied by electrospinning method. Table 4-1 shows electrospinning condition. The humidities of inside chamber during electrospinning were typically controlled and maintained between 30 and 80 % RH. And the general effects of fiber morphology was also observed by SEM.

Table 4-1 Condition of electrospinning in this study

Parameter	Condition
Syringe	10 mL (SGE LL type) with metallic needle
Collector	Rotating 200 rpm
voltage	15 kV, 20 kV
Feeding rate	3.0 mL/h
Distance (between tip and collector)	15 cm
Relative humidity	30-80 % at room temperature

Figure 4-14 shows SEM images for effects of humidity on as-spun composite nanofiber. Lower humidity (less than 35% RH) displayed fiber-like, however it raised fiber-fiber bonding (Figure 4-14a). Humidity between 40 and 55% RH was found to be formed clean fibrous structure (Figure 4-14b, 4-14c and 4-14d). Higher humidity (70 % RH or more) was induced excessive plasticization of the as-spun Al₂O₃/PVP nanofiber (Figure 4-14e).

Figure 4-15 shows SEM images of as-spun composite nanofiber at less than 35 % RH condition according to voltage power supply (15 and 20 kV). When the voltage is changed to 15 kV from 20 kV, fiber-fiber bonding phenomenon has been slightly improved (Figure 4-15b).

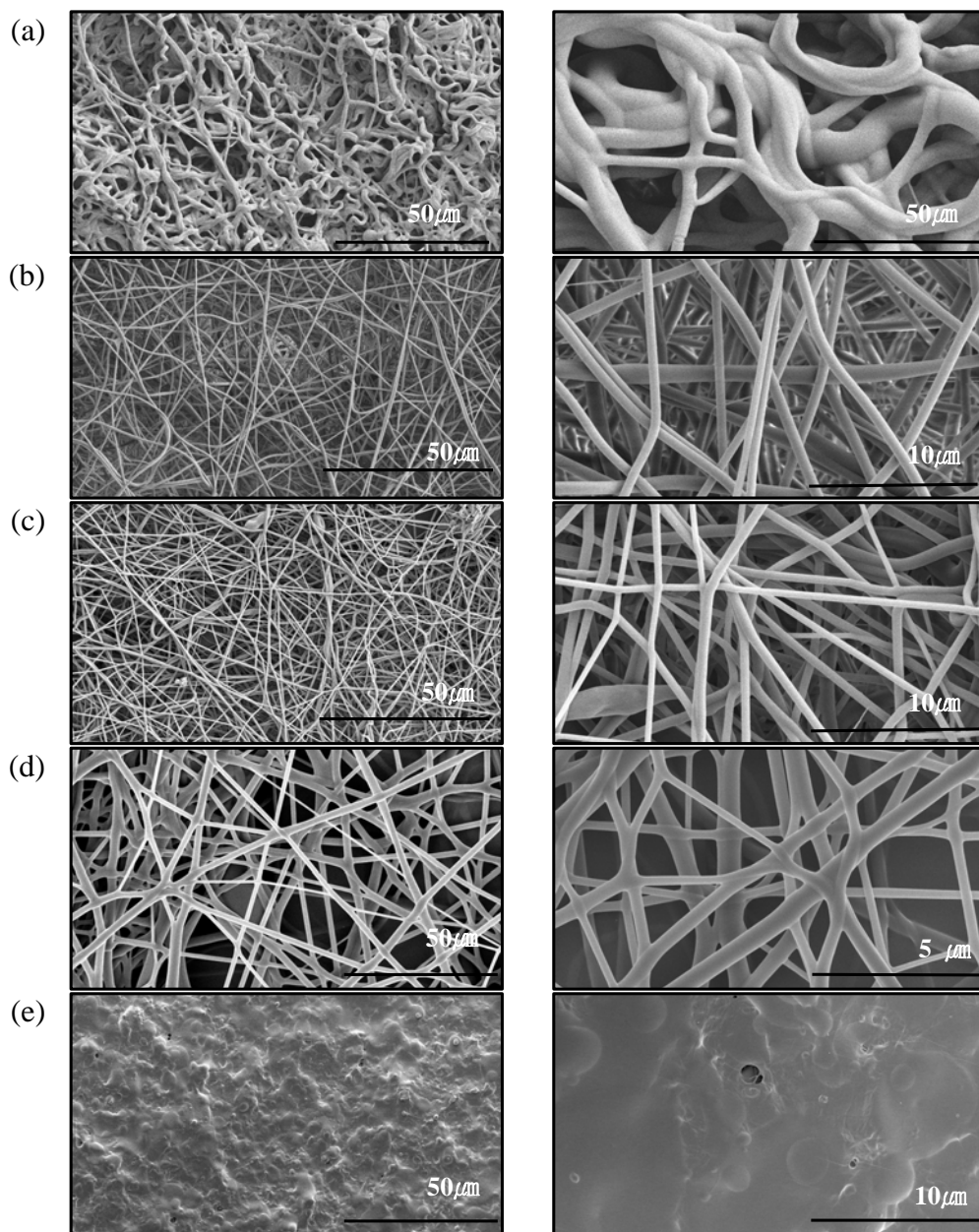


Figure 4-14 SEM image according to relative humidity of as-spun $\text{Al}_2\text{O}_3/\text{PVP}$ nanofiber; (a) RH > 35 %, (b) RH 40-45 % (c) RH 45-50 % (d) RH 50-55 % and (e) RH 70 < %. Electrospinning condition (1.5 mL/h, 20 kV, 15 cm).

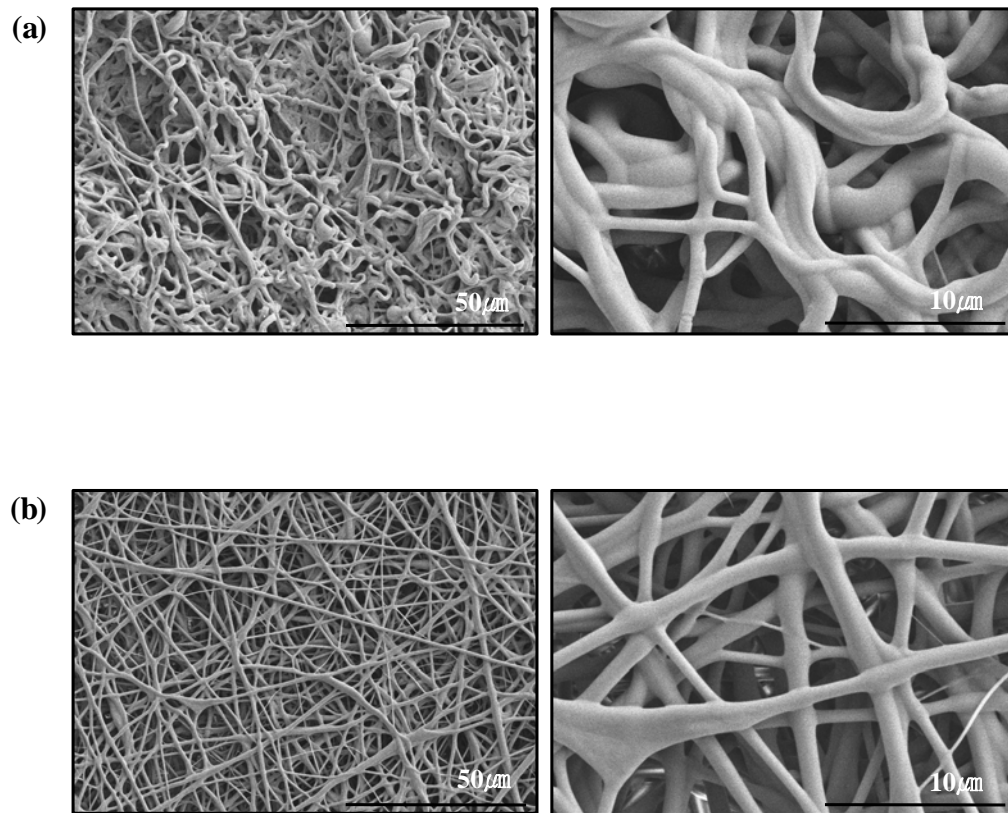


Figure 4-15 SEM image of as-spun Al_2O_3 nanofibers at different power supply (a) 15 kV and (b) 20 kV (Relative Humidity <35 %).

4.2 Photoelectricity for DSSC Performance

4.2.1 TiO₂ Particle Photoelectrode

To characterize the nanocrystalline sol-gel TiO₂ film properties, BET, FE-SEM, and FT-IR measurements were performed. **Figure 4-16** exhibits the FE-SEM images of surface morphology and the cross-section of TiO₂ thin films coated on FTO glass.

TiO₂ film has a porous structure in which the TiO₂ spherical nanoparticles are all bonded together through a sintering process. The spherical nanoparticles of P25-TiO₂ film (Figure 4-16a) and sol-gel TiO₂ film (Figure 4-16b) are well distributed and maintain their original size and shape. The pattern reveals the TiO₂ particles to be composed of a three-dimensional network of interconnected particles. We also found that the particle size of sol-gel TiO₂ was smaller than that of P25-TiO₂. These results are consistent with those estimated from XRD data.

From the line width of XRD peak (anatase, 101) of the TiO₂ samples, we have also roughly estimated the particle sizes of TiO₂ using the Scherrer's equation (Equation 4.1). From the Equation 4.1, their crystalline nanoparticle sizes are about 22 nm for P25-TiO₂ and 14 nm for sol-gel TiO₂.

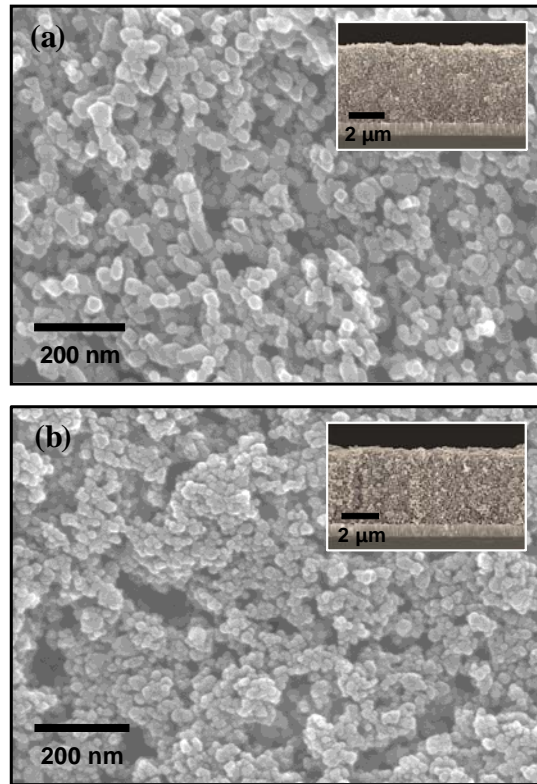


Figure 4-16 FE-SEM images of (a) P25-TiO₂ and (b) sol-gel TiO₂ film.

Table 4-2 Surface properties of TiO₂ film

Properties	Unit	P25-TiO ₂ film	Sol-gel TiO ₂ film
Root mean square roughness (R_q)	nm	25.1	28.8
Mean roughness (R_a)	nm	20.3	22.9
Adsorption amount of N719	mmol $\times 10^{-6}/\text{cm}^2$	4.982	5.874

Commonly, if the TiO₂ thin film has a higher surface roughness, the amount of N719 dye adsorbed is increased [119]. It has been known that the anatase TiO₂-based solar cells exhibit better photovoltaic characteristics compared to the rutile TiO₂-based solar cells because of higher surface area (i.e., higher amount of dye adsorption) [110]. These results corresponds to adsorption amount of N719 dye on TiO₂ film in Table 4-2.

The surface area determined by nitrogen adsorption/desorption isotherm data of sol-gel TiO₂ was found to be 63 m²/g (Figure 4-17a), and the average pore size calculated by BJH method was 83 Å (Figure 4-17b). From the results of the nitrogen adsorption/ desorption isotherm, the sol-gel TiO₂ exhibited the International Union of Pure and Applied Chemistry (IUPAC) type-IV isotherm with a mesoporous structure [120,121,122]. A slight increase of surface area of sol-gel TiO₂ fabricated in this work compared to P25-TiO₂ is attributed to the development of mesopores.

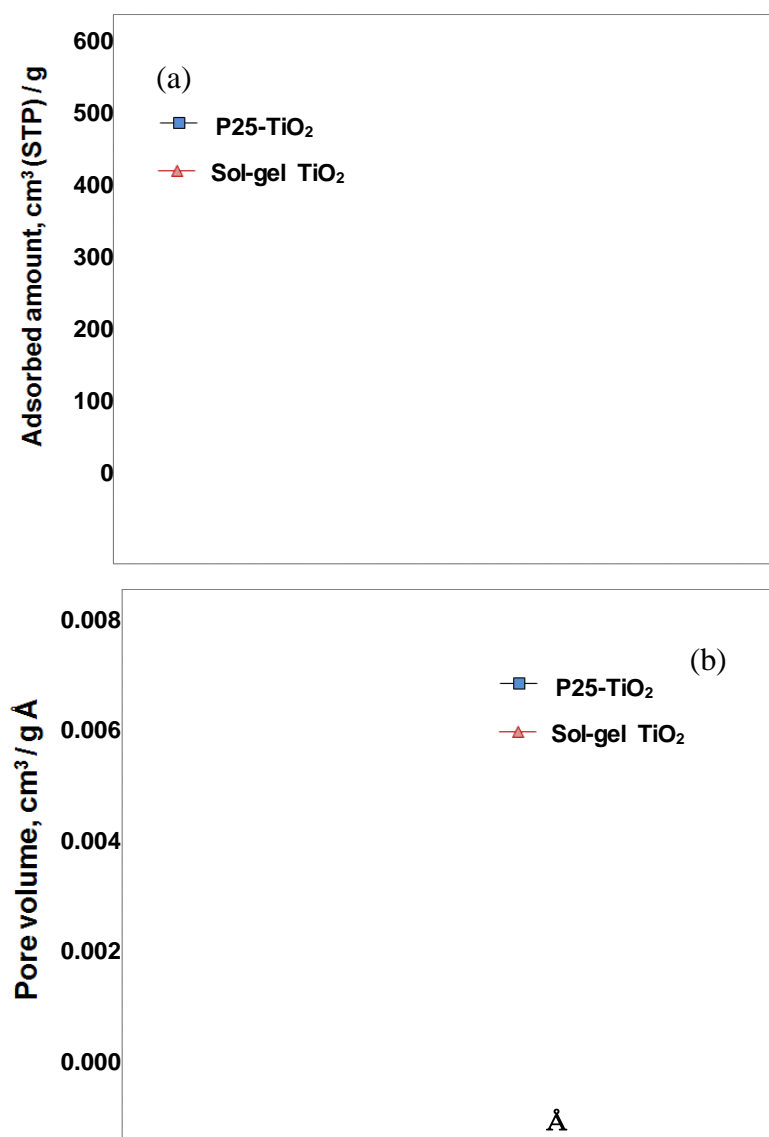


Figure 4-17 N₂ gas adsorption and desorption isotherms (a) and pore size distributions (b) of sol-gel TiO₂ and P25-TiO₂ films.

Interfacial binding between the dye molecules (N719) and the surface of TiO_2 was investigated by FT-IR spectra of the dye-anchored TiO_2 films. In general, the efficiency of the charge injection process is highly dependent on bonding structure of the dye molecules adsorbed on the TiO_2 film. In addition, the electron transfer in DSSC is strongly influenced by electrostatic and chemical interactions between TiO_2 surface and the adsorbed dye molecules [123].

Figure 4-18 shows the FT-IR spectra of N719 dye adsorbed on TiO_2 films (P25- TiO_2 , sol-gel TiO_2) compared to the signals of the dye powder. Absorption at $2,105\text{ cm}^{-1}$ of N719 dye is attributed to the SCN stretch model of N-bonded SCN ligand [124,125]. The FT-IR spectra were observed at $1,370\text{ cm}^{-1}$, $1,610\text{ cm}^{-1}$, and $1,720\text{ cm}^{-1}$ when the dye molecules were adsorbed on P25- TiO_2 and sol-gel TiO_2 films. The FT-IR spectra located at $1,370\text{ cm}^{-1}$ and $1,610\text{ cm}^{-1}$ is consistent with the bidentate coordination. Compared to the dye-anchored P25- TiO_2 films, the dye-anchored sol-gel TiO_2 films have strong absorptions at $1,720\text{ cm}^{-1}$, indicating the C=O stretch mode of the protonated carboxylic acid (i.e., ester-like linkage). Similar results were reported that the coordination of N719 dye on TiO_2 films occurs mainly by the contribution of unidentate (i.e., ester-like linkage) and partially by bidentate linkage [123,124,125].

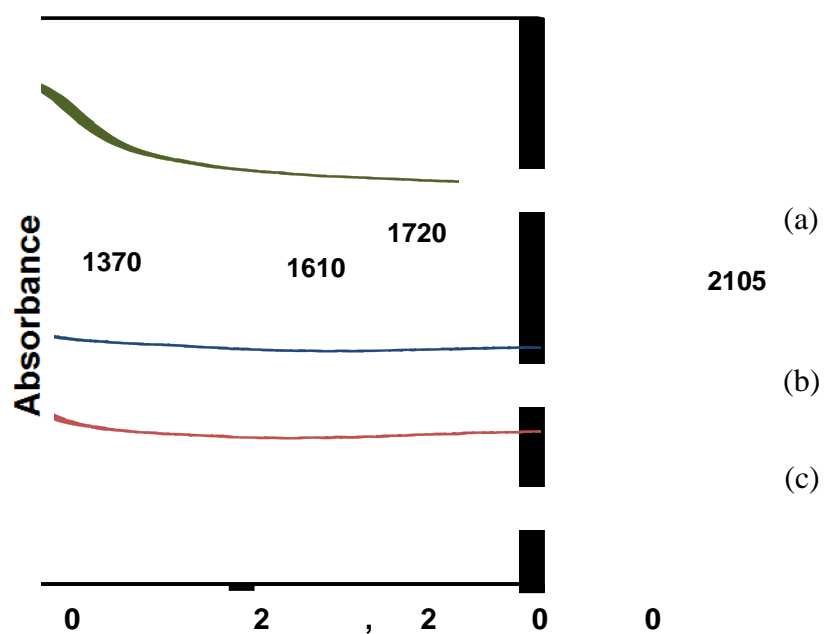


Figure 4-18 FT-IR spectra; N719 dye powder (a), N719 dye adsorbed on P25-TiO₂ film (b) and sol-gel TiO₂ film (c).

Figure 4-19 shows the photocurrent-voltage curves of P25-TiO₂ and synthesized sol-gel TiO₂. The fill factor (FF) and overall energy efficiency (η_{eff}) were determined by the Equations 2.1 and 2.2 which was described in detail elsewhere [48,81]. Where I_{sc} is the short-circuit current density (mA/cm²), V_{oc} is the open-circuit voltage (V), P_{in} is the incident light power, and I_{max} (mA/cm²) and V_{max} (V) are the current density and voltage in the I - V curve at the point of maximum power output. The determined I - V curves are summarized in Table 4-3.

A dye-sensitized solar cell with sol-gel TiO₂ electrode fabricated in this work gave an open-circuit voltage of 0.55 V, short-circuits current density of 15.57 mA/cm² for an incident light intensity of 100 mW/cm² and the conversion efficiency of over 4.88 %. Also, it showed that photo-energy conversion efficiency of DSSC with sol-gel TiO₂ electrode was increased compared with the P25-TiO₂ electrode.

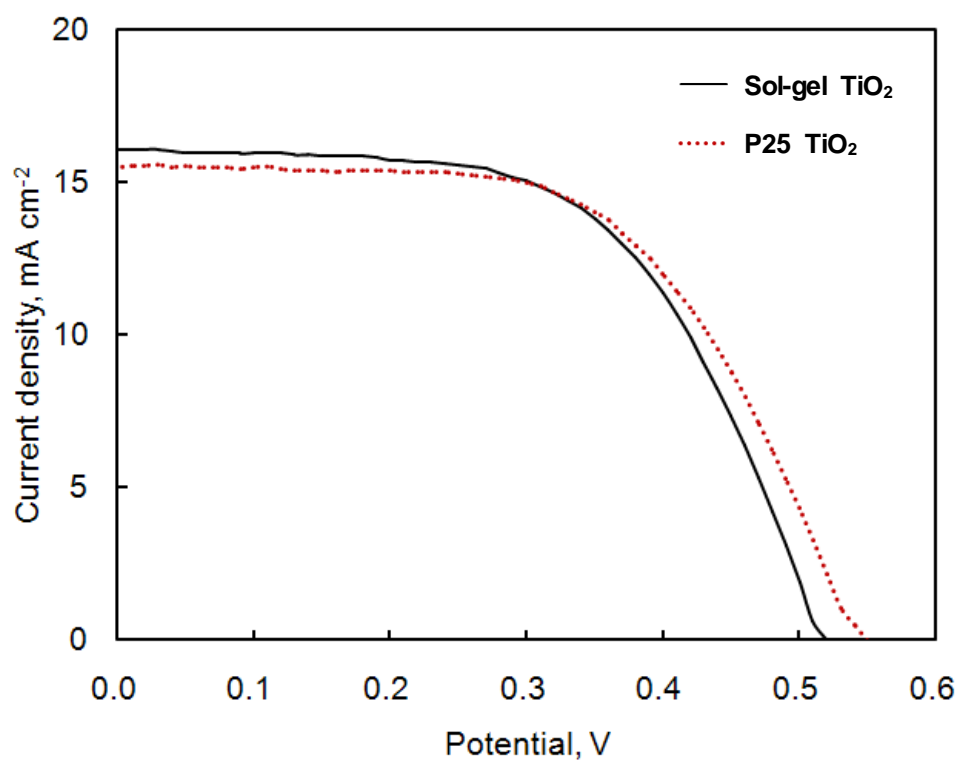


Figure 4-19 Photocurrent-voltage (I - V) curves of sol-gel TiO₂ and P25-TiO₂ films.

Table 4-3 Photovoltaic performance of DSSC

	V_{oc} , V	I_{sc} , mA/cm ²	FF	η_{eff} , %
P25-TiO ₂ film	0.52	16.08	0.52	4.26
Sol-gel TiO ₂ film	0.55	15.57	0.57	4.88

Characterization of DSSC with Sol-gel TiO₂ Electrode on Adsorption Time

In this study is experimental for characterization of DSSC with sol-gel TiO₂ electrode on adsorption time and adsorption amount.

Before making the cell, the working electrodes were immersed in a 0.5 mM of N719 dye for different adsorption time (0.25, 0.5, 1.0, 5.5, and 24 h) to control the adsorption amount. The effect of adsorption quantity on the photovoltaic performance of DSSC analyzed. The determined the short-circuit current (I_{sc}), open-circuit voltage (V_{oc}), fill factor (FF), and overall conversion efficiency (η_{eff}) of DSSCs are summarized in Tables 4-3.

And figure 4-20 shows efficiency and adsorption amount according to adsorption time of N719 dye. As shown in the figure 4-20, it was noted that the order of the photocurrent densities and conversion efficiency increased with the adsorption amount and adsorption time, until adsorption time 5.5 h. The result is showed that high adsorption capacity of sol-gel TiO₂ with the low charge transfer resistance may give rise to the superior I_{sc} of DSSCs because of the monolayer adsorption [123].

However, after adsorption time 5.5 h, there was little change in amount of adsorption and the photocurrent density and conversion efficiency of sol-gel TiO₂ decreases with increasing immersion time. This result may explain how the agglomeration of dyes molecules adsorbed on sol-gel TiO₂ surfaces affected negatively on the charge transfer resistance [67,126]. To avoid this agglomeration of dye molecules, the dye adsorption should be conducted under a supercritical condition. It can be concluded from this work that the conversion efficiency of the DSSC was dependent on the

adsorption properties of N719 dye on TiO₂ films.

Table 4-4 Characteristics values of dye-sensitized solar cells according to adsorption time

Adsorption time, h	Adsorption amount, mmol $\times 10^{-6}$ /cm ²	V_{oc} , V	I_{sc} , mA/cm ²	Fill factor, <i>FF</i>	η_{eff} , %
0.25	0.25	0.58	1.4	59	0.5
0.5	1.05	0.62	3.3	47	1.0
1.0	3.67	0.63	6.3	42	1.7
5.5	5.29	0.62	8.5	45	2.4
26.0	5.35	0.66	7.3	45	2.2

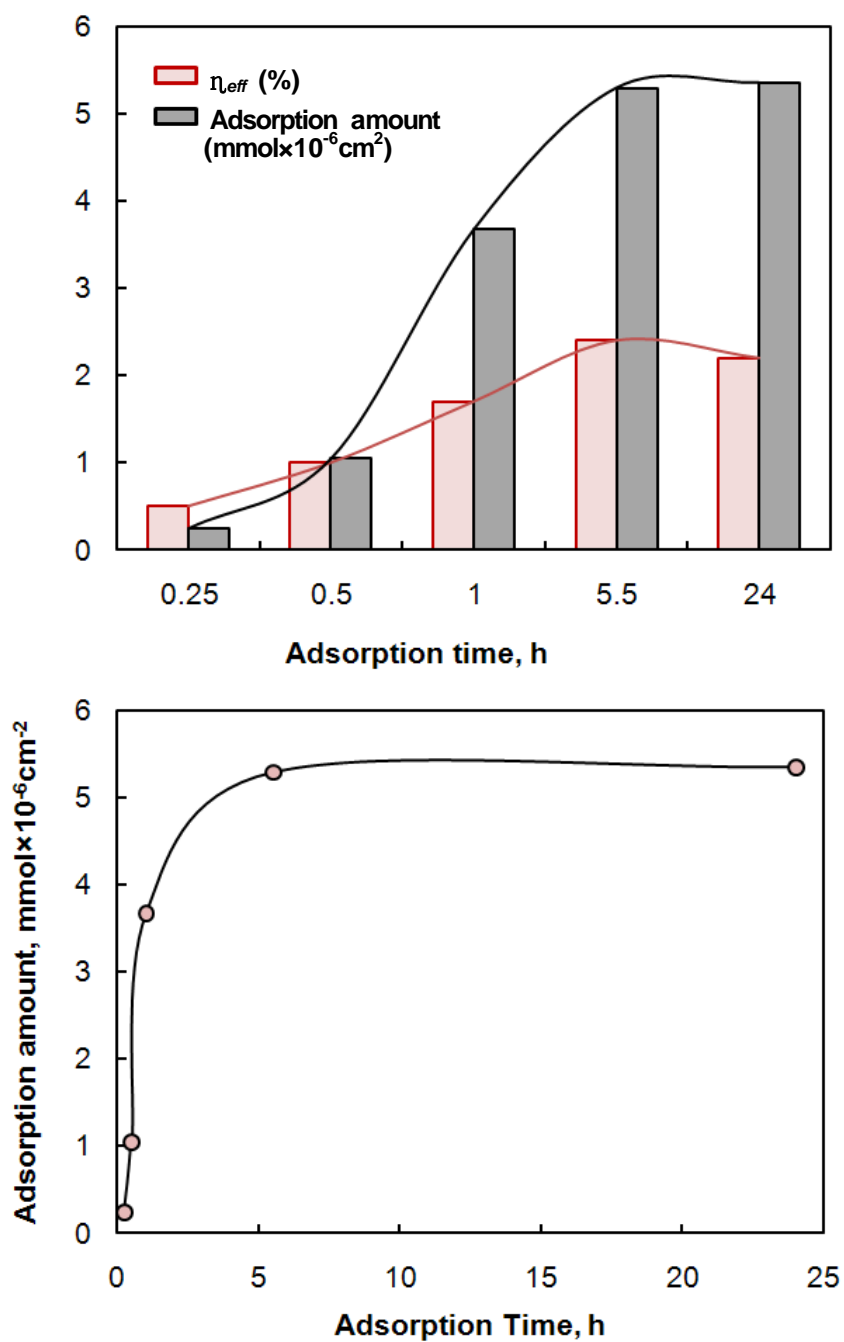


Figure 4-20 Efficiency and adsorption amount according to adsorption time of N719 dye.

4.2.2 TiO₂ Nanofiber Doped TiO₂ Nanoparticle Electrode

Photovoltaic efficiency of the photoelectrode film with different TiO₂ nanofiber content performance was carried out. To evaluate the photovoltaic performance of nanoporous TiO₂ thinfilm, the current–voltage curves were obtained. The photocurrent-voltage (*I*-*V*) curves were measured using a source measure unit under irradiation of white light from a 1,000 W Xenon lamp (Thermo Oriel Instruments). The incident light intensity and the active cell area were 100 mW/cm² and 0.25 cm², respectively. The *I*-*V* curves were used to calculate the short-circuit current(*I*_{sc}), open-circuit voltage(*V*_{oc}), fillfactor(*FF*), and overall conversion efficiency (η_{eff}) of DSSC. As shown in Fig.6, it was observed that the over all conversion efficiency(η_{eff}) is in the following order: NF (1.5 wt%: 5.87 %) > NF (0.5 wt%: 5.43 %) > NF (0.0 wt%: 5.00 %). This trend is identical to that of the N719 adsorption on nanoparticle and nanofibers of TiO₂. Therefore, It is reasonable to conclude that the overall photovoltaic performance was substantially dependent on the adsorption amount of N719 (Figure 4-21 and Table 4-5) because of the high packing density of TiO₂ electrode by employing the TiO₂ nanofiber additives.

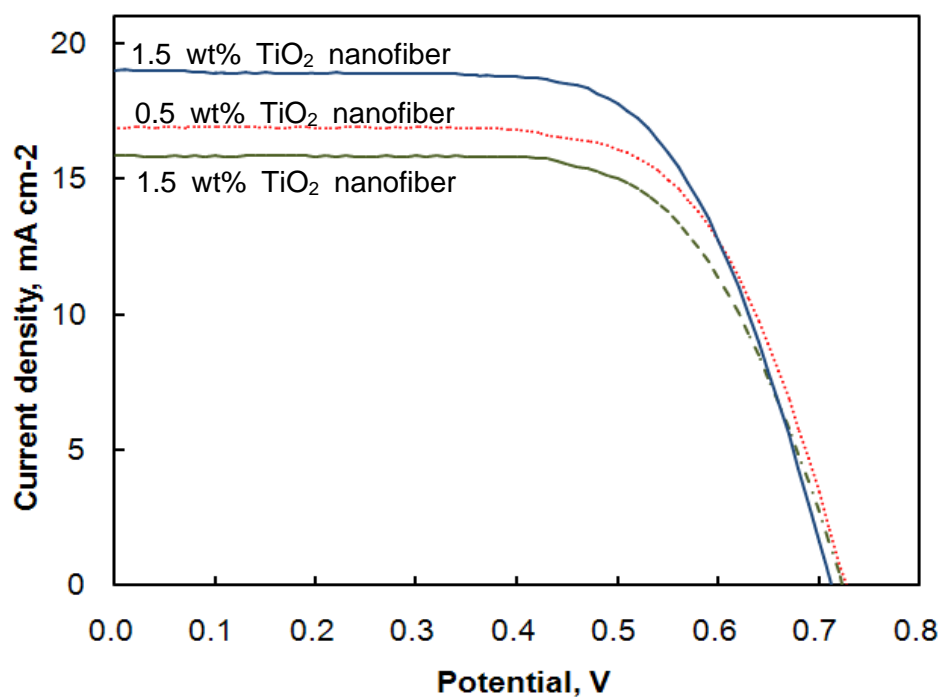


Figure 4-21 Photocurrent-voltage(I-V) of DSSCs depending on the contents of TiO₂ nanofiber dopant in TiO₂ electrode.

Table 4-5 Photovoltaic performance of DSSC with TiO₂ nanofiber dopant

TiO ₂ nanofiber(NF) content	V_{oc} , V	I_{sc} , mA/cm ²	FF	η_{eff} , %
Without NF	0.73	15.86	0.43	5.00
0.5 % NF	0.73	16.93	0.43	5.26
1.5 % NF	0.72	19.01	0.42	5.77

4.2.3 Al₂O₃ Nanofiber Doped TiO₂ Nanopatical Electrode

Photovoltaic efficiency of the photoelectrode film with different Al₂O₃ nanofiber content performance was carried out.

Figure 4-22 shows SEM image and EDS analysis of Al₂O₃ nanofiber doped photoelectrode. As shown in the SEM image, there is no difference between the Al₂O₃ nanofiber and TiO₂ particles. This is considered that both have due to a similar size of single-crystal spherical particles. Electrosun Al₂O₃ nanofiber doped photoelectrode, which particles are mixed with each other, is played a decisive role in the delivery of the generated photoelectron and the adsorption of the dye and the electrode [127]. EDS data acquired on the photoelectrod film are displayed in light of Figure 4-22. The spectra reveal signatures of titanium and aluminum.

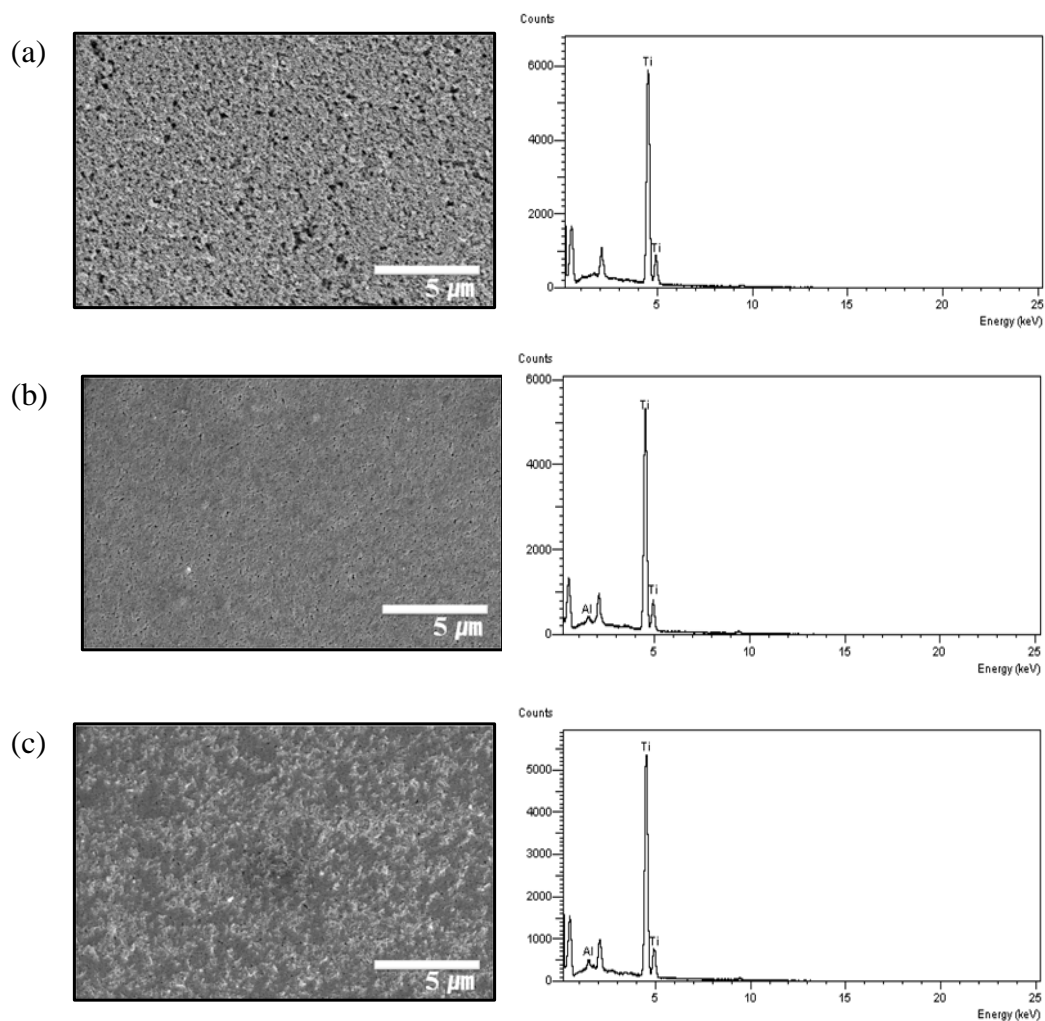


Figure 4-22 SEM image (left side) and EDS analysis (right side) of Al_2O_3 nanofiber doped TiO_2 films; (a) without Al_2O_3 nanofiber, (b) 0.5 % Al_2O_3 nanofiber (c) 1.0 % Al_2O_3 nanofiber.

Information about the surface elemental composition of the electrode is obtained using XPS. Since many relevant processes such as adsorption or catalysis occur on surfaces, the presence of even trace amounts of impurities may have unwanted effects in the application of these material and, in that regard, XPS is a very powerful analytical method for our purposes [128, 129]. Survey scans of composite $\text{Al}_2\text{O}_3/\text{TiO}_2$ powder calcined at 700 °C are presented in Figure 4-23. XPS data clearly show signatures of O, Ti, and Al. A carbon signal is almost always seen in XPS as previously reported for calcined electrospun Al_2O_3 [129], TiO_2 [130], and this result was similar to experiments of the EDS.

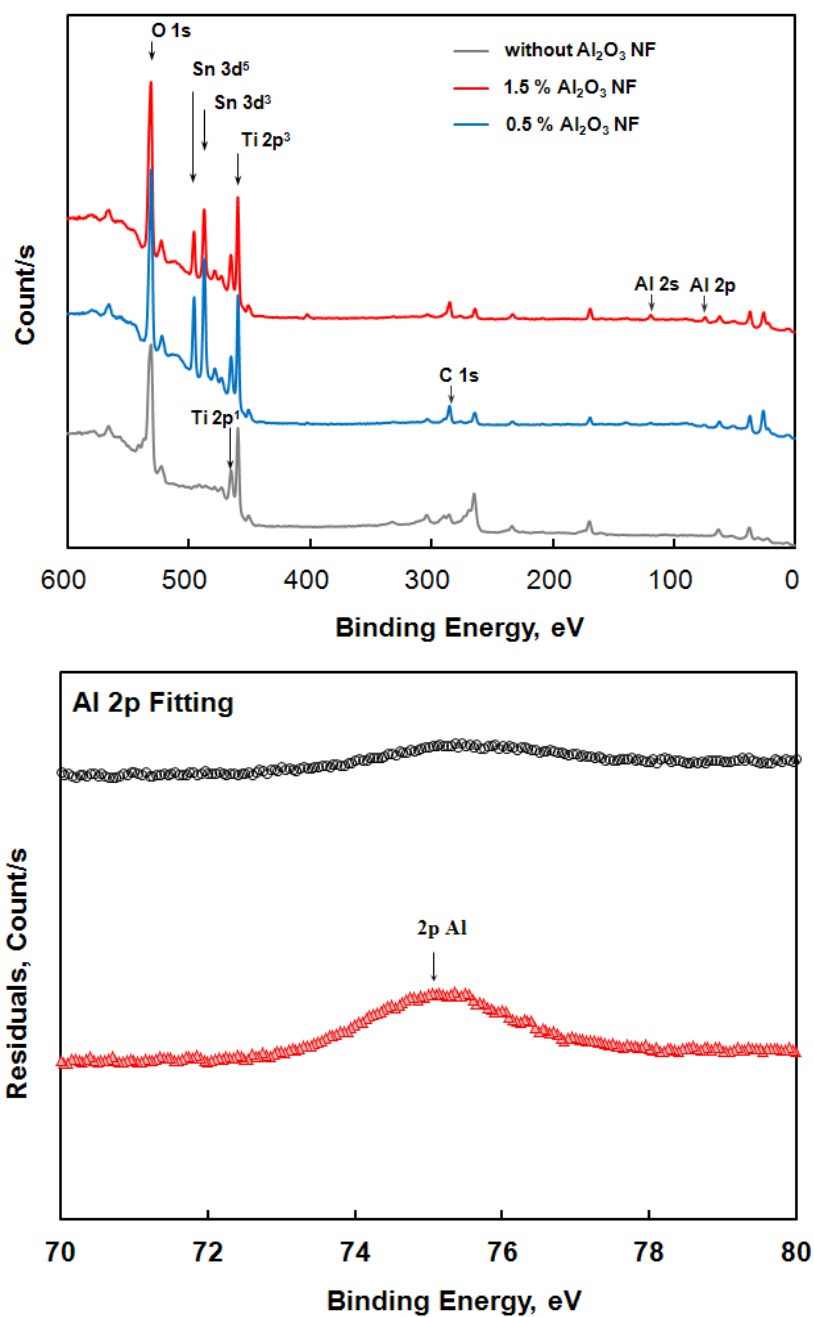


Figure 4-23 XPS Survey graphs (a) and Al 2p core level (b) of Al₂O₃ nanofiber doped TiO₂ films.

Figure 4-24 shows the electrochemical impedance spectra of corresponding to the charge recombination on the interface of $\text{TiO}_2/\text{Al}_2\text{O}_3/\text{dye}/\text{electrolyte}$ (frequency range: $10^3\sim 10^6$, $1\sim 10^3$ and $0.1\sim 1$ Hz), where the spectra of three cells are composed of three semicircles. It has been reported that the semicircle in high frequency is attributed to a charge transfer at the counter electrode, a circle in intermediate-frequency is associated with both the electron transport in the mesoscopic TiO_2 film and back reaction at the $\text{TiO}_2/\text{electrolyte}$ interface, and a semicircle in low-frequency reflects the diffusion of I_3^- in the electrolyte [131-133]. The high frequency offset in the spectra is the series resistance of the cell, primarily due to the FTO resistance. The impedance at the platinum/electrolyte interface can be seen in the spectra as a small arc at high frequencies. The charge transport and charge transfer resistance in the $\text{TiO}_2/\text{Al}_2\text{O}_3/\text{dye}/\text{electrolyte}$ can be seen as the big semicircle at the intermediate frequencies, whose radius increases with increase in amount of Al_2O_3 nanofiber dopant. And the semicircle in low frequency decrease with increase in amount of Al_2O_3 nanofiber dopant. These results indicate that the diffusion rate of I_3^- in the ionic liquid electrolyte is higher than the only TiO_2 electrode and the slow response of only TiO_2 electrode to attain a saturated point can be explained by the slow diffusion rate of I_3^- .

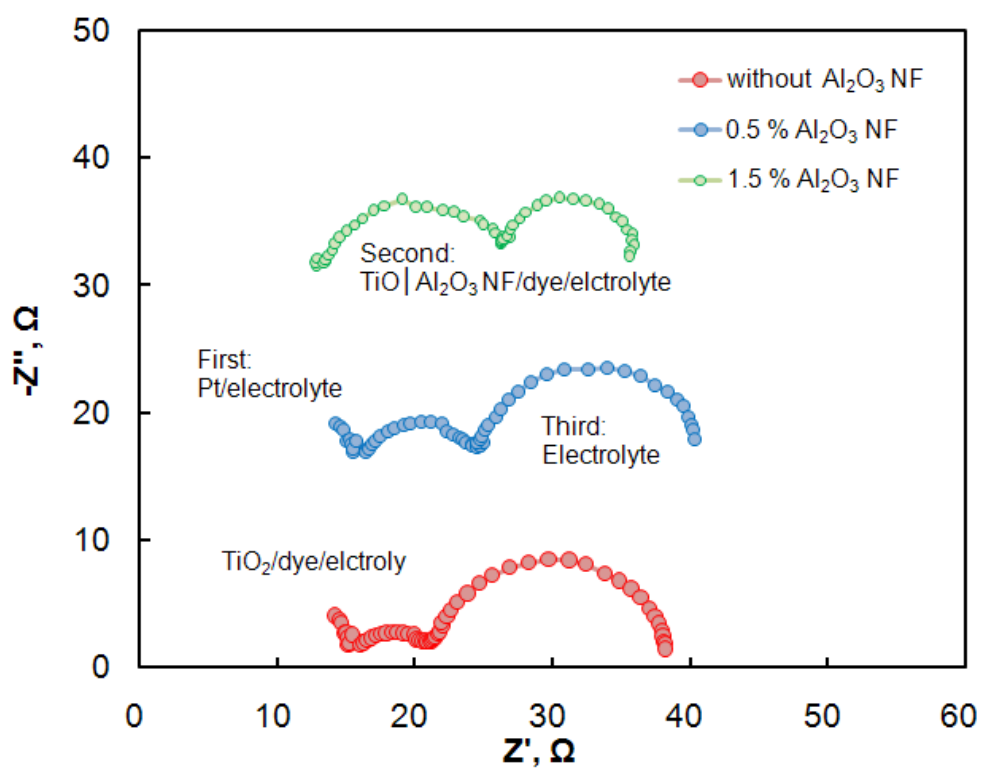


Figure 4-24 Electrochemical impedance spectra of $\text{TiO}_2/\text{Al}_2\text{O}_3$ nanofiber doped electrode.

To evaluate the photovoltaic performance of $\text{TiO}_2/\text{Al}_2\text{O}_3$ NF electrode, the current–voltage curves were obtained. The photocurrent-voltage (I-V) curves were measured using a source measure unit under irradiation of white light from a 150 W Xenon lamp (K401 CW150 Lamp power supply; McScience Co.). The incident light intensity and the active cell area were 100 mW/cm^2 and 0.25 cm^2 , respectively. The I-V curves were used to calculate the short-circuit current(I_{sc}), open-circuit voltage(V_{oc}), fillfactor(FF), and overall conversion efficiency (η_{eff}) of DSSC. As shown in Figure 4-25 and Table 4-7, it was observed that the overall conversion efficiency(η_{eff}) is in the following order: Al_2O_3 NF (1.5 wt%: 5.99 %) > Al_2O_3 NF (0.5 wt%: 5.54 %) > Al_2O_3 NF (0.0 wt%: 5.10 %). This trend is identical to that of the N719 adsorption on nanoparticle and nanofibers of TiO_2 . Therefore, It is reasonable to conclude that the overall photovoltaic performance was substantially dependent on the adsorption amount of N719 because of the high packing density of TiO_2 electrode by employing the Al_2O_3 nanofiber additives.

Table 4-6 Photocurrent-voltage of dye-sensitized solar cells for Al_2O_3 nanofiber doped TiO_2 electrodes

Al_2O_3 nanofiber(NF) content	V_{oc} , V	I_{sc} , mA/cm^2	FF	η_{eff} , %
Without NF	0.71	16.70	0.42	5.10
0.5 % NF	0.70	17.98	0.42	5.54
1.5 % NF	0.67	20.00	0.43	5.99

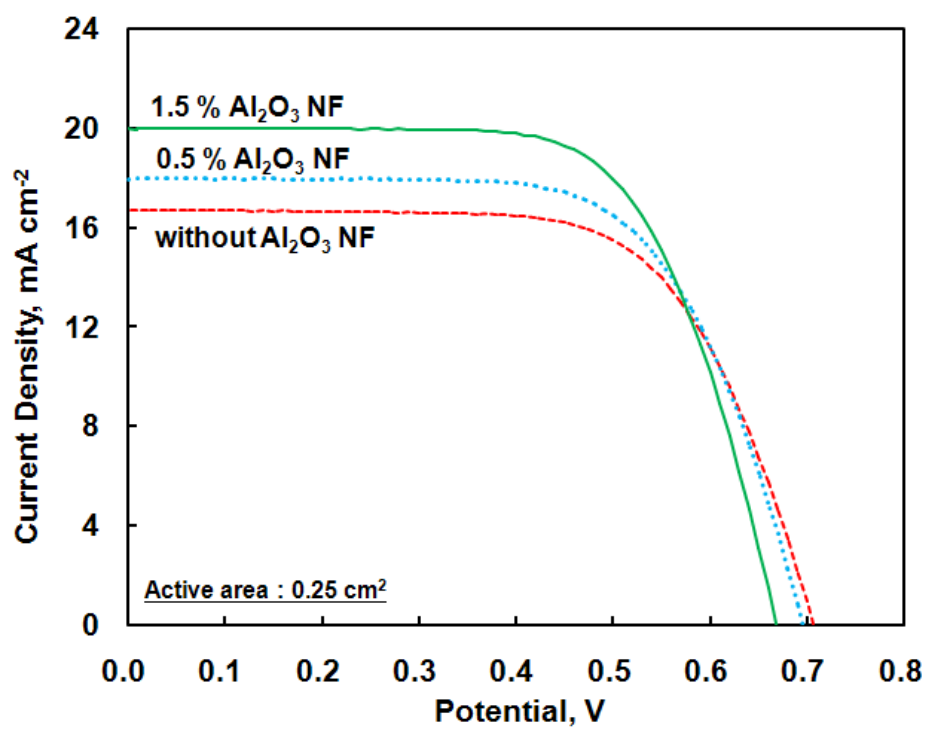


Figure 4-25 Photocurrent-voltage(I-V) polt of DSSCs depending on the contents of Al_2O_3 nanofiber dopant in TiO_2 electrode.

Chapter V. Conclusions

In this research, an experiment for TiO_2 modification which makes a wider range of sunlight available as well as a recombination blocking layer for the dye-sensitized solar cell was conducted. The main conclusions of this research are:

The TiO_2 particles produced by the sol-gel method (expressed hereafter as sol-gel TiO_2), which were synthesized at a low temperature and calcined at higher temperatures, and their structural characteristics were examined. The sol-gel TiO_2 particles were relatively uniform in size. According to the results of XRD analysis, all TiO_2 powders calcined at up to 500°C were anatase type.

The TiO_2 nanofibers were prepared with an electrospinning method from a mixture of titanium-tetra-isopropoxide and polyvinylpyrrolidone. It was found from the FE-SEM images of TiO_2 nanofiber that the fiber-like shape and continuous morphology, the diameter of the electrospun TiO_2 nanofibers was in the range of 70~160 nm. The BET surface area was about $50 \text{ m}^2\text{g}^{-1}$ for the TiO_2 nanoparticles and $17 \text{ m}^2\text{g}^{-1}$ for the TiO_2 nanofibers. The average poresize of the nanoparticles and nanofibers was between 67 and 3.2 nm.

Electrospun Al_2O_3 nanofibers were successfully prepared by combining the sol-gel and electrospinning methods, while using AIP as an alumina precursor. On the basis of the results of the XRD analysis, the Al_2O_3 nanofibers calcined at 1200°C were identified as comprising the α -alumina phase. It was found from the SEM images of the various samples that the

fiber-like shape and continuous morphology of the as-spun samples were preserved in the calcined samples. The diameters of the fabricated nanofibers were small and in a range between 102 and 378 nm. When compared to polymer nanofibers, the electrospun Al_2O_3 nanofibers were found to be more sensitive to humidity. Humidity between 40 and 50% RH led to clean fibrous structure. Higher humidity (70% RH or more) induced excessive plasticization of the as-spun $\text{Al}_2\text{O}_3/\text{PVP}$ nanofiber. When the voltage is changed to 15 kV from 20 kV, the fiber-fiber bonding phenomenon is slightly improved.

In order to know the possibility of applying this to the energy field and environment, experiments for the photo conversion efficiency are measured using the DSSCs made in this research. Synthesized sol-gel TiO_2 particles, electrospun TiO_2 nanofibers and electrospun Al_2O_3 nanofibers were used for the photoelectrodes and the films of single-phase anatase crystallites were formed on the FTO glass for a working DSSC electrode. The films were characterized by BET, FE-SEM, FT-IR, XPS, and XRD analysis. The content of Ti and O in the sol-gel TiO_2 particles are 27.01% and 52.23% corresponding closely to the Ti^{4+} state. The nanoparticle size of the sol-gel TiO_2 particle is about 14nm and the film thickness was ca. 4 μm . A dye-sensitized solar cell of sol-gel TiO_2 particale gave an open-circuit voltage of 0.55 V and a short-circuit current density of 15.57 mA/cm^2 for an incident light intensity of 100 mW/cm^2 . DSSCs made with sol-gel TiO_2 nanocrystalline films as photo-anodes achieved better photo-energy conversion efficiency compared to those prepared using commercially available P25- TiO_2 films. A power conversion efficiency of over 4.88 % was achieved using

the single-phase anatase sol-gel TiO₂ crystallites synthesized in this work. The order of the photocurrent densities and conversion efficiency increased with adsorption amount and adsorption time, until the adsorption time was 5.5 h. The results showed that the high adsorption capacity of sol-gel TiO₂ with the low charge transfer resistance may give rise to the superior I_{sc} of DSSCs because of the monolayer adsorption. However, after an adsorption time of 5.5h, there was little change in the amount of adsorption and the photocurrent density and conversion efficiency of sol-gel TiO₂ decreases with increasing immersion time.

In order to improve the short-circuit photocurrent, we added the TiO₂ nanofibers and Al₂O₃ nanofibers to the TiO₂ electrode. The additive TiO₂ nanofibers increased the amount of dye adsorption on the TiO₂ electrode. Also, the TiO₂ nanofibers added to the DSSC can increase the conversion energy by up to about 15% over conventional DSSCs with only TiO₂ electrodes. Conversion efficiency (η_{eff}) of the photoelectrode with 1.5% TiO₂ nanofiber content was 5.87 %. The additive Al₂O₃ nanofiber increased the amount of dye adsorption on the TiO₂ electrode. The higher diffusion rate of I₃⁻ in the ionic liquid electrolyte in the TiO₂/Al₂O₃ NF electrode compared to the simple TiO₂ electrode was confirmed by the electrochemical impedance spectra.

Also, the Al₂O₃ nanofibers added to the DSSC can increase the conversion efficiency by 20% over conventional DSSCs with only TiO₂ films. The photo-to-electric conversion efficiency for DSSCs of TiO₂/Al₂O₃ nanofiber electrodes was 5.99%.

Reference

1. Z. Donga, S.J. Kennedyb, Y. Wu, *Journal of Power Sources*, 196, 4886–4904 (2011).
2. OPEC Seretariat, *World Oil Outlook 2011*, Organization of Petroleum Exporting Countries, Vienna, 2011, pp. 25-149.
3. J.T. Kiehl, K.E. Trenberth, *Bull. Am. Meteorol. Soc.* 78, 197–208 (1997).
4. D. Li, Y. Xia. *Adv. Mater.*, 16(14), 1151–1170 (2004).
5. H. Yu, J. Guo, S. Zhu, Y. Li, Q. Zhang, M. Zhu. *Materials Letters*, 74, 247–249 (2012).
6. M. Law, J. Goldberger, P.D. Yang, *Ann. Rev. Mater. Res.*, 34, 83–122 (2004).
7. J.X. Huang, S. Virji, B.H. Weiller, R.B. Kaner, *J. Am. Chem. Soc.*, 125, 314–315 (2003).
8. X. Wang, Y.D. Li, *J. Am. Chem. Soc.*, 124, 2880–2881 (2002).
9. Y.G. Sun, Y.D. Yin, B.T. Mayers, T. Herricks, Y.N. Xia, *Chem. Mater.*, 14, 4736–4745 (2002).
10. A.A. Tseng, A. Notargiacomo, T.P. Chen, *J. Vac. Sci. Technol. B*, 23, 877–894 (2005).
11. D. Wouters, U.S. Schubert, *Angew. Chem.-Int. Ed.*, 43, 2480–2495 (2004).
12. J.D. Hartgerink, E. Beniash, S.I. Stupp, *Science*, 294, 1684–1688 (2001).
13. V. Maneeratana, W.M. Sigmund, *Chemical Engineering Journal*, 137, 137–143, (2008).
14. Y. Dimitriev, Y. Ivanova, R. Iordanova, *J. of the Uni. of Che. Tec. and Met.*, 43, 2, 181–192 (2008)
15. C. J. Brinker, G. W, scherer “Sol-gel Sciences”, Academic Press
16. K. Suriye, B. Jongsomjit, C. Satayaprasert, P. Prasertthdam, *Applied Surface Science*, 255, 2759–2766 (2008).
17. D. Li, Y.N. Xia, *Adv. Mater.*, 16, 1151–1170 (2004).
18. A. Greiner, J.H. Wendorff, *Angew. Chem. Int. Ed.*, 46, 5670–5703 (2007).
19. Hui WU, Wei PAN, Dandan LIN, Heping LI, *Journal of Advanced Ceramics*, 1(1), 2–23 (2012).
20. Z.M. Huang, Y.Z. Zhang, M. Kotakic, S. Ramakrishn, *Composites Science and Technology*, 63, 2223–2253 (2003).

21. A.L. Yarin, S. Koombhongse, D.H. Reneker, J. Appl. Phys., 89, 3018–3026 (2001).
22. Q.P. PHAM, U. SHARMA, A.G. MIKOS, TISSUE ENGINEERING, Volume 12, Number 5, (2006).
23. L. Huang, R.A. McMillan, R.P. Apkarian, B. Pourdeyhimi, V.P. Conticello, E.L. Chaikof, Macromolecules, 33, 2989–2997 (2000).
24. H. Fong, W.D. Liu, C.S. Wang, R.A. Vaia, Polymer, 43, 775–780 (2002).
25. C.L. Casper, J.S. Stephens, N.G. Tassi, D.B. Chase, J.F. Rabolt, Macromolecules, 37, 573–578 (2004).
26. J.T. McCann, D. Li, Y.N. Xia, J. Mater. Chem., 15, 735–738 (2005).
27. D. Li, Y.L. Wang, Y.N. Xia, Nano Lett., 3, 1167–1171 (2003).
28. V. Thavasi, G. Singh, S. Ramakrishna, Energy Environ. Sci., 1, 205–221 (2008).
29. E.D. Boland, J.A. Matthews, K.J. Pawlowski, D.G. Simpson, G.E. Wnek, G.L. Bowlin, Front. Biosci., 9, 1422–1432 (2004).
30. E.R. Kenawy, G.L. Bowlin, K. Mansfield, J. Layman, D.G. Simpson, E.H. Sanders, G.E. Wnek, J. Control. Rel., 81, 57–64 (2002).
31. K.S. Rho, L. Jeong, G. Lee, B.M. Seo, Y.J. Park, S.D. Hong, S. Roh, J.J. Cho, W.H. Park, B.M. Min, Biomaterials, 27, 1452–1461 (2006).
32. I.D. Kim, A. Rothschild, B.H. Lee, D.Y. Kim, S.M. Jo, H.L. Tuller, Nano Lett., 6, 2009–2013 (2006).
33. J. Yoon, S.K. Chae, J.M. Kim, J. Am. Chem. Soc., 129, 3038–3039 (2007).
34. Z.W. Ma, M. Kotaki, S. Ramakrishna, J. Membr. Sci., 265, 115–123 (2005).
35. N. Bhardwaj, S.C. Kundu, Advances, 28, 325–347 (2010).
36. E.J. Chong, T.T. Phan, I.J. Lim, Y.Z. Zhang, B.H. Bay, S. Ramakrishna, Acta. Mater., 3, 321–330, (2007).
37. H.L. Jiang, D.F. Fang, B.S. Hsiao, B. Chu, W.L. Chen, 5, 326–333 (2004).
38. K.H. Kim, L. Jeong, H.N. Park, S.Y. Shin, W.H. Park, S.C. Lee, J. Biotechnol., 120, 327–339 (2005).
39. P. Gupta, C. Elkins, T.E. Long, G.L. Wilkes, Polymer, 46 4799–4810 (2005).
40. A. Koski, K. Yim, S. Shivkumar, Mater. Lett., 58, 493–497 (2004).
41. C. Zhang, X. Yuan, L. Wu, Y. Han, J. Sheng, Eur. Polym. J., 41, 423–432 (2005).

42. K.H. Kim, L. Jeong, H.N. Park, S.Y. Shin, W.H. Park, S.C. Lee, *J. Biotechnol.*, 120, 327–339 (2005).
43. C.S. Ki, D.H. Baek, K.D. Gang, K.H. Lee, I.C. Um, Y.H. Park, *Polymer*, 46, 5094–5102 (2005).
44. T.J. Sill, H.A.V. Recum, *Biomaterials*, 29, 1989–2006 (2008).
45. C.L. Casper, J.S. Stephens, N.G. Tassi, D.B. Chase, J.F. Rabolt, *Macromolecules*, 37, 573–578 (2004).
46. C. Mit-uppatham, M. Nithitanakul, P. Supaphol, *Macromol. Chem. Phys.*, 205, 2327–2338 (2004).
47. M. R. Narayan, *Renewable and Sustainable Energy Reviews*, 16, 208–215 (2012).
48. K. Kalyanasundaram, M. Grätzel, *Coord. Chem. Rev.*, 77, 347 (1998).
49. A. Hagfeldt, M. Grätzel, *Chem. Rev.*, 95(1), 49 (1995).
50. <http://ruby.colorado.edu/~smyth/min/tio2.html>
51. J. Xu, C. Zhai, B. Zheng, H. Li, M. Zhu, Y. Chen, *Vacuum*, 86, 1161–1164 (2012)
52. B. O'Regan, M. Grätzel, *Nature*, 353, 737–740 (1991).
53. M. Grätzel, *Photoelectrochemical cells. Nature*, 414, 338–344 (2001).
54. M.A. Green, K. Emery, Y. Hishikawa, W. Warta, *Prog. Photovolt: Res. Appl.*, 18, 144 (2010).
55. S. Kolsek, D. Raftery, *J. Phys. Chem. B*, 105 (2001).
56. T. Ohno, F. Tanihara, K. Fujihara, S. Izumi, M.J. Masumura, R.W. Photochem, J. Matthews, *Phys. Chem.*, 91, 3328 (1987).
57. M. Shanmugam, M.F. Baroughi, D. Galipeau, *Thin Solid Films*, 518, 2678–2682 (2010)
58. C.S. Karthikeyan, M. Thelakkat, M. Willert-Porada, *Thin Solid Films*, 187, 511–512 (2006).
59. S.T. Martin, C.L. Morrison, M.R. Hoffmann, *J. phys. Chem.*, 98, 13695 (1994)
60. J. Nelson, S.A. Haque, D.R. Klug, J.R. Durrant, *Phys. Rev. B*, 63, 205321 (2001).
61. J. Nissfolk, K. Fredin, A. Hagfeldt, G. Boschloo, *J. Phys. Chem. B*, 110, 17715 (2006).
62. M. Yanagida, K. Sayama, K. Kasuga, M. Kurashige, H. Sugihara, *J. Photochem. Photobiol., A Chem.*, 182, 288 (2006).
63. E. Palomares, J.N. Clifford, S.A. Haque, T. Lutz, J.R. Durrant, *J. Am. Chem. Soc.*, 125, 475 (2003).

64. E. Palomares, J.N. Clifford, S.A. Haque, T. Lutz, J.R., Durrant, *Chem. Commun.*, 14, 1464 (2002).
65. Md. K. Nazeeruddin, E. Baranoff, M. Graetzel, *Solar Energy*, 85, 1172–178 (2011).
66. C.J. Barbe, F. Arendse, P. Comte, M. Jirousek, F. Lenzmann, V. Shklover, M. Graetzel, *J. Am. Chem. Soc.*, 80, 3157 (1997).
67. G. Rothenberger, P. Comte, M. Graetzel, *Solar Energy Mater. Solar Cells*, 58, 321, (1999).
68. A.H. Shnishil, S.S. Chid, M.J. Yaseen, and T.J. Alwan, *Energy Procedia*, 6, 153–159 (2011).
69. C. A. GUEYMARD, D. MYERS, K. EMERY, *Solar Energy*, 73, 6, 443–67 (2002).
70. K. Takagi, S. Magaino, H. Saito, T. Aoki, D. Aoki, *Journal of Photochemistry and Photobiology C: Photochemistry Reviews*, 175(12), 1–11 (2012).
71. M. Grätzel, *Prog. Photovolt. Res.*, 8, 171 (2000).
72. M. K. Nazeeruddin, A. Kay, I. Rodicio, R. Humphry-Baker, E. Müller, P. Liska, N. Vlachopoulos, M.J. Grätzel, *Am. Chem. Soc.*, 115, 6382 (1993).
73. N. Koide, I. Han, *Rev. Sci. Instrum.*, 75, 2828–2831 (2004).
74. V. Thavasi, V. Renugopalakrishnan, R. Jose, S. Ramakrishna, *Materials Science and Engineering R*, 63, 81–99 (2009).
75. Q. Zhang, G. Cao, *Nano Today*, 6, 91–109 (2011).
76. A.S. Polo, M.K. Itokazu, N.Y.M. Iha, *Coordination Chemistry Reviews*, 248, 1343–1361 (2004).
77. A. Hagfeldt, M. Grätzel, *Acc. Chem. Res.*, 33(5), 269 (2000).
78. A. Hagfeldt, B. Didriksson, T. Palmqvist, H. Lindström, S. Södergren, H. Rensmo, S.E. Lindquist, *Sol. Energy Mater. Sol. Cells*, 31, 481 (1994).
79. M. Gutschner, S. Nowak, *Potential and Implementation of Building-Integrated Photovoltaics on the Local Level Case Studies and Comparison of Urban and Rural Areas in Switzerland*, 16th European Photovoltaic Solar Energy Conference: Glasgow, (2001).
80. M. Grätzel, *Curr. Opin. Colloid Interface Sci.*, 4, 314 (1999).
81. M. Grätzel, *Journal of Photochemistry and Photobiology C: Photochemistry Reviews*, 4, 145–153 (2003).

82. V. Thavasi, V. Renugopalakrishnan, R. Jose, S. Ramakrishna, *Materials Science and Engineering R*, 63, 81–99 (2009).
83. E. Palomares, J.N. Clifford, S.A. Haque, T. Lutz, J.R. Durrant, *Chem. Commun.*, 1464–1465 (2002).
84. V. Ganapathy, B. Karunagaran, S.W. Rhee, *Journal of Power Sources* 195 5138–5143 (2010).
85. D. Cahen, G.J. Hodes, *Phys. Chem. B*, 104, 2053 (2000).
86. J. Ferber, J. Luther, *Sol. Energy Mater. Sol. Cells*, 53, 29 (1998).
87. V. Thavasi, V. Renugopalakrishnan, R. Jose, S. Ramakrishna, *Materials Science and Engineering R*, 63, 81–99 (2009).
88. J. Guo, D. Stockwell, X. Ai, C. She, N.A. Anderson, T. Lian, *J. Phys. Chem. B*, 110, 5238–5244 (2006).
89. J. Guo, C. She, T. Lian, *J. Phys. Chem. C*, 111, 8979–8987 (2007).
90. S.A. Haque, Y. Tachibana, R.L. Willis, J.E. Moser, M. Grätzel, D.R. Klug, J.R. Durrant, *J. Phys. Chem. B*, 104, 538 (2000).
91. S.Y. Huang, G. Schlichthörl, A.J. Nozik, M. Grätzel, A.J. Frank, *J. Phys. Chem. B*, 101, 2576 (1997).
92. J. Nelson, S.A. Haque, D.R. Klug, J.R. Durrant, *Phys. Rev. B*, 63, 205321 (2001).
93. A.V. Barzykin, M. Tachiya, *J. Phys. Chem. B* 106, 4356 (2002).
94. A. Zaban, A. Meier, B.A. Gregg, *J. Phys. Chem. B*, 101, 7985 (1997).
95. N.G. Park, *J. Ind. Eng. Chem.*, 15(3), 265 (2004).
96. S.Y. Huang, G. Schlichthörl, A.J. Nozik, M. Grätzel, A.J. Frank, *J. Phys. Chem. B*, 101, 2576 (1997).
97. L. Xu, H. Song L. Chou, *Materials Chemistry and Physics*, 132, 1071–1076 (2012).
98. P. Wang, S.M. Zakeeruddin, P. Comte, R. Charvet, R. Humphry-Baker, M.J. Grätzel, *Phys. Chem. B*, 107(51), 14336 (2003).
99. S. Ito, T.N. Murakami, P. Comte, P. Liska, C. Grätzel, M.K. Nazeeruddin, M. Grätzel, *Thin Solid Films*, 516, 4613 (2008).
100. S. Ito, M.K. Nazeeruddin, P. Liska, P. Comte, R. Charvet, P. Pechy, M. Jirousek, A. Kay, S.M. Zakeeruddin. M. Grätzel, *Prog. Photovolt: Res. Appl.*, 15, 603 (2007).

101. L. Kaven, B. O'Regan, A. Kay, M.J. Grätzel, *Electroanal. Chem.*, 346, 291 (1993).
102. K. J. Hwang, S. J. Yoo, S. H. Jung, D. W. Park, S. I. Kim, and J. W. Lee, *Bull. Korean Chem. Soc.*, 30(1), 172 (2009)
103. M. Gutschner, S. Nowak, Potential and Implementation of Building-Integrated Photo-voltaics on the Local Level - Case Studies and Comparison of Urban and Rural Areas in Switzerland, 16th European Photovoltaic Solar Energy Conference: Glasgow, (2001).
104. G. Wolfbauer, A.M. Bond, J.C. Eklund, D.R. MacFarlane, *Sol. Energy Mater. Sol. Cells*, 70, 85 (2001).
105. J. Rijnberg, J.M. Kroon, J. Wienke, A. Hinsch, J.A.M. Van Roosmalen, W.C. Sinke, B.J.R. Scholtens, J.G. De Vries, C.G. De Koster, A.L.L. Duchateau, I.C.H. Maes, H.J.W. Henderickx, Long Term Stability of Nanocrystalline Dye-Sensitized Solar Cells, 2nd World Conference and Exhibition on Photovoltaic Solar Energy Conversion: Vienna, (1998).
106. A. Kay, M. Grätzel, *Sol. Energy Mater. Sol. Cells*, 44, 99 (1996).
107. N. Papageorgiou, Y. Athanassov, M. Armand, P. Bonhote, H. Pettersson, A. Azam, M.J. Gratzel, *Electrochem. Soc.*, 143, 3099 (1996).
108. N. Papageorgiou, Y. Athanassov, M. Armand, P. Bonhote, H. Pettersson, A. Azam, M.J. Gratzel, *Electrochem. Soc.*, 143, 3099 (1996).
109. R.G. Gordon, *MRS Bulletin*, 52 (2000).
110. N.G. Park, Van de Lagemaat, J. Frank, A. J. J. *Phys. Chem. B*, 104, 8989 (2000).
111. T. Yoko, L. Hu, S. Sakka, *Thin solid films*, 315, 111 (1998)
112. Q. Zhang, G. L. Griffin., *J. Electrochem. Soc*, 137. 120 (1995)
113. J.F. Moudler, W.F. Stickle, P.E. Sobol, K.D. Bomben, *Handbook of X-ray Photoelectron Spectroscopy*, Perkin-Elmer: Eden prairie, (1992).
114. W. Kang, B. Cheng, Q. Li, X. Zhuang, Y.N. Ren, *Textile Reaserch Journal*, 81(2), 148-155 (2011).
115. W. Kang, B. Cheng, Q. Li, X. Zhuang, Y.N. Ren, *Textile Reaserch Journal*, 81(2), 148-155 (2011).
116. L. Favaro, A. Boumaza, P. Roy, J. Ledion, G. Sattonnay, J.B. Brubach, A.M. Huntz, R. Tetot, *Journal of Solid State Chemistry*, 183, 901-908 (2010).
117. A. Mahapatra, B.G.Mishra, G.Hota, *Ceramics International*, 37, 2329-2333 (2011).

118. V. Maneeratana, W.M. Sigmund, *Chemical Engineering Journal*, 137, 137–143 (2008).
119. A. Luque, S. Hegedus, *Handbook of Photovoltaic Science and Engineering*, John Wiley & Sons: Chichester, (2003).
120. P.D. Yang, D.Y. Zhao, D.I. Margolese, B.F. Chmelka, G.D. Stucky, *Chem. Mater.*, 11, 2813 (1999).
121. Y.H. Yu, Z. Gao, *Chem. Commun.*, 1755 (2000).
122. D.W. Park, K.H. Park, J.W. Lee, K.J. Hwang, Y.K. Choi, *J. Nanosci. Nanotechnol.*, (2007), 7(11), 3722.
123. K.J. Hwang, S.J. Yoo, S.S. Kim, J. M. Kim, W.G. Shim, S. I. Kim, J.W. Lee, *J. Nanosci. Nanotechnol.*, 8(10), 4976 (2008).
124. C.P. Leon, L. Kador, B. Peng. M.J. Thelakkat, *Phys. Chem. B.*, 110(17), 8723 (2006).
125. K.S. Finnie, Bartlett, J. R.; Woolfrey, J. L. *Langmuir*, (1998), 14, 2744.
126. R. Katoh, A. Furube, A.V. Barzykin, H. Arakawa, M. Tachiya, *Coordination Chemistry Reviews*, 248, 1195–213 (2004).
127. S.Q. Fan, Y. Geng, C. Kim, S. paik, J. Ko, *Materials Chemistry and Physics* 132, 943-949 (2012).
128. A.F. Lotus, R.K. Feaver, L.A. Britton, E.T. Bender, D.A. Perhay, N. Stojilovic, R.D. Ramsier, G.G. Chase, *Materials Science and Engineering B*, 167, 55–59 (2010).
129. R.W. Tuttle, A. Chowdury, E.T. Bender, R.D. Ramsier, J.L. Rapp, M.P. Espe, *Appl. Surf. Sci.*, 254, 4925–4929 (2008).
130. E.T. Bender, P. Katta, G.G. Chase, R.D. Ramsier, *Surf. Interface Anal.*, 38, 1252–1256 (2006).
131. K. Takagi, S. Magaino, H. Saito, T. Aoki, D. Aoki, *Journal of Photochemistry and Photobiology C: Photochemistry Reviews*, 175, 1–12 (2012).
132. A. Sreekumaran Nair, Rajan Jose, Yang Shengyuan, Seeram Ramakrishna, *Journal of Colloid and Interface Science* 353, 39–45 (2011)
133. E. Palomares, J.N. Clifford, S.A. Haque, T. Lutz, J.R. Durrant, *J. Am. Chem. Soc.* 125, 475 (2002).

Preparation and Characterization of Electrospun Nanofibers for Dye-sensitized Solar Cells

Cheong-Suk Yang

Advisor : prof. Kim Sun Il, Ph.D

Department of Chemical Engineering

Graduate School of Chosun University

A solar cells are dealt to overcome the future energy and environmental problems. Solar cell as an alternative energy source is electricity generator changing from sun light to electricity directly by photovoltaic effect. Compared to silicon solar cell, dye-sensitized solar cells (DSSC) have been much attention from industrial fields because of the high energy conversion efficiency and low fabrication cost. For the enhancement of energy conversion efficiency, many researchers have been studied on the nanocrystalline TiO_2 electrode, dye development, electrolyte, electron diffusion, sealing technology and conductivity substrate.

In this study, various TiO_2 electrode was developed and the energy conversion efficiency was evaluated to increase the photovoltaic conversion efficiency. Nanocrystalline TiO_2 particles as a key part in DSSC were synthesized by typical sol-gel method. The synthesized TiO_2 particles are single-phase anatase nanocrystallites and have particle size of the 15 nm. The prepared TiO_2 electrode including commercial P25- TiO_2 electrode were characterized by BET, FE-SEM, FT-IR, XPS, and XRD analysis. It was found that DSSC made of TiO_2 electrode as photo-anodes achieved better photo-energy conversion efficiency compared to those prepared using commercially available P25- TiO_2 electrode. The influences of adsorption properties on the energy conversion efficiency of DSSC are also

investigated. To this end, adsorption equilibrium and kinetics of N719 dye on the TiO_2 electrode were investigated.

To improve the photovoltaic conversion efficiency, metal oxides have been used for the reduction of electron recombination losses at TiO_2 /dye/electrolyte interface. In this study, the energy conversion efficiency of TiO_2 photo electrodes adding electrospun TiO_2 and Al_2O_3 nanofibers were investigated. The electrospun samples were characterized by BET, SEM, XRD, FT-IR and TGA analysis. To improve the short-circuit photocurrent, TiO_2 nanoparticle paste with different mixing ratio of additives (i.e., electrospun TiO_2 and Al_2O_3 nanofibers) was prepared and applied for the evaluation of DSSC performance. The conversion efficiencies of TiO_2 photo electrode with TiO_2 and Al_2O_3 nanofibers were increased up to 15 % and 20 %, respectively, compared to TiO_2 photoelectrode without nanofiber additives. This result may come from the fact that the adsorption amount of dye molecule and the diffusion coefficient of I_3^- for TiO_2 photoelectrode including additives of TiO_2 and Al_2O_3 nanofibers were higher and faster than those of TiO_2 photoelectrode prepared by sol-gel method.